Electronic Properties of Novel Mid-Infrared Materials and Devices

Davide Maria Di Paola

Thesis submitted to the University of Nottingham
for the degree of Doctor of Philosophy
October 2018

Abstract

This thesis describes the effects of the combined incorporation of nitrogen (N) and hydrogen (H) atoms in the narrow gap III-V InAs semiconductor.

The plasmonic properties of the dilute nitride In(AsN) alloy are investigated before and after the *post-growth* incorporation of H-atoms. The hydrogenation of In(AsN) leads to a substantial increase of the electron density near the surface. The optical excitation of In(AsN):H creates a mid-infrared (MIR) surface plasmon polariton (SPP) mode detected by reflectance techniques. The plasmonic response of the highly doped In(AsN):H compound is spatially tailored and suppressed by different techniques, such as laser or electron beam annealing, as probed by Raman spectroscopy and scanning electron microscopy (SEM). This approach enables the control of the electron density of a highly doped semiconductor by changing its chemical composition on the μm-scale.

Furthermore, the effects of the incorporation of N in the quantum well (QW) layer of an In(AsN)/(InAl)As resonant tunnelling diode (RTD) are presented. We show that the N-incorporation leads to the creation of strongly localized zero-dimensional (0D) states in the band gap of In(AsN). These contribute to an extended and weakly temperature dependent negative differential resistance (NDR) in the current-voltage (*I*-*V*) characteristic of the diode, not observed in N-free RTDs. This behaviour is attributed to a new type of Zener tunnelling assisted by N-related 0D states, whose size is probed by magneto-tunnelling experiments. These N-related states also contribute to the tuning of the MIR electroluminescence (EL) of the RTD, which notably also shows the occurrence of up-conversion up to room temperature.

List of publications

1. D. M. Di Paola, M. Kesaria, O. Makarovsky, A. Velichko, L. Eaves, N. Mori, A. Krier and A. Patanè, "Resonant Zener tunnelling via zero-dimensional states in a narrow gap diode", *Scientific Reports* **6**, 32039 **(2016)**.
2. A.V. Velichko, Z. R. Kudrynskyi, D. M. Di Paola, O. Makarovsky, M. Kesaria, A. Krier, I. C. Sandall, C. H. Tan, Z. D. Kovalyuk and A. Patanè, "Highly-mismatched InAs/InSe heterojunction diodes", *Applied Physics Letters* **109**, 182115 **(2016)**.
3. D. M. Di Paola, A. V. Velichko, M. Bomers, N. Balakrishnan, O. Makarovsky, M. Capizzi, L. Cerutti, A. Baranov, M. Kesaria, A. Krier, T. Taliercio and A. Patanè, "Optical Detection and Spatial Modulation of Mid-infrared Surface Plasmon Polaritons in a Highly Doped Semiconductor", *Advanced Optical Materials* **6**, 1700492 **(2018)**.
4. M. Bomers, D. M. Di Paola, L. Cerutti, T. Michel, R. Arinero, E. Tourniè, A. Patanè and T. Taliercio, "Mid-IR plasmonic compound with gallium oxide toplayer formed by GaSb oxidation in water", *Semiconductor Science and Technology* **33**, 095009 **(2018)**.

List of conference abstracts

1. D. M. Di Paola, M. Kesaria, O. Makarovsky, A. Velichko, L. Eaves, A. Krier and A. Patanè: "Resonant Zener Tunnelling via Zero-dimensional states in the Novel Mid-Infrared Alloy In(AsN)"; *19th International Conference on Molecular-Beam Epitaxy*, Montpellier (France); **09/2016**.
2. M. Bomers, M. J. Milla, D. M. Di Paola, F. Barho, L. Cerutti, F. González-Posada, A. Patanè, E. Tournié and T. Taliercio: "Impact of GaSb oxidation on the mid-IR properties of InAsSb:Si/GaSb-based plasmonic biosensors", *8th International Conference on Surface Plasmon Photonics (SPP8)*, Taipei (Taiwan); **05/2017**.
3. D. M. Di Paola, A. V. Velichko, M. Bomers, N. Balakrishnan, O. Makarovsky, M. Capizzi, A. Polimeni, L. Cerutti, A. Baranov, M. Kesaria, A. Krier, L. Eaves, T. Taliercio and A. Patanè: "Zero-dimensional Zener Tunnelling and Plasmon Resonances due to N- and H- Incorporation in the Narrow Gap InAs"; *EDISON20 - The 20th International Conference on Electron Dynamics in Semiconductors, Optoelectronics and Nanostructures*, Buffalo (USA); **07/2017**.
4. D. M. Di Paola, M. Bomers, N. Balakrishnan, A. V. Velichko, O. Makarovsky, M. Capizzi, M. Kesaria, A. Krier, T. Taliercio and A. Patanè: "Mid-Infrared Surface Plasmon Polaritons in a Novel Highly Doped Semiconductor"; *UK Semiconductors 2018*, Sheffield (UK); **07/2018**.
5. D. M. Di Paola, M. Bomers, N. Balakrishnan, A. V. Velichko, O. Makarovsky, M. Capizzi, M. Kesaria, A. Krier, T. Taliercio and A.

Patanè: “Mid-Infrared Surface Plasmon Polaritons in a Novel Highly Doped Semiconductor”; *Photonics on the Lake*, Windermere (UK); **07/2018**.

6. D. M. Di Paola, M. Bomers, N. Balakrishnan, M. Capizzi, A. V. Velichko, O. Makarovsky, L. Cerutti, A. Baranov, M. Kesaria, A. Krier, T. Taliercio and A. Patanè: “Mid-Infrared Surface Plasmon Polaritons in a Novel Highly Doped Semiconductor”; *ICPS 2018 - 34th International Conference on the Physics of Semiconductors*, Montpellier (France); **08/2018**.

Acknowledgments

I would like to express my most sincere gratitude to my supervisor Prof. Amalia Patanè, for always encouraging me to pursue excellence in research and for being a great role model.

My deepest gratitude also goes to my supervisor Dr. Oleg Makarovsky, for his valuable support and for always caring about my professional and personal growth.

I am extremely grateful to Prof. Laurence Eaves (The University of Nottingham) and Prof. Mario Capizzi (Sapienza Universitá di Roma) for sharing their lifelong experience and knowledge and for setting such high examples of work integrity and passion.

I thank my amazing colleagues and co-workers of Wendy House for creating a great working and human environment and for their daily presence in my life: Dr. Lyudmila Turyanska, Dr. Nilanthy Balakrishnan, Dr. Zakhar R. Kudrynskyi, Dr. Anton V. Velichko, Dr. Natalia Alexeeva, Garry Mudd, Jake Greener, Mahabub Bhuiyan, Debarati Mazumder, Chengxi Zhang, and Nathan Cottam.

I would also like to thank my fellow PROMIS ESRs: Eva Repiso Menendez, Denise Montesdeoca Cardenes, Mario Bomers, Mayank Sharma, Julie Tournet, Stefano Soresi, Atif Khan, Flavio Nucciarelli, Lucas Pinel, Shumitira Gandan, Salman Abdullah, Emna Amri, Shalini Gupta, Saeed Younis and Reza Arkani. Our common path and the precious experiences that we have shared have created strong bonds that I will always bring with me.

I would also like to acknowledge the support of our collaborators within the PROMIS ITN: Prof Thierry Taliercio (Université de Montpellier); Prof. Anthony Krier, Dr. Manoj Kesaria and Dr. Qi Lu (Lancaster University); Prof. Antonio Polimeni and Dr. Marco Felici (Sapienza Universitá di Roma); Dr. Giorgio Pettinari (CNR). I would also like to thank Dr. Susan Krier, Mr Allan Gordon and Ms Pamela Forster (Lancaster University) for their valuable support and assistance in organizing the PROMIS network. My gratitude also goes to Mr Martin Roe from the Nanoscale and Microscale Research Centre (nmRC) of the University of Nottingham, for the precious technical support and for his kind availability.

I acknowledge the University of Nottingham, the EU Marie Skłodowska-Curie ITN PROMIS (under grant agreement N° 641899), the Engineering and Physical Sciences Research Council (EPSRC) for funding this research work.

I will never be grateful enough to my parents and my brother, to my loving family, and particularly to Zia Antonietta; to my friends back home in Sicily and to those that I have found on my way in Trento, Pisa and Genoa, for being great companions in our path, through and in spite of the distance.

And finally, to my incredible friends in Nottingham, for giving a new meaning to the terms “caring” and “sharing”, and for always being by my side through the joyful and the difficult moments of this chapter of my life.

Physical constants

Quantity	Symbol	Value	Unit
Boltzmann constant	k_B	1.38065×10^{-23}	JK^{-1}
Electron charge	e	1.60218×10^{-19}	C
Electron mass in vacuum	m_0	9.10938×10^{-31}	kg
Permittivity in vacuum	ε_0	8.85419×10^{-12}	Fm^{-1}
Planck constant	h	6.62607×10^{-34}	Js
Reduced Planck constant ($h/2\pi$)	$\hbar$	1.05457×10^{-34}	Js
Speed of light in vacuum	c	2.99792×10^{8}	ms^{-1}

List of Contents

Abstract **i**

List of publications **ii**

List of conference abstracts **iii**

Acknowledgments **v**

Physical constants **vii**

List of Contents **viii**

1 Introduction **1**

1.1 Motivation 4

1.2 Thesis structure and overview 9

2 The effects of N- and H- incorporation in III-V semiconductors **11**

2.1 Nitrogen incorporation in III-V compounds 15

2.1.1 Band anticrossing model of the dilute nitride III-Vs 17

2.2 Hydrogen incorporation in III-V compounds 19

2.2.1 Hydrogen in dilute nitride III-N-V alloys 20

3 Quantum tunnelling and plasmonics **25**

3.1 Quantum tunnelling 26

3.1.1 Zener Tunnelling 27

3.1.2 Probing 0D states by magneto-tunnelling 31

3.1.3 Resonant tunnelling diodes (RTDs) 33

3.2 Plasmonics 38

3.2.1 Plasmonics in highly doped semiconductors (HDSCs) 43

4 Samples and experimental techniques 46

4.1 Samples 46

4.1.1 In(AsN) epilayers and hydrogenation 46

4.1.2 In(AsN)/(InAl)As *p*-*i*-*n* resonant tunnelling diodes 49

4.2 Experimental techniques: transport studies 50

4.2.1 Current-voltage (*I*-*V*) measurements 50

4.2.2 Low-temperature magneto-tunnelling spectroscopy 51

4.3 Experimental techniques: optical studies 54

4.3.1 Raman spectroscopy 54

4.3.2 Reflectance spectroscopy 57

4.3.3 Electroluminescence (EL) spectroscopy 59

4.4 Experimental techniques: topographical studies 62

4.4.1 Scanning electron microscopy (SEM) 62

4.4.2 Atomic force microscopy (AFM) 65

5 Mid-infrared plasmonics in highly H-doped In(AsN) 67

5.1 Introduction 67

5.2 Reflectance spectroscopy of surface plasmon polaritons 68

5.3 Raman spectroscopy of plasma modes 76

5.4 Tuning plasma modes by laser annealing 79

5.5 Summary 82

6 Dissociation of the N-H complex by electron beam annealing 84

6.1 Electron beam annealing of In(AsN):H 84

6.2 Mapping the H-distribution by Raman spectroscopy 87

6.3 Temperature-dependent electron annealing studies 90

6.4 Summary 94

7 Resonant Zener tunnelling via zero-dimensional states in an In(AsN) diode 96

7.1 Introduction 96

7.2 Negative differential resistance in In(AsN)/(InAl)As RTDs 97

7.3 Resonant Zener tunnelling through N-induced zero-dimensional states 99

7.4 Magneto-tunnelling spectroscopy of zero-dimensional states 102

7.5 Summary 110

8 Electroluminescence studies of In(AsN) resonant tunnelling diodes 112

8.1 Electroluminescence (EL) of In(AsN)/(InAl)As RTDs 112

8.2 Modelling charge injection and recombination 120

8.3 Summary 128

9 Conclusions and future directions **130**

9.1 MIR plasmonics with the highly doped In(AsN):H 131

9.2 Novel approach for H-removal with e-beam annealing 132

9.3 Resonant Zener tunnelling via 0D states in In(AsN) RTDs 134

9.4 Electroluminescence (EL) studies of In(AsN) RTDs 135

9.5 Future directions 136

9.5.1 Novel approach to MIR plasmonics 137

9.5.2 Towards an understanding of N-related defects 139

Appendix A Electronic bound states in a quantum well **141**

Appendix B Laser induced lattice heating **147**

Bibliography **150**

Chapter 1

Introduction

The engineering of band properties in semiconductors is a focus of research in condensed matter physics[1-4]. This is routinely done by the controlled incorporation of impurities in the crystal[5, 6]. Within this context, the incorporation of small quantities of nitrogen ([N] < 3%) into the group-V sublattice of III-V semiconductors has recently attracted increasing attention due to several effects of both fundamental and technological relevance[7, 8]. N-incorporation induces a reduction of the band gap energy of these dilute nitrides alloys due to the hybridization between the extended conduction band (CB) states of the host crystal with the localized N level[9-12]. This effect can be theoretically explained by several models, such as the so-called band anti-crossing (BAC) model[13-16]. The N-induced reduction of the band gap energy offers new routes for the tunability of the photonic response of semiconductor compounds, which is relevant for the realization of lasers, LEDs, and solar cells[17, 18].

Further remarkable effects are achieved by the combined incorporation of N- and H-atoms in III-V compounds. Nitrogen and hydrogen are ambivalent impurities for the III-Vs, but they can be used to tailor their properties such as the band gap energy, the carrier concentration and mobility. For example, the incorporation of H-atoms in dilute nitride alloys of III-V compounds can lead to the passivation of the electronic activity of the N-atoms. This is accounted for

by the creation of N-H complexes that was predicted theoretically[19-21] and observed experimentally[22]. The spatial control of these complexes can be achieved by using thermal annealing and/or masking techniques; these cause the dissociation of the N-H complexes and can thus be used to achieve the spatial profiling of fundamental band properties on the sub-micron scale[23-25].

Many studies have been conducted in order to investigate the combined effect of N- and H-incorporation on III-V compounds such as GaAs [19, 26, 27]. However, another member of the III-V family, the narrow gap InAs semiconductor, has received less attention and shows potential for novel and unexpected effects. For example, contrary to what is observed in other dilute nitride III-V alloys, such as Ga(AsN), Ga(PN) and (InGa)(AsN), the electronic activity of the N-atoms in In(AsN) is not neutralized upon H-incorporation[28-30]. Also, while the N-level lies close to the CB edge of Ga(AsN) and other similar compounds, thus acting as a resonant scattering centre, it lies well above the CB edge of In(AsN). Thus the non-resonant nature of the N-H complex in InAs enables to maintain high conductivity in hydrogenated In(AsN)[31]. Another appealing feature is that the electron density of In(AsN) increases by two orders of magnitude, up to 10^{19} cm^{-3}, following H-incorporation[31]. This enhancement is notably not observed in N-free InAs or reported for other dilute nitride alloys, and is attributed to the N-atoms, which act as traps for the H-atoms, forming N-H donor complexes within a thin (~ 0.1-1 μm) channel below the surface[32]. The unique behaviour of the hydrogenated In(AsN) among other similar compounds thus stimulates further studies in order to exploit novel effects that are still largely unexplored and not fully explained. The aim of this thesis is to present different novel effects observed in the InAs semiconductor following the incorporation of N- and H-atoms.

Firstly, we demonstrate that the increased electron density of In(AsN) following the *post-growth* H-incorporation can be used to reach high carrier concentrations and to excite a surface plasmon polariton (SPP) mode in the mid-infrared (MIR) spectral range that we detect with reflectance techniques. The plasmonic response of our highly H-doped In(AsN) semiconductor can be spatially tailored by focusing a laser beam onto the surface. This causes the dissociation of the N-H donor complexes, thus restoring the pristine condition of the non-hydrogenated In(AsN), as also probed by Raman spectroscopy studies. This approach enables the modulation of the electron density by controlling the chemical composition of a highly doped semiconductor by H-incorporation followed by laser writing on the μm-scale. This thesis also presents preliminary results on an alternative approach to the removal of H-atoms from highly H-doped In(AsN) by using the focused electron beam of a scanning electron microscope (SEM).

We also report on the effects of the incorporation of small quantities of N-atoms (nitrogen content [N] = 1%) in the intrinsic (*i*) quantum well (QW) layer of an In(AsN)/(InAl)As *p*-*i*-*n* resonant tunnelling diode (RTD). We observe a pronounced and extended negative differential resistance (NDR) in the current-voltage (*I*-*V*) characteristics of the RTD at voltages much lower than those required to reach flat band conditions. This additional NDR is not observed in N-free RTDs and is attributed to a novel type of resonant Zener tunnelling across the *p*-*i*-*n* diode, assisted by N-related zero-dimensional (0D) states. We probe the size of the 0D states by magneto-tunnelling spectroscopy (MTS), showing that these states are localized on the nanometre length-scale. Further to these findings, we investigate the role of these N-related states on the carrier injection and recombination in the RTDs by electroluminescence (EL) spectroscopy

studies. We observe EL in the MIR range (λ = 3-5 μm) up to room temperature. The EL signal is voltage-tuneable at temperatures T < 77 K; in addition, we observe up-conversion in the EL signal at temperatures 77 K < T < 300 K.

1.1 Motivation

Photonics, nanotechnology, advanced materials and advanced manufacturing technologies continue to have a profound impact on technological progress in the 21st century. These fields, identified as key enabling technologies (KETs) by the European Union (EU)[33], play a key role in the development and diffusion of ground-breaking technologies worldwide. The great impact of these fields on the global economy is proved by their huge market worth, which is today estimated to be around € 300 billion for photonics alone[34]. There is thus a great effort into translating and commercializing fundamental research discoveries into real life applications.

Semiconductor materials have been the backbone of an unprecedented technological and industrial revolution in the second half of the 20th century. A new impulse was given by advances in growth, processing and nanofabrication processes in the last decades. This has provided new means of tailoring semiconductor properties at the nanoscale, while the route of miniaturization of semiconductor devices has created a promising technological platform that has revolutionized our world on a global scale for a wide range of applications in photonics and electronics. Among these, one should mention communications (broadband connections, quantum cryptography and data protection for secure communications)[35], security (remote sensing applications, imaging and night vision for military, domestic or commercial demand)[36, 37] and energy management (monitoring of global warming with renewable energies,

especially efficient energy generation and harvesting in photovoltaic systems)[38, 39].

A crucial technological challenge in today's world is represented by the monitoring of environmental conditions[40]. The detection of small quantities of pollutants, whether it be greenhouse gases in the atmosphere or molecules/chemicals in water, requires the development of reliable, efficient, cost-effective and compact sensors[41, 42]. Thus there is currently a great effort to achieve a higher sensitivity, down to the the zeptamolar range of sensitivity, *i.e.* being sensitive to the order of ~1000 molecules per litre. This would have a huge impact on several areas: air/water quality monitoring; mapping of traffic, agricultural and landfill sites exhausts; detection of toxic and/or volatile species at power stations, production facilities, coal mines and disaster zones; detection of pipeline leaks; pharmaceutical processing and medical breath analysis[34, 43].

Within this context, it is especially important to develop novel materials and devices that can absorb and emit light in the mid-infrared (MIR) spectral range of the electromagnetic spectrum (*i.e.* in the wavelength range λ = 2-20 μm)[44, 45]. As a matter of fact, as shown in Figure 1.1, many bio-molecules and gas species have their vibrational–rotational absorption bands located in this range[43, 46-50]: methane (CH_4) at λ = 3.3 μm; hydrogen chloride (HCl) at λ = 3.55 μm; formaldehyde (CH_2O) at λ = 3.6 μm; carbon dioxide (CO_2) at λ = 4.2 μm; nitrous oxide (N_2O) at λ = 4.5 μm; carbon monoxide (CO) at λ = 4.66 μm; carbonyl sulphide (OCS) at λ = 4.86 μm; nitric oxide (NO) at λ = 5.3 μm; sulphur dioxide (SO_2) at λ = 8.7 μm; ozone (O_3) at λ = 10 μm; ethylene (C_2H_4) at λ = 10.5 μm; ammonia (NH_3) at λ = 10.6 μm.

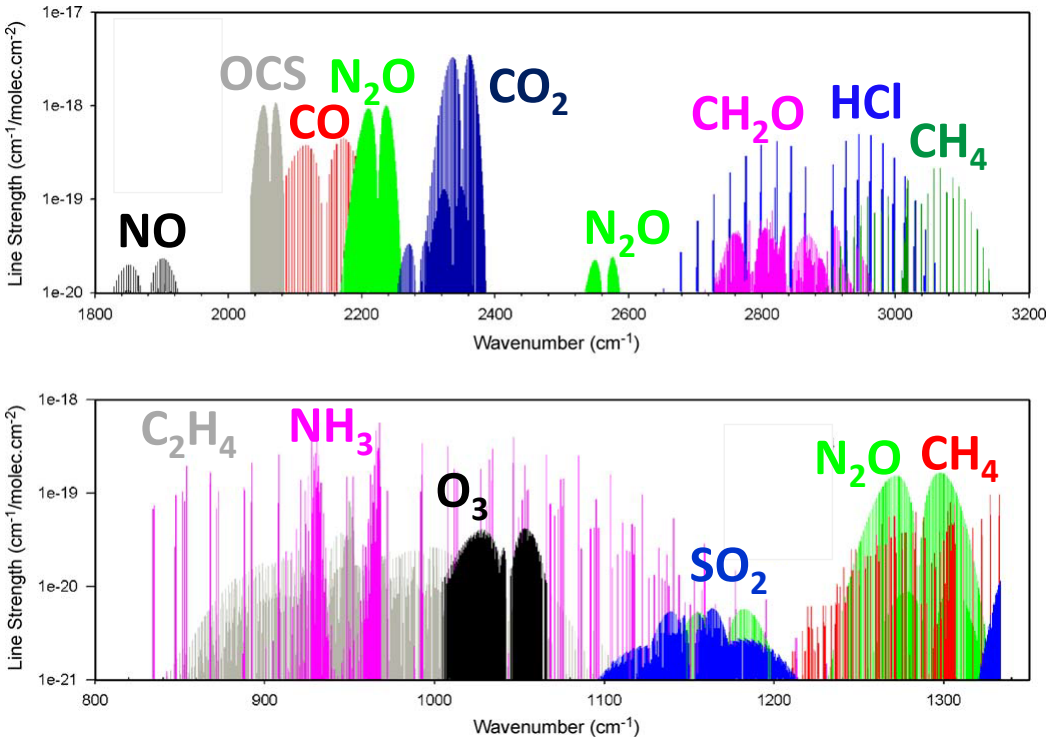


Figure 1.1: Absorption spectra of environmentally relevant gas species in the MIR spectral range. This range covers a substantial portion of the spectrum of fundamental vibrations of molecules[47].

Key requirements for trace gas sensing are high detection sensitivity, good spectral selectivity and fast response time[43, 48]. In particular, the spectral selectivity is achieved by using laser sources with narrow linewidth output. The MIR spectral range can be successfully covered by using novel semiconductor lasers, such as quantum cascade lasers (QCLs)[51-54] and interband cascade lasers (ICLs)[55-58]. These devices have been successfully designed to operate in pulsed or continuous wave mode and to enable high power output (of the order of tens to hundreds of mWs) with tuneable single mode emission and intrinsically narrow linewidths[59-61]. These features enabled the development of robust and reliable gas sensors achieving sensitivities down to parts per trillion by volume (pptv)[43, 48].

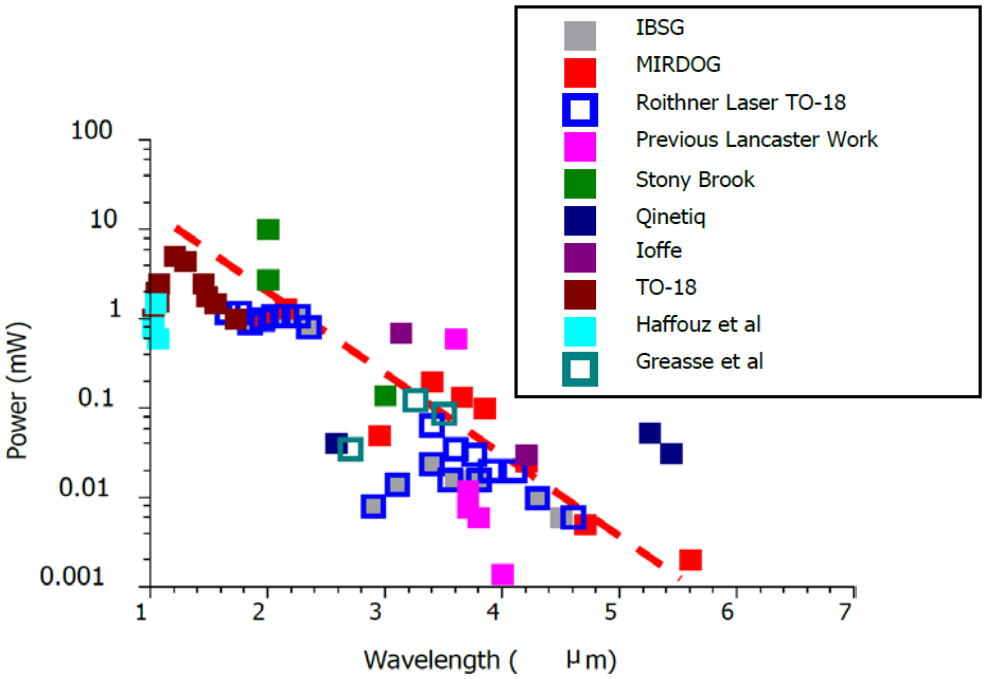


Figure 1.2: State-of-the-art for the room temperature output power of LEDs in the MIR spectral range[34].

Despite being successfully developed, QCLs and ICLs present a number of limitations due to their complexity and often prohibitive costs. For this reason, a great effort is put into finding more cost-effective alternatives. MIR light emitting diodes (LEDs) represent attractive candidates, given their price, robustness and lower power consumption, which are ideal for the realization of low-budget portable instrumentation[62, 63]. As summarized in Figure 1.2, the room temperature output power of MIR LEDs strongly decreases for λ > 2 μm[34]. The performance of MIR sources is limited by a generally low radiative efficiency due to thermal excitation of carriers and non-radiative Auger recombination[64-66]. The lack of suitable sources in the MIR (*i.e.* with output power > 1mW) leads to the use of much weaker (x100) molecular fingerprints in the near infrared (NIR) spectral range[34].

For these reasons, a deeper understanding of the band structure and of the related opto-electronic properties of novel MIR materials is crucial for the development and realization of suitable and reliable devices. Furthermore, as shown in Figure 1.3, the multi-billion worth market behind IR imaging and MIR sensors has been increasing steadily in the last decade and is expected to be growing significantly in the next years[67]. The translation of fundamental discoveries into commercially available devices would answer a deep request from the global market and is the main motivation of this research.

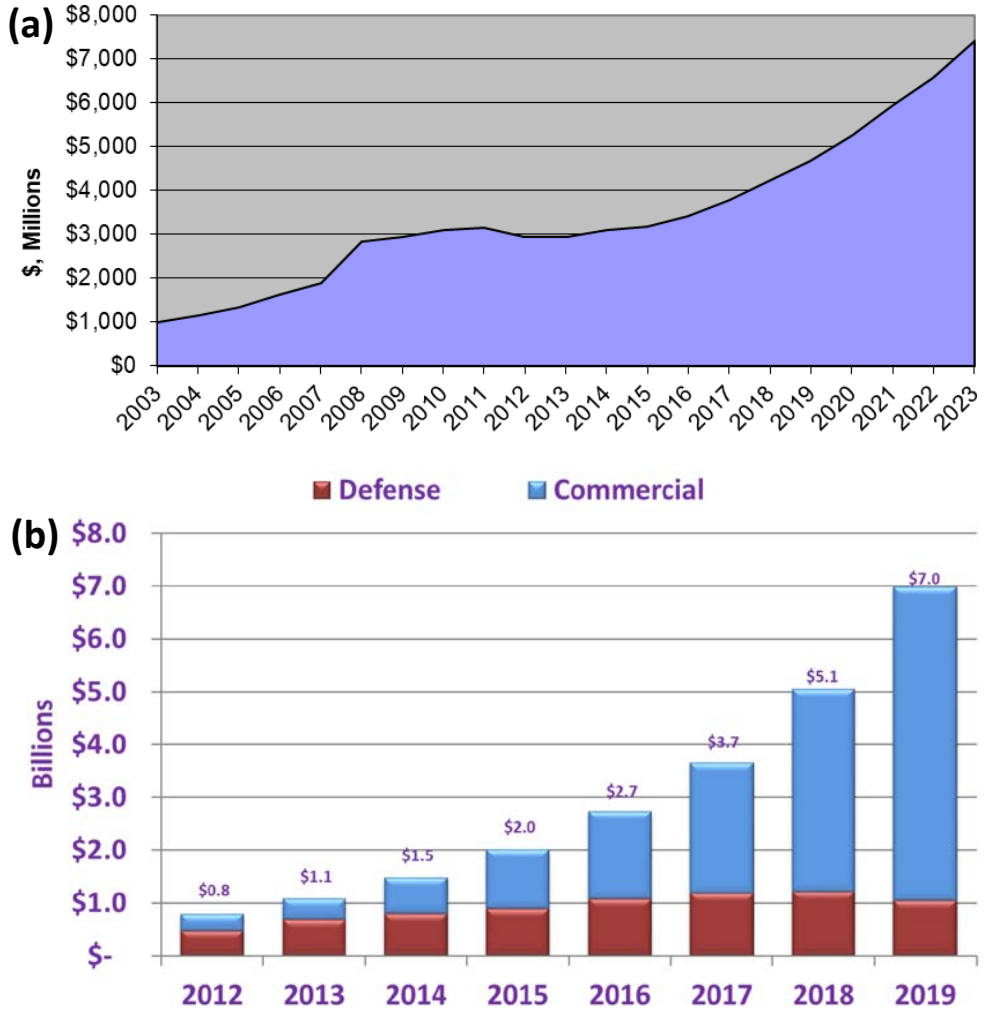


Figure 1.3: **(a)** World commercial and dual-use infrared (IR) imaging market. **(b)** MIR sensors market shipments[67].

1.2 Thesis structure and overview

This thesis is structured as follows.

Chapter 2 discusses the effect of the incorporation of nitrogen (N) and hydrogen (H) atoms in III-V semiconductors, focusing on the narrow gap InAs compound.

Chapter 3 presents the theory and modelling of physical phenomena of relevance for the topics discussed in this thesis. Firstly, a general theory of Zener tunnelling, magneto-tunnelling and resonant tunnelling diodes (RTDs) is presented. Then, fundamentals on plasmonics are presented, along with a discussion on the need of finding novel plasmonic materials.

Chapter 4 includes details on the growth and processing of the samples used for my studies and presents the experimental techniques used during my PhD.

Chapter 5 presents experimental data on a novel approach to plasmonics by using a highly doped semiconductor (HDSC). A surface plasmon polariton (SPP) mode in the MIR range is detected with reflectance techniques in hydrogenated In(AsN) epilayers. The plasmonic response can be suppressed by laser annealing, as assessed by Raman spectroscopy studies.

Chapter 6 presents an alternative approach to the removal of H-atoms from hydrogenated In(AsN) epilayers by using the focused electron beam of a scanning electron microscope (SEM).

Chapter 7 presents a study of a *p-i-n* In(AsN)/(InAl)As resonant tunnelling diode (RTD). We observe an extended negative differential resistance (NDR) in the current-voltage (*I-V*) curve of the diode. We attribute

this to a novel type of Zener tunnelling assisted by zero-dimensional (0D) N-related states, whose size is probed by magneto-tunnelling experiments.

Chapter 8 presents electroluminescence (EL) studies of In(AsN)/(InAl)As RTDs. We observe EL signal up to room temperature. These studies show a voltage-tuneable EL signal in the MIR spectral range (λ = 3-5 μm) at low temperatures (T < 77 K) and the occurrence of up-conversion luminescence (UCL) in the MIR EL signal over an extended range of temperature (77-300 K).

Chapter 9 concludes this thesis by providing a summary of the main findings and a proposal for future studies and directions.

This thesis contains 2 Appendixes. Appendix A describes the electronic bound states in quantum wells (QWs). Appendix B describes the calculation of the lattice heating induced by a focused laser beam.

Chapter 2

The effects of N- and H- incorporation in III-V semiconductors

The engineering of the band properties of semiconductor crystals has rapidly grown in the last decade[3, 4]. A widely used approach relies on the controlled incorporation of impurities and/or dopants in the crystal[5, 6]. This has enabled the observation of a wide range of tuneable electronic, optical and magnetic properties in condensed matter systems. The incorporation of impurities can be done during or after the crystal growth. However, achieving high levels of doping in a semiconductor is not a trivial task. Several factors contribute to limit the efficiency of this technique, such as the solid solubility of the dopants[6, 68] or doping compensation effects[69, 70]. In addition, the presence of impurities in a lattice tends to degrade the crystal quality and induce substantial internal losses, thus affecting key parameters such as the carrier mobility and limiting the performance of semiconductor devices. For these reasons, the study of impurities in semiconductors plays a key role in matching fundamental research with real device applications and presents challenges of both fundamental and technological interest.

Among semiconductors, most of light emitters (lasers, LEDs) are made using III-Vs[71]. These are binary compounds, formed by a group III metal (Al, Ga, In) and a group V anion (N, P, As, Sb), commonly disposed according to the zincblende crystal structure[72]. The historical relevance of the III-Vs relies

on the major impact of GaAs technologies[73]. However, also less explored III-V semiconductors show exciting properties. Most of the III-V semiconductors have a direct band gap, which is a key advantage for photonics, since it enables the efficient absorption and emission of light. Furthermore, several of these compounds, such as InSb and InAs, have small electron effective masses (0.014 m_e and 0.025 m_e at the Γ point, respectively), which makes them excellent candidates for high mobility applications[74, 75]. Given these and many other appealing features, III-V compounds have found use in a wide range of technologies and applications, such as transistors, mobile phones and other high-frequency electronic components[71].

Figure 2.1a shows the band gap energy vs lattice constants of the members of the III-V family. These materials offer tunability over a wide range of band gap energies, E_g, from the UV to the IR spectral ranges of the electromagnetic spectrum. Moreover, as shown in Figure 2.1b, the stacking of different materials to realize heterostructures provides a wide range of different band alignment configurations, according to the discontinuity between the conduction (E_C) and valence (E_V) band edges[76]. In type-I/straddling alignment (as for GaAs/(AlGa)As or AlSb/GaSb) both electrons in the conduction band (CB) and holes in the valence band (VB) are confined in the same quantum well (QW) layer; the quantum confinement enables the recombination of the electron and hole states bound in the QW, and the emitted luminescence can be tuned by changing the QW width[77-80]. In particular, a two-dimensional electron gas (2DEG) can be formed at the interface of a doped GaAs/(AlGa)As heterojunction[77]; this low dimensional system retains high mobility and has a unique historical relevance, since it represents the core of the so-called

modulation-doped field effect transistors (MODFETs), also known as high electron mobility transistors (HEMTs)[81-84]. In type-II/staggered alignment (for example InAs/AlSb or GaAs/GaSb), only one carrier type is confined; this configuration can be used in type-II quantum dots (QDs)[85-87]. Finally, in type-III/broken gap alignment (*e.g.* InAs/GaSb), the CB of one material overlaps with the VB of the other, thus facilitating the transfer of carriers through the interface. For this reason, the type-III band alignment is commonly used for the realization

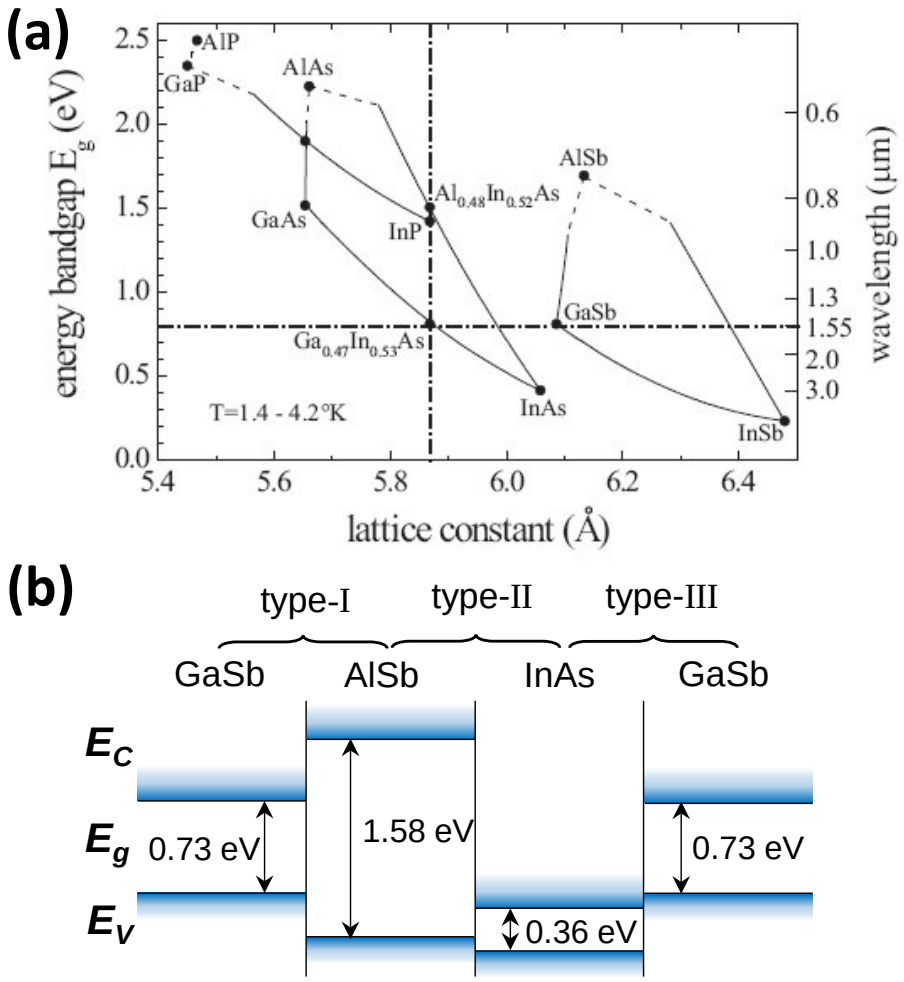


Figure 2.1: **(a)** Band gap energy vs. lattice constant for some III-V compounds. The continuous and dashed lines represent the direct and indirect band gaps of the ternary compounds, respectively[88]. **(b)** Alignment of conduction (E_C) and valence (E_V) band in different III-V heterojunctions at T = 300 K.

of tunnel junctions[89] and tunnel field effect transistors (TFETs)[90, 91].

The epitaxial growth of III-Vs is a well-established technique that enables the growth of heterostructures with monolayer accuracy[92]. Several of these III-V compounds have very similar lattice constant, a, required for epitaxial growth by molecular-beam epitaxy (MBE), metalorganic vapour phase epitaxy (MOVPE), etc. The possibility of growing lattice-matched and lattice-mismatched heterostructures enables the fabrication of a large variety of low-dimensional structures, such as two-dimensional (2D) quantum wells (QWs), one-dimensional (1D) quantum wires (QWis) and zero-dimensional (0D) quantum dots (QDs). The growth of ternary or quaternary or even quinary compounds is also possible (represented by the solid and dashed lines in Figure 2.1a). This provides opportunities for additional band engineering and further widens the range of the accessible electronic and optical properties of III-V semiconductors.

Among the different approaches for the controlled incorporation of impurities in III-V compounds, the incorporation of small quantities of nitrogen (N) atoms to form the so-called dilute nitride alloys has lately gained considerable attention due to unique effects of both fundamental and technological relevance[65, 93] (Section 2.1). Some of these effects, such as the reduction of the band gap energy with increasing N-content ([N])[94] can be theoretically explained by using the simple band anticrossing (BAC) model[13-15], presented in Section 2.1.1. This chapter also discusses the peculiar effects of the hydrogen impurity in semiconductor crystals (Section 2.2), and particularly in the dilute nitrides of III-Vs (Section 2.2.1).

2.1 Nitrogen incorporation in III-V compounds

Dilute nitride alloys of III-V semiconductors, such as Ga(AsN), (InGa)(AsN), Ga(PN), and (InGa)(PN), have attracted a lot of attention lately due to their peculiar electronic and optical properties[7, 8]. These compounds are obtained by the incorporation of relatively low quantities of N-atoms (nitrogen content [N] < 3%) in the group V anion (As, P) sublattice. In this thesis, I focused my attention on the largely unexplored dilute nitride alloy of InAs. This III-V semiconductor presents a direct narrow energy band gap (E_g = 0.415 eV at T = 4.2 K)[95], corresponding to light absorption in the mid-infrared (MIR) spectral range of the electromagnetic spectrum. This compound has one of the smallest electron effective masses among the III-Vs (m_e^* = 0.025 m_e at the Γ valley)[96] that is only weakly affected upon N-incorporation[97]. These properties make the dilute nitride In(AsN) a promising candidate for high-mobility applications in MIR photonics[18].

Figure 2.2a shows the unit cell of In(AsN). Here the In- and As- atoms are disposed according to the zincblende crystal structure. N-atoms can either be incorporated in place of As-atoms (substitutional nitrogen, N_{sub} in Figure 2.2a) or sit interstitially out of the crystal sites (N_{int} in Figure 2.2a). A smaller lattice constant usually induces an increase of the energy bandgap. However, the incorporation of the small and highly electronegative N-atoms in III-Vs leads to a large local perturbation of the potential in the lattice[15] resulting in large and composition-dependent bowing of the band gap energy[94, 98]. This induces the decrease of the band gap energy with increasing N-content[99] (indicated as *x* in Figure 2.2b). This effect is due to the creation of a localized N-level above the conduction band (CB) edge of the host III-V matrix.

Many of the effects arising from the N-incorporation in III-Vs can be explained by using a simple band anticrossing (BAC) model[13-15]. According to this model, the extended CB edge states admix with the localized N-level. This interaction leads to the splitting of the CB into two hybridized subbands, resulting in the red-shift of the CB edge. A more formal treatment of the BAC model is given in Section 2.1.1. The reduction of the band gap energy with increasing nitrogen content, [N], was observed experimentally by several techniques, such as photoluminescence (PL)[10, 11] and photoreflectance[12] spectroscopy (Figures 2.3a and 2.3b, respectively).

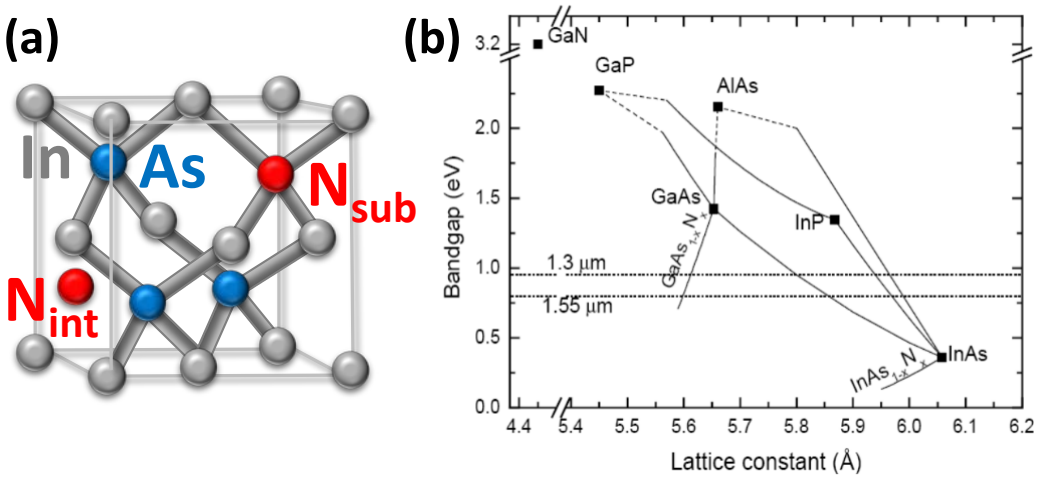


Figure 2.2: **(a)** Unit cell of InAs (zincblende structure), where N-atoms are incorporated in one of the group V sublattice sites in place of an As-atom (N_{sub}) or sit interstitially in the crystal (N_{int}). **(b)** Band gap energy vs lattice constant for various III-Vs. The continuous and dashed lines represent the direct and indirect band gaps of the ternary compounds, respectively. The band gap energy of Ga(AsN) and In(AsN) decreases with increasing nitrogen content, indicated as x[100].

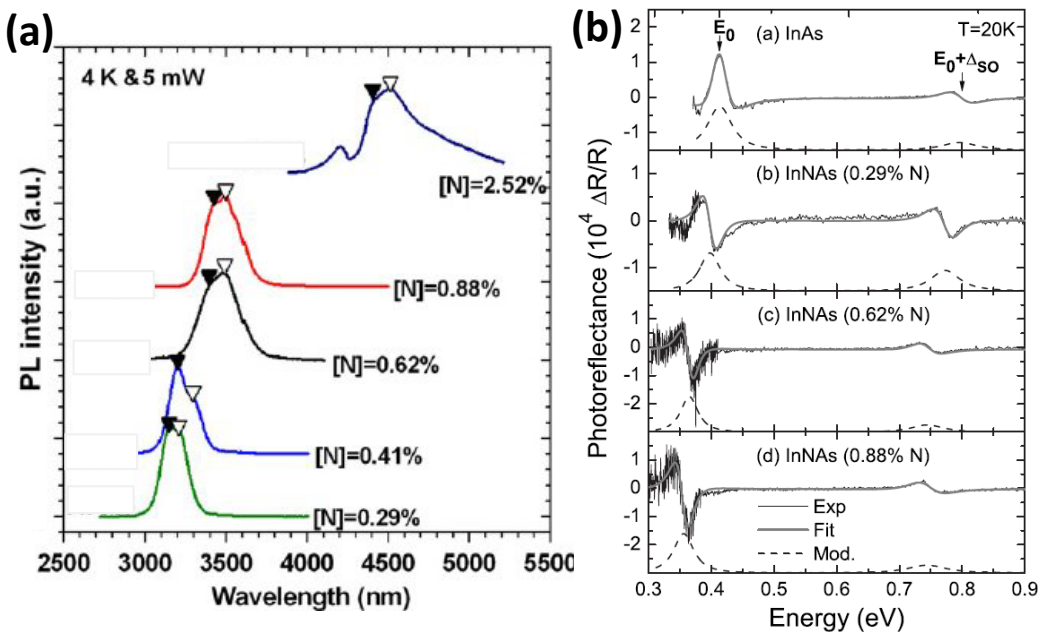


Figure 2.3: Photoluminescence[11] **(a)** and photoreflectance[12] **(b)** spectra of In(AsN) epilayers, showing the reduction of the band gap energy with increasing nitrogen content, [N]. Solid and open triangles in (a) denote the positions of the double-peak photoluminescence emissions.

2.1.1 Band anticrossing model of the dilute nitride III-Vs

The two-level band anticrossing (BAC) model has been extensively applied to estimate the effect of the dilute N-incorporation in III-V alloys[13-15]. This is done by applying degenerate perturbation theory to a system of extended electronic states of the host matrix and localized states. The interaction between these electronic states is described by the following eigenvalue problem:

$$\begin{vmatrix} E(k) - E_M(k) & V_{NM} \\ V_{NM} & E(k) - E_N \end{vmatrix} = 0 \,, \qquad (2.1)$$

where $E_M(k)$ and E_N are, respectively, the energies of the CB states of the host material and of the N-level, measured with respect to the VB maximum; $V_{NM} = \langle M|V|N\rangle$ is the matrix element describing the interaction between the localized N-states ($|N\rangle$) and the extended CB states of the host material ($|M\rangle$), and V is

the potential generated by a single N-atom on a substitutional site. The two solutions of this problem are given by:

$$E_{\pm} = \frac{1}{2}\left\{(E_N + E_M(k)) \pm \sqrt{\left[\left(E_N - E_M(k)\right)^2 + 4V_{MN}^2\right]}\right\}. \quad (2.2)$$

Assuming that the matrix element V_{NM} does not depend on the wavevector k near the CB edge, it can then be expressed as $V_{NM} = C_{NM} \times [\mathrm{N}]^{1/2}$, where C_{NM} is a constant (that depends on the host matrix) and [N] is the fraction of substitutional nitrogen. Equation 2.2 can thus be rewritten as:

$$E_{\pm} = \frac{1}{2}\left\{(E_N + E_M(k)) \pm \sqrt{\left[\left(E_N - E_M(k)\right)^2 + 4C_{MN}^2 \times [\mathrm{N}]\right]}\right\}. \quad (2.3)$$

The dispersion of the $E_{\pm}$ mode is shown in Figure 2.4a for the dilute nitride In(AsN) alloy with [N] = 1%: for $k \to 0$, the E_+ solution (solid blue line) is close to the localized N-state (horizontal black dashed line), while the E_- solution (solid red line) represents the CB edge, redshifted due to the admixing of the extended CB states of the host matrix (black dashed curve) with the localized N-impurity. The reduction of the band gap energy of InAs as a function of [N], as estimated by the BAC model, is shown in Figure 2.4b for [N] < 3%. For this calculation, we consider E_N to lie 1.44 eV above the VB maximum and C_{NM}= 2.0 eV[101, 102]. Note that this model only considers the effect of the localized N-state on the CB states and neglects the effects on the VB. Indeed, photoreflectance studies have proven experimentally the weak influence of the N-level on the spin-orbit (SO) splitting of In(AsN)[12].

The BAC model represents a very simple approach to the description of the interaction between the localized N-states and the extended CB states of the host material. More complex models, considering the formation of nitrogen clusters, have been developed to account for a better description of the band

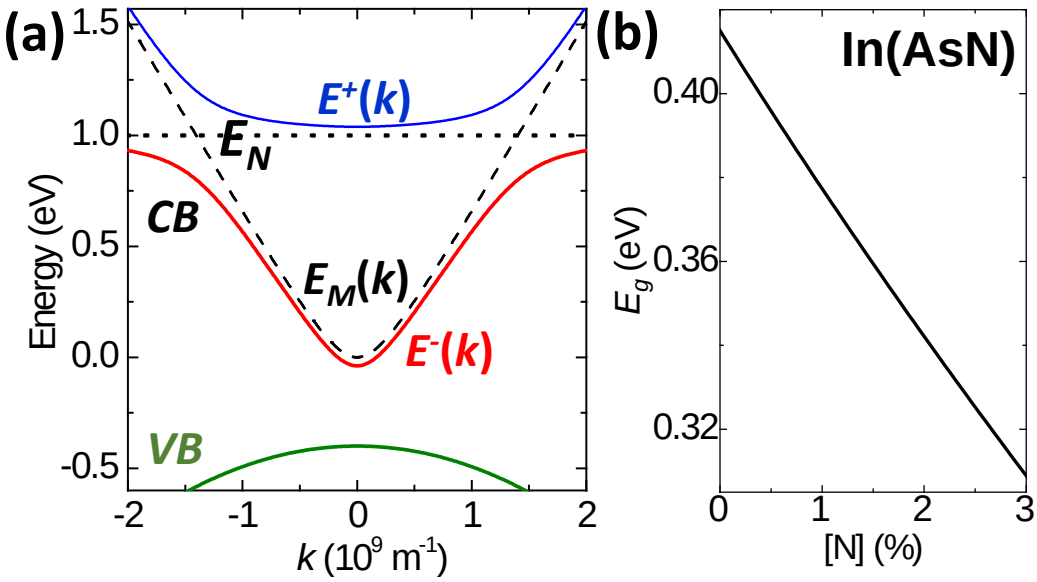


Figure 2.4: **(a)** Dispersion of the $E_{\pm}$ modes (blue and red solid lines) in the BAC model for In(AsN) with nitrogen content [N] = 1%. These modes arise from the interaction between the CB states of InAs (black dashed curve) and the localized N-state (horizontal black dotted line). **(b)** Dependence of the band gap energy, E_g, of In(AsN) on nitrogen content, [N].

structure[16, 103]. A many-impurity Anderson model was also developed, considering the effect of localized states arising from defects that are randomly distributed in the crystal. The solutions to this problem provide the dispersion relations for the hybridized subband states, while the imaginary part of Green's function accounts for the broadening effects[104].

2.2 Hydrogen incorporation in III-V compounds

The behaviour of hydrogen (H) atoms in different classes of materials (semiconductors, insulators, aqueous solutions…) has attracted great interest due to unique effects on their structural, electronic and optical properties[105]. It is also well known that the unintentional incorporation of H-atoms occurs during

the growth of semiconductor crystals or their processing into devices[106, 107]. This has stimulated intensive studies of H-incorporation for a deeper understanding of the way hydrogen combines with the host crystal matrix of different semiconductors[108-110], such as Si[111, 112], as well as in zero-gap semiconductors, like graphene[113], or insulators, like diamond[114]. Hydrogen also has a strong effect as a dopant or on the passivation of dopants in wide-bandgap semiconductors[115] such as InN[116], GaN[117] and (InGa)N[118].

Interesting effects also arise upon H-incorporation in III-V compounds[105]. For example, H-atoms have a profound impact on the behaviour of dopants (such as C, Si, Zn) in GaAs[119, 120]. C-atoms are routinely used as *p*-type dopants in GaAs, where they tend to sit on the As-site, thus behaving like acceptors; the incorporation of H-atoms was shown to passivate the C-dopants by the creation of C-H complexes[119, 121, 122]. A similar effect was observed in the ternary (InGa)As alloy[123]. The formation of H-related complexes in *post-growth* hydrogenated GaAs, (AlGa)As and (InGa)As is strongly supported by photoluminescence (PL) experiments[124]. The introduction of the H-impurity in GaAs also induces the formation of both donor and acceptor states near the conduction and valence band edges, respectively[125], as also confirmed by PL studies[126].

2.2.1 Hydrogen in dilute nitride III-N-V alloys

Interest in the behaviour of the small, highly diffusive and electronically active hydrogen atom in crystals has received a renewed impulse from the even more striking effects that the H-irradiation has on dilute nitride alloys, such as Ga(AsN), Ga(PN), and (InGa)(AsN)[28, 29, 127]. As presented in Section 2.1, the incorporation of N-atoms induces strong modification of the structural,

electronic and optical properties of III-V compounds. However, many of these properties can be recovered upon H-incorporation in the III-N-V alloys. Thus hydrogen tends to passivate the electronic activity of N-atoms, restoring the pristine crystal[22, 128]. This passivation can be accounted for by the formation of N–H_n complexes ($n \geq 2$), which was theoretically predicted[19-21] and confirmed experimentally[22]. The thermal diffusion of H-atoms in the host crystal was studied by secondary-ion mass spectrometry (SIMS) to correlate the H-diffusion profile with the hydrogenation conditions, such as temperature, T_H, hydrogen beam energy, E, and dose, D_H [28].

These effects have been extensively exploited. For example, the selective hydrogenation of III-N-V crystals using mask techniques enables the spatial control of the band gap at the nanoscale. An appealing approach also exploits a laser writing techniques to dissociate the N–H_n complexes and thus achieve band gap profiling at the μm-scale[26, 27, 127-130]. This offers new routes to band gap engineering and a novel approach to device fabrication.

It is worth noting that, unlike for Ga(AsN):H, where the kinetics and energetics of the N–H_n complexes has been extensively studied[19, 20, 22, 120, 131], the nature and exact configuration of these complexes is still largely unexplored in other compounds. For example, the hydrogenated In(AsN) alloy presents a peculiar and unique behaviour. Notably, the H-irradiation does not neutralize the electronic activity of the N-atoms, contrary to what observed in other dilute nitride alloys, such as Ga(AsN), Ga(PN), and (InGa)(AsN)[28, 29]. Thus the band gap energy of In(AsN) does not change upon H-incorporation[30]. This may partially arise from the different position of the N-level in InAs, which lies well above (~ 1 eV) the CB minimum[101], whereas it lies close to the CB minimum

of other dilute nitrides such as Ga(AsN)[104], as shown in Figure 2.5. The unusually high position of the N-level in In(AsN) enables the creation of N-H complexes with donor states far from resonance with the conduction electrons. The non-resonant nature of the N-H complex thus enables to retain low electron scattering rates and high electron mobility (μ_e> 10^3 cm^2V^{-1} s^{-1}) even for high impinging doses of the H-atoms[31, 32]. Further theoretical models are required to determine the nature and configuration of N–H_n complexes in In(AsN):H, as well as experimental verifications. This would give a renewed impulse to the exploitation of effects so far unique and unobserved in other III-Vs[30].

Another interesting effect is the increase of the electron density, n_e, of In(AsN) by two orders of magnitude, up to $n_e \sim 10^{19}$ cm^{-3}, following the incorporation of hydrogen[31] (Figure 2.6b). This enhancement is notably not observed in N-free InAs or reported for other dilute nitride alloys, and is attributed to the formation of N-H donor complexes (sketched in Figure 2.6a) within a thin channel below the surface[32]. These N-H complexes are stable under normal conditions and do not degrade with time[30]. Secondary ion mass spectroscopy (SIMS) has shown that the H-distribution has a box-shaped

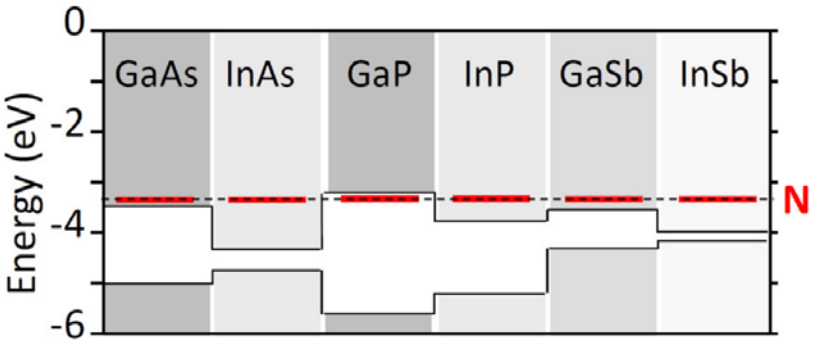


Figure 2.5: Band lineups for different members of the III-V family. For each material, the upper/lower lines represent the CB minimum/VB maximum, respectively; the horizontal red lines indicate the substitutional N-level[127].

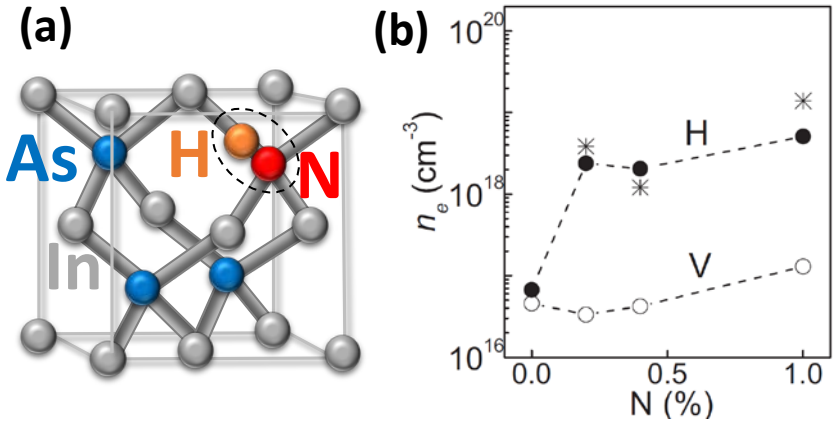


Figure 2.6: **(a)** Sketch of the N-H donor complex in In(AsN) after irradiation of a H-ion beam. **(b)** Dependence of the electron density, n_e, of In(AsN) on the nitrogen content, [N], before (V) and after (H) hydrogenation[31]. The values of n_e are derived from the analysis of the Shubnikov-de Haas oscillations (asterisks) and the Hall resistance (dots and circles).

form[30, 32], from which the H-penetration depth can be estimated (Figure 2.7a). The box-like SIMS profile differs from the Gaussian profile commonly observed in conventional semiconductors[132] and it arises from the presence of the N-atoms, which act as H-traps. The penetration of H-atoms in the lattice can be controlled by the N-content and by changing the hydrogenation conditions, such as the temperature (T_H), the H-ion beam energy (E) and dose (D_H)[30]; a similar behaviour is also observed in the dilute nitride Ga(AsN) alloy[28]. The effect of N-atoms, acting as traps for the diffusion of the H-atoms, is reflected by the SIMS profile, whose forefront becomes sharper with increasing N-content; for [N] > 1%, the intensity profile tends to reduce by an order of magnitude within 10 nm

Figure 2.7b shows the different effect of the H-irradiation on N-free InAs and In(AsN). In N-free InAs (dashed line in Figure 2.7b), the bending of the CB

edge leads to the formation of a two-dimensional electron gas near the surface[133]. On the other hand, the incorporation of hydrogen in In(AsN) (solid lines in Figure 2.7b) leads to the formation of a well-defined subsurface region with a three-dimensional electron gas, as estimated by solving Poisson's equation[32].

All these features make the highly doped In(AsN):H alloy a promising candidate for applications exploiting its H-enhanced conductivity, such as plasmonics in the MIR spectral range for gas sensing[49, 50, 134]. Further details on the growth and hydrogenation of our In(AsN) epilayers are given in Section 4.1.1. In Chapter 5, we demonstrate that In(AsN):H can support a MIR surface plasmon polariton (SPP) mode and that the plasmonic resonance can be spatially tailored and suppressed by photo-annealing, thus paving the way for the patterning of plasmonic properties by the incorporation of H-atoms and their selective removal by laser writing.

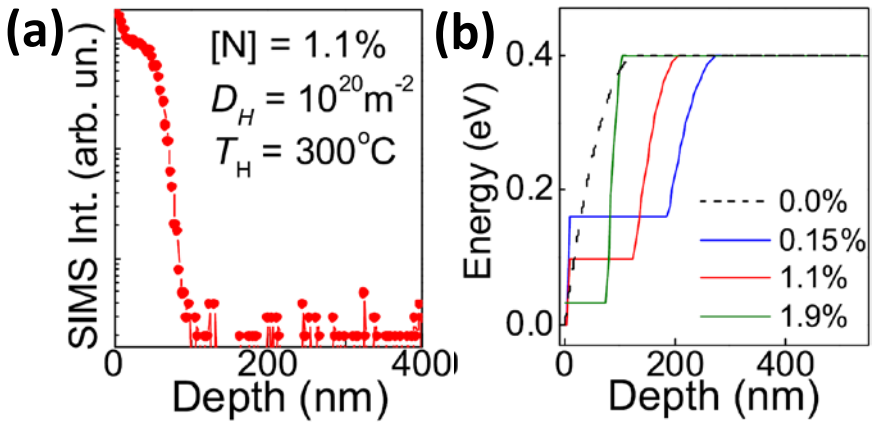


Figure 2.7: **(a)** SIMS profile of ^{2}H in In(AsN) with [N] = 1.1%, D_H = 10^{20} ions/cm^2, t_H = 9 min, T_H = 300 °C [32]. **(b)** Simulations for the bending of the CB for InAs (dashed line) and In(AsN) (full lines) upon hydrogenation, as derived from Poisson's equation[32].

Chapter 3

Quantum tunnelling and plasmonics

This chapter describes fundamental physical phenomena that are relevant for the semiconductor systems studied during my PhD. My project explores the transport and electronic properties of novel mid-infrared (MIR) materials and devices. In particular, I focused on the effects of the incorporation of nitrogen (N) and hydrogen (H) atoms in the narrow gap InAs semiconductor alloy, which are probed by tunnelling and MIR plasmonics.

In the following, we discuss some relevant aspects of quantum tunnelling (3.1). We present the basic physical principles of Zener tunnelling (3.1.1). Magneto-tunnelling (3.1.2), *i.e.* tunnelling under the effect of an applied magnetic field, represents a powerful tool to probe zero-dimensional (0D) states in semiconductors. Furthermore, the physical principles behind resonant tunnelling diodes (RTDs) and their relevance for semiconductor devices are presented (3.1.3). The fundamentals of plasmonics are presented in Section 3.2, along with the search for alternative low-loss materials for MIR plasmonics (3.2.1). Within this context, the highly H-doped In(AsN) compound represents a promising candidate among the highly doped semiconductor (HDSC) family for MIR sensing applications.

3.1 Quantum tunnelling

The phenomenon of tunnelling of a charged particle through an energy potential barrier represents one of the most impactful achievements related to the theory of quantum mechanics. As a matter of fact, it is not only a major conceptual validation of the theory, but its exploitation has also played a key role in the development of nanotechnologies relying on quantum phenomena. Within this context, the interband tunnelling of carriers through a forbidden energy gap in insulators/semiconductors, also known as Zener tunnelling, is of particular historical relevance. First theoretically predicted by Zener in 1934[135], it was experimentally observed in the Esaki diode in 1957[136] as the first demonstration of quantum tunnelling in a condensed matter system. The effect of tunnelling in a diode in forward bias regime, giving rise to a negative differential resistance (NDR) region[132], is further discusses in Section 3.1.3. Notably, the phenomenon of tunnelling in reverse bias is crucial for the exploitation of Zener diodes, whose current-voltage, *I-V*, characteristic is depicted in Figure 3.1. In reverse bias, Zener diodes exhibit a controlled breakdown, enabling to keep the voltage around the Zener breakdown voltage,

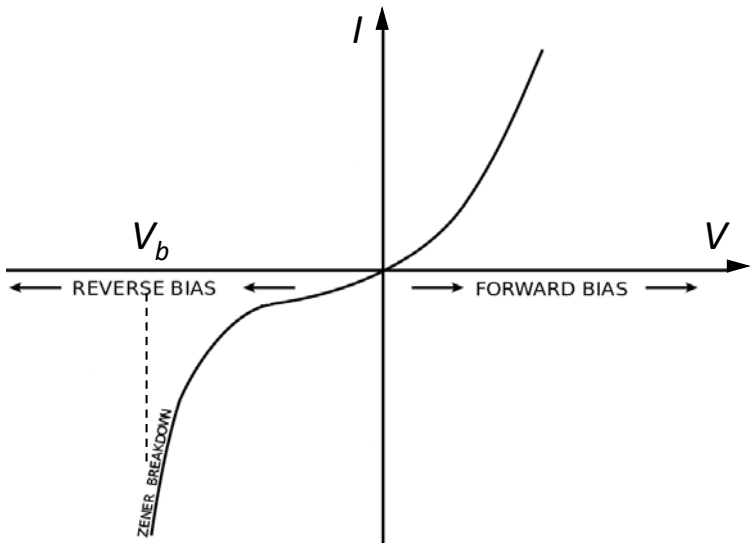


Figure 3.1: Current-voltage (*I-V*) characteristic of a Zener diode.

V_b, for a wide range of currents. For this reason, Zener diodes are routinely used as reference voltages or as voltage stabilizers[137]. More recently, Zener tunnelling has received renewed interest in nanotechnologies due to its impact on the properties and performance of semiconductor devices at the nanoscale.

3.1.1 Zener Tunnelling

The study carried out by Zener deals with the effect of an external electric field on the motion of electrons in a periodic semiconductor/insulator crystal[135]. In particular, it focuses on the possibility of electrons to make a transition from a filled to an unfilled energy band thanks to the band bending arising from the external electric field[135]. In normal conditions, a certain number of electrons are promoted to excited states due to thermal excitation and/or impurities in the crystal; their number is, however, too small to enable feasible current flows in devices under normal external field conditions.

The motion of electrons in a crystal is determined by the electron energy, E, and wavevector, k, which is real if $E(k)$ lies within allowed energy bands, thus leading to extended wave functions. On the other hand, whenever k lies within a forbidden energy bandgap, k is complex and the wave function probability density distribution decreases exponentially in real space[135]. More formally, Zener's theory starts from the Bloch theorem, which states that the wave function in a crystal periodic potential can be factorized as a plane wave and a function, $U_k(x)$, with the same spatial periodicity, a, of the crystal lattice:

$$\psi_k(x) = e^{ikx}\, U_k(x)\,. \tag{3.1}$$

When an external electric field, F, is applied, the motion of an electron is described by a wave packet of energy ω_B, where ω_B is the so-called Bloch frequency:

$$\omega_B = eFa/h\ , \tag{3.2}$$

where *h* is the Planck constant. This frequency describes how frequently the electron is reflected by an ideal lattice with no scattering centres. At every reflection there is a finite probability, *p*, that the electron tunnels into an excited state. The probability by unit time, *γ*, that the electron is excited to an upper level is given by

$$\gamma = p\ \omega_B\ . \tag{3.3}$$

To calculate *γ*, let us start from the Schrödinger equation for an electron of energy *E* and mass *m*, under the effect of an electric field, *F*, in a periodic potential, *V(x)*[135]:

$$\left\{\frac{-\hbar^2}{2m}\frac{\partial^2}{\partial x^2} + V(x) + (eFx - E\right\}\psi(E,x) = 0\ . \tag{3.4}$$

Provided that the electric field term, *eFx*, changes smoothly over a single lattice constant length, an approximate solution to Equation 3.4 is given by

$$\psi(E,x) = e^{i\int k(x)\,dx}\ U_k\ , \tag{3.5}$$

which can be seen as an extension of the Bloch solution in Equation 3.1. Note that, for a given energy *E*, *k* is real only for certain values of *x*. Also, the wave function increases or decreases exponentially in those regions where *k* is complex. By taking the physically meaningful solution, *i.e.* the one that decreases exponentially, the transition probability, *p*, for an electron of energy *E* that tunnels from a low to a high energy band through the forbidden energy gap is given by [135]

$$p = |\psi(x_C)/\psi(x_B)|^2\ , \tag{3.6}$$

where x_B and x_C are the classical turning points at energy *E* (Figure 3.2).

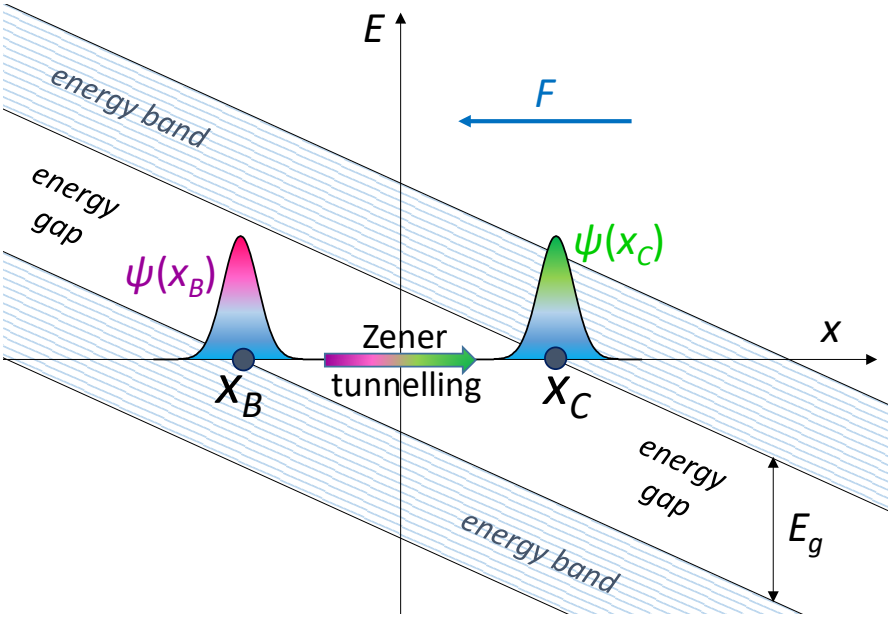


Figure 3.2: Schematic *E(x)* diagram of the energy bands of a crystal lattice under the effect of a uniform electric field, *F*. The shaded regions represent the allowed energy band states, separated by a forbidden energy gap. A sketch of the wave function probability density, $|\psi|^2$, is represented at the coordinates x_B and x_C, which are the classical turning points at a certain energy *E*.

By explicitly splitting the real, ξ, and imaginary, η, part of the wavevector[135]

$$k = \xi(x) + i\eta(x), \tag{3.7}$$

we get for the transition probability:

$$\gamma = \frac{eFa}{h} exp\left\{-2\int_{x_B}^{x_C} \eta(x)\, dx\right\}. \tag{3.8}$$

By choosing a reference frame whose origin, $x = 0$, lies midway between the classical turning points, we can write $x_B = -E_g/2eF$ and $x_C = +E_g/2eF$, where E_g is the band gap energy. With this notation, the complex wavevector is[135]

$$k = \left\{1 \pm i\frac{8ma^2}{h^2}\sqrt{\left(E_g/2\right)^2 - (eFx)^2}\right\}, \tag{3.9}$$

and the resulting transition probability is given by

$$\gamma = \frac{eFa}{h} exp\left\{-\frac{\pi^2}{h^2}\frac{ma^2E_g^2}{|eF|}\right\}. \quad (3.10)$$

A more formal treatment of the problem was given by Kane[138] by rewriting the time independent Schrödinger's equation under the effect of an electric field, *F* as:

$$\left[E_n(k) + ieF\frac{\partial}{\partial k_x} - E\right] a_n(K) + \sum_{n'} eF\chi_{nn'}(k)\, a_{n'}(k) = 0\,, \quad (3.11)$$

where $E_n(k)$ is the energy of an electron in the periodic lattice and *E* is the total energy. In this notation, the basis functions are Bloch's functions as in Equation 3.1, $\psi_n(k,x) = e^{ikx}\, U_n(k,x)$, labelled by the index *n*, and a_n are expansion coefficients. The position operator, $\hat{r}$, is split into an intraband ($i\,\partial/\partial k$) and interband ($\chi_{nn'}$) operator, respectively. The off-diagonal elements of the latter couple the periodic parts of Bloch's functions, labelled by the index *n* and wavevector *k*:

$$\chi_{nn'} = i\int U_n^*(k)\frac{\partial}{\partial k}U_{n'}(k)\, dr\,. \quad (3.12)$$

By integration of the interband terms over all the possible wavevectors, one gets the matrix elements, $M_{nn'}$, connecting two states at the same energy but belonging to different bands (*n* and *n'*)[138]:

$$M_{nn'} \propto \int \chi_{nn'}(k)\; exp\left\{-\frac{i}{eF}\int_0^{k_x}[E_n(k') - E_{n'}(k')]dk'_x\right\} dk_x\,. \quad (3.13)$$

By using Fermi's golden rule, one gets

$$\gamma = \frac{2\pi}{h}|M_{nn'}|^2 D(E) \quad (3.14)$$

where *D(E)* is the density of states of the system. Thus the probability by unit time, *γ*, of an electron transition from the band *n* to the band *n'* is directly proportional to the square modulus of the interband matrix element. Further theories have been developed to account for the bias and temperature

dependence of the direct[139] and indirect[140] interband tunnelling in semiconductor *p-n* junctions, as well as the effect of non-uniform electric fields across the junction[141].

This approach is used in Section 3.1.2 to model the tunnel current under the effect of an applied magnetic field. Notably, Kane also discusses the physical processes that can contribute to the so-called "excess current", namely the current flowing under non-resonant conditions between two energy bands without energy conservation[142]. The possible mechanisms that are envisaged for the energy loss and/or gain for electron tunnelling may involve photons, phonons, electrons or plasmons; however, in spite of being allowed or even observed, these effects are also too small to account for large current flows in forward bias in standard semiconductor *p-n* junctions[142]. On the other hand, the presence of energy states in the gap, arising from disorder, impurities and/or dislocations, can represent an important contribution to the current in forward bias[142]. In this work (Chapter 7), we report on the origin and role of "in-the-gap" N-related states and their effect on Zener tunnelling in In(AsN)/In(AlAs) RTDs[143].

3.1.2 Probing 0D states by magneto-tunnelling

Probing individual atoms or electron charge distributions in condensed matter systems is a research field of both theoretical and technical relevance. Sensitive techniques are currently used, such as scanning tunnelling microscopy (STM)[144], to probe the spatial form and size of the wave function of 0D states, created by individual impurities and quantum dots (QDs). However, STM represents an invasive and destructive method that is applied only for 0D states close to a surface, whereas dots that are incorporated into real semiconductor

devices need a different approach. Within this context, magneto-tunnelling spectroscopy (MTS)[145-147] represents a non-invasive and non-destructive approach to this problem. MTS exploits the effect of the classical Lorentz force on the motion of an electron tunnelling into a 0D state. It can be regarded as the counterpart of STM in momentum- (*k*-) space: in STM, a moving tip probes the wave function probability density in real space; in a similar way, in MTS, a magnetic field *B* is used to probe the electronic wave function probability density in *k*-space. As the magnetic field plays the role of the probing tip, MTS can be done inside a 3D sample.

In MTS, an electron of charge -*e* tunnels along the *Z*-direction from an emitter (*E*) into the 0D state, separated by a distance *s*; under the effect of a transverse magnetic field applied along the *X*-direction, B_x, the electron acquires an additional in-plane momentum along the *Y*-direction, given by $\hbar\Delta k_y = -eB_x s$ (Figure 3.3). The tunnelling of electrons from the emitter into the 0D state is envisaged as a ballistic process (*i.e.* no scattering occurs). Thus the tunnel current, *I*, is determined by the matrix element, *M*, that governs the quantum transition of an electron tunnelling, *i.e.* $I \propto |M|^2$, where *M* is given by the overlap integral of the Fourier transforms, $\phi_E(k)$ and $\phi_{0D}(k)$ of the real-space wave functions of the emitter and of the 0D state, respectively[148]:

$$M = \int_k \phi_E(k - \Delta k_y)\phi_{0D}(k) \,. \tag{3.15}$$

For a 3D or 2D emitter, the emitter state has a much weaker spatial confinement in real space than the 0D state; conversely, $\phi_{0D}(k)$ is much more spread in *k*-space than $\phi_E(k - \Delta k_y)$ (Figure 3.3). The latter is a sharp function peaked at $k = \Delta k_y$. Thus, if $\phi_E(k - \Delta k_y)$ is approximated by a δ–function, the matrix element is $M(\Delta k_y) = \phi_{0D}(\Delta k_y)$. The additional momentum $\Delta k_y \propto B_x$ creates

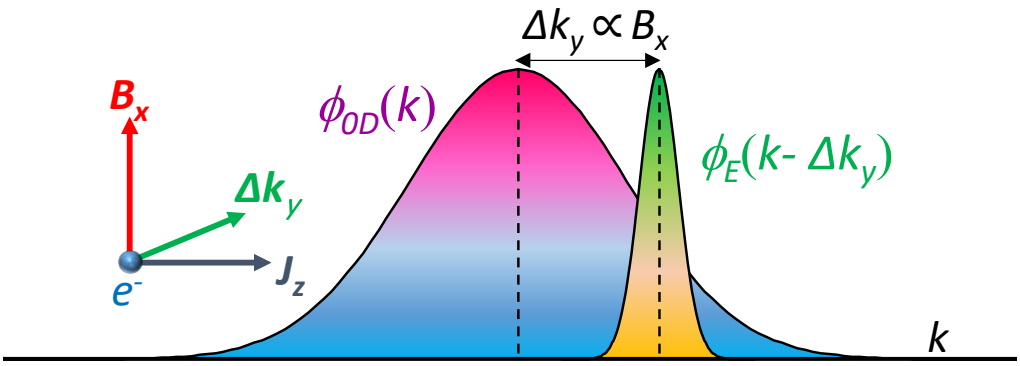


Figure 3.3: Sketch of the overlap in *k*-space of $\phi_{0D}(k)$ and $\phi_E(k-\Delta k_y)$, the Fourier transforms associated with the electron wave functions of the 0D state and the emitter, respectively. In our system, the electron current density *J* is along *z*, while the magnetic field *B* is applied along the *x*-direction, causing an additional momentum, Δk_y, along the *y*-direction, proportional to B_x.

a shift in the *k*-space between the two wave functions (as sketched in Figure 3.3). In this way, the B_x-induced variation of the tunnel current enables to probe the electron probability density in Fourier space of the resonant localized state[147]. Chapter 7 describes how this technique can be used to probe 0D states in the dilute nitride In(AsN) alloy.

3.1.3 Resonant tunnelling diodes (RTDs)

A resonant tunnelling diode (RTD) consists of a quantum well (QW) layer enclosed between two potential barriers. According to classical mechanics, the only particles that can pass a barrier of height V_0 are those with energy $E > V_0$. However, according to quantum mechanics, there is a finite probability for particles with $E < V_0$ to tunnel through the barrier. The tunnelling probability decreases exponentially with increasing barrier height and/or thickness[77].

The presence of two thin barriers in a RTD leads to the spatial confinement of electrons tunnelling in the QW for a finite period of time; the resulting quasi-bound state makes the RTD the electrical counterpart of an optical Fabry-Perot etalon: in both cases, wave-like particles are confined and partially reflected in a resonant cavity, enclosed by barriers in the RTD, by mirrors in the etalon. The constructive interference of the reflected waves in the cavity enables resonances.

To establish a flow of electrons tunnelling into the QW, the barrier structure is sandwiched between two highly doped semiconductor layers. These high conductivity regions effectively act as contacts and represent respectively a source and a sink for the electrons tunnelling into the RTD. Thus these are also referred to as *emitter* and *collector*, respectively.

The *tunnelling matrix* formalism enables the formal treatment of an electron tunnelling through a system of potential barriers by the calculation of the transmission coefficient, *T*, as a function of the energy, *E*, of the impinging electron. For an electron approaching a square potential barrier of height V_0 and thickness b , the transmission coefficient is given by [77]

$$\begin{cases} T(E) = \left[1 + \frac{{V_0}^2}{4E(E-V_0)} \sin^2(kb)\right]^{-1} & E > V_0 \\ T(E) = \left[1 + \frac{{V_0}^2}{4E(V_0-E)} \sinh^2(kb)\right]^{-1} & E < V_0 \end{cases} \tag{3.16}$$

where $k = \sqrt{|2m(E - V_0)|}/\hbar$. The plot of $T(E)$ for an InAs/(InAl)As/InAs barrier of height $V_0 = 0.12$ eV and thickness $b = 10$ nm is shown in Figure 3.4a, solid black line. Unlike the classical treatments (black dashed line), the probability of tunnelling for electrons with energy $E < V_0$ is non-zero, while the transmission coefficient is unity at energies $E > V_0$ when $kb = 2n\pi$, corresponding to the so-called over-the-barrier resonances (see zoom in the Inset of Figure 3.4a).

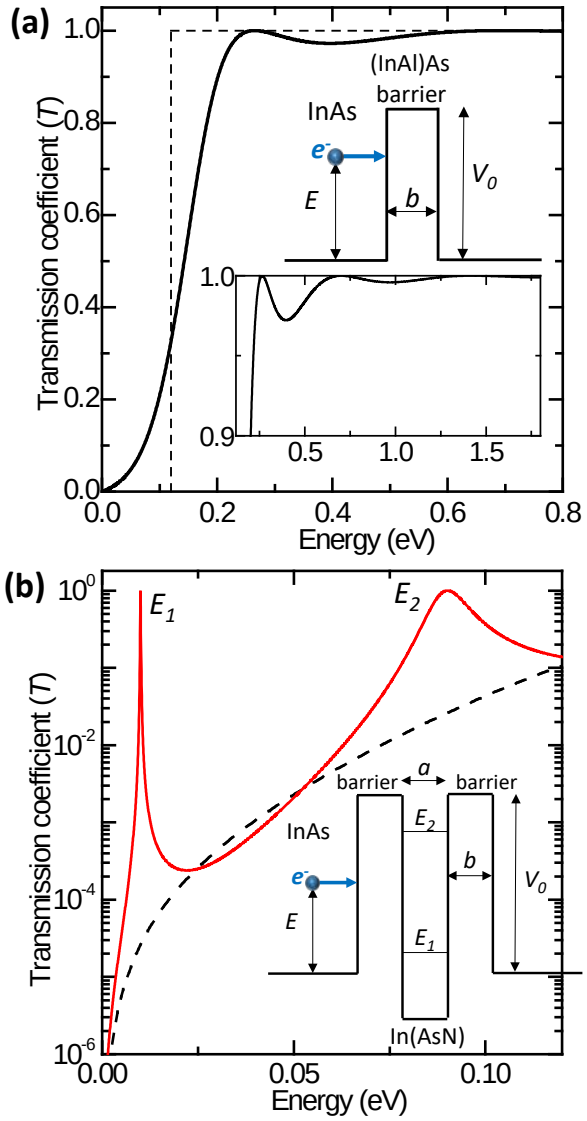


Figure 3.4: **(a)** Transmission coefficient, *T*, as a function of energy, *E*, for a square potential InAs/(InAl)As/InAs barrier of height V_0 = 0.12 eV and thickness *b* = 10 nm (sketch in the Inset). The dashed line represents the classical result for a barrier of the same height. Inset: zoom of *T*(*E*) on the over-the-barrier resonances. **(b)** Transmission coefficient, *T(E)*, for a resonant tunnelling structure (depicted in the Inset): an In(AsN) QW layer of thickness *a* = 10 nm is embedded in a double InAs/(InAl)As barrier of thickness *b* = 10 nm. The dashed curve shows the transmission for an In(AlAs) barrier of thickness 2*b*; this result would apply to the double barrier if there was no resonance.

Let us consider now an RTD consisting of a double (InAl)As barrier of thickness b = 10 nm embedding an In(AsN) QW layer of thickness a = 10 nm (Inset of Figure 3.4b). The presence of quantized electronic levels in the QW (of energies E_1 and E_2) due to spatial confinement has dramatic consequences for the electron transmission. The calculation of the electronic bound states in a QW is treated in Appendix A. The tunnelling probability out of resonance (black dashed line in Figure 3.4b) is the product of the tunnelling probabilities of the left and right barriers, denoted as T_L and T_R , respectively. However, whenever the impinging electron is close to resonance with the QW bound state, the tunnelling probability increases significantly (Figure 3.4b). In this case the tunnelling probability profile has a Lorentzian shape centred on E_1 [77]

$$T(E) = T(E_1)\left[1 + \left(\frac{E-E_1}{\Gamma/2}\right)^2\right]^{-1}, \tag{3.17}$$

where $\Gamma = \hbar v\,(T_L + T_R)/2a$ is the width of the Lorentzian profile for an electron with velocity v. The peak transmission $T(E_1)$ is given by:

$$T(E_1) \sim \frac{4T_L T_R}{(T_L+T_R)^2}\ . \tag{3.18}$$

Note that for symmetric barriers ($T_L \sim T_R$) the transmission peak approaches unity. This dramatic enhancement of the tunnelling probability on resonance has profound consequences for the tunnel current in barrier-based devices such as RTDs.

Figure 3.5a shows the CB profile for an RTD structure under different bias regimes, along with the corresponding current-voltage, *I-V*, characteristic (Figure 3.5b). The shaded regions represent the 3D emitter (*E*) and collector (*C*), with Fermi energy E_F^E and E_F^C, respectively. The QW bound state has energy E_0, as measured from the CB minimum.

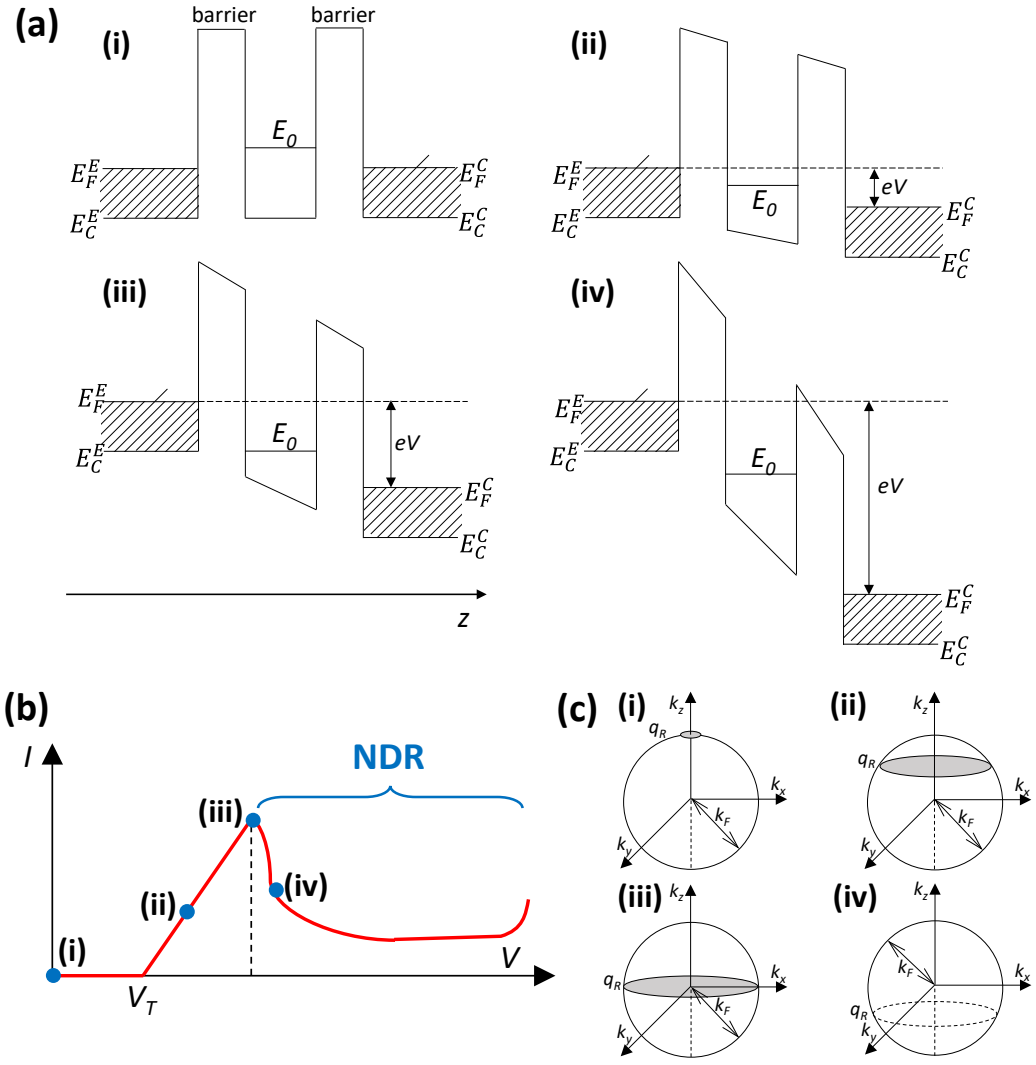


Figure 3.5: **(a)** Conduction band profile for a RTD for zero applied bias (i), on resonance (ii), at the current peak (iii), and off resonance (iv). **(b)** Sketch of the corresponding *I-V* characteristic. **(c)** Sketch depicting the intersection of the plane $k_z = q_R$ with the Fermi sphere in the different bias regimes (i-iv).

Under zero applied bias, no electrons can tunnel through the barrier, thus resulting in zero current (i). A bias $V \neq 0$ applied across the device creates a potential difference and changes the relative position between the energy levels in the QW and the emitter. The resonant transmission of electrons across the device occurs when the QW state at energy E_0 is aligned with the Fermi energy

of the emitter, E_F^E; the bias at which this occurs is called threshold bias, V_T, (Figure 3.5b), and a current starts flowing for $V > V_T$. Let $k_F \propto (E_F^E)^{1/2}$ be the Fermi momentum, *i.e.* the radius of the Fermi sphere for the 3D emitter, and let $q_R \propto (E_0)^{1/2}$ be the wavenumber associated with the energy of the resonant state: for every bias, the electronic states involved in the tunnelling are those fulfilling the conservation of energy and momentum, *i.e.* those states in the *k*-space represented by the intersection of the Fermi sphere with the plane $k_z = q_R$. The current density *J* is thus proportional to the area of the intersection (grey disk in Figure 3.5c):

$$J \propto \pi(k_F^2 - q_R^2) \propto (E_F^E - E_0) \propto eV \ . \qquad (3.19)$$

Since $(E_F^E - E_0)$ is proportional to the applied bias *V*, the tunnel current *I* increases linearly with the applied bias *V* as long as the QW state is resonant with the 3D emitter (ii). The tunnel current increases from zero when $k_z = k_F$ and has a maximum when $k_z = 0$ (iii). A further increase of the applied bias brings the system off resonance: no electron fulfils the energy and momentum conservation requirement, leading to a drop in tunnel current with increasing voltage, also known as negative differential resistance (NDR) region (iv). At even higher *V*, the total *I* is the result of contribution from thermal current and excess current, and it presents an exponential increase with the applied bias[132].

3.2 Plasmonics

The excitation of an electron gas is called a plasma oscillation, namely a longitudinal collective charge density oscillation, whose quantum is called a *plasmon*[149]. Let us consider the so-called plasma model, consisting of a thin metallic film with a gas of electrons of charge –*e* and average density n_e

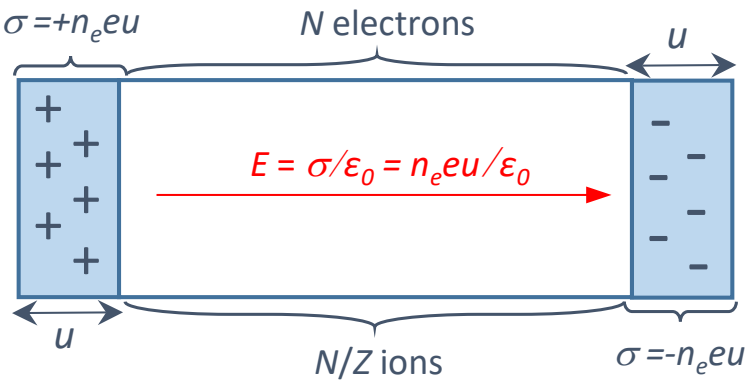


Figure 3.6: Model of a plasma oscillation: a displacement $\vec{u}$ of the electron gas with respect to the positive background charges gives rise to a surface charge density, σ, which in turn induces an electric field $\vec{E} = n_e e\vec{u}/\varepsilon_0$.

embedded in a uniform and fixed background of neutralizing positive charges. The electron gas moves as a whole with respect to the positive background ion charges. A displacement, $\vec{u}$, of the electron gas creates an electric field $\vec{E} = n_e e\vec{u}/\varepsilon_0$, where ε_0 is the vacuum permittivity (Figure 3.6). From the equation of motion

$$m\frac{d^2\vec{u}}{dt^2} = -e\vec{E} = -\frac{n_e e^2\vec{u}}{\varepsilon_0} \tag{3.20}$$

one can see that the system oscillates at the so-called plasma frequency (ω_p),

$$\omega_p = \sqrt{\frac{n_e e^2}{m_0 \varepsilon_0}}, \tag{3.21}$$

where m_0 is the electron mass in vacuum. In a semiconductor material, the modification of the electron motion from the energy band structure is accounted for by the electron effective mass m_e^*. In such a system, with relative permittivity ε_r , the plasma frequency becomes:

$$\omega_p = \sqrt{\frac{n_e e^2}{m_e^* \varepsilon_0 \varepsilon_r}}. \tag{3.22}$$

The plasma model accounts for several optical properties of metals over a wide range of frequencies (visible-UV)[149]. Within this model, the free electrons oscillate in response to the applied electromagnetic field and they collide with a characteristic collision frequency, $g = 1/\tau$, where τ is the relaxation time of the free electron gas. One can then write the following equation of motion:

$$m\frac{d^2\vec{u}}{dt^2} + mg\frac{d\vec{u}}{dt} = -e\vec{E} \ . \tag{3.23}$$

By assuming that the time dependence of the driving electromagnetic field is harmonic, *i.e.* $E(t) = E_0 e^{-i\omega t}$, a particular solution for the electron oscillation is given by $\vec{u}(t) = \vec{u}_0 e^{-i\omega t}$, where the terms $\vec{u}_0$ incorporates any phase shift between the driving field in and the response. Thus the solution of Equation 3.23 is given by

$$\vec{u}(t) = \frac{e}{m(\omega^2 + ig\omega)}\vec{E} \ . \tag{3.24}$$

The free electron displacement contributes to the macroscopic polarization, $\vec{P}$:

$$\vec{P} = -n_e e\vec{u}(t) = -\frac{n_e e^2}{m(\omega^2 + ig\omega)}\vec{E} \ . \tag{3.25}$$

From the expression for the dielectric displacement, $\vec{D} = \varepsilon_0\vec{E} + \vec{P} = \varepsilon(\omega)\vec{E}$, one can derive the frequency-dependent dielectric function:

$$\varepsilon(\omega) = 1 - \frac{\omega_p^2}{\omega^2 + ig\omega} \ . \tag{3.26}$$

In several cases, the residual polarization from the positive background ions should be accounted for by considering the high-frequency dielectric constant, ε_∞:

$$\varepsilon(\omega) = \varepsilon_\infty - \frac{\omega_p^2}{\omega^2 + ig\omega} \ . \tag{3.27}$$

Given the ability of an electron gas in metals to couple with impinging radiation at metallic interfaces, plasmonics is of particular relevance for those

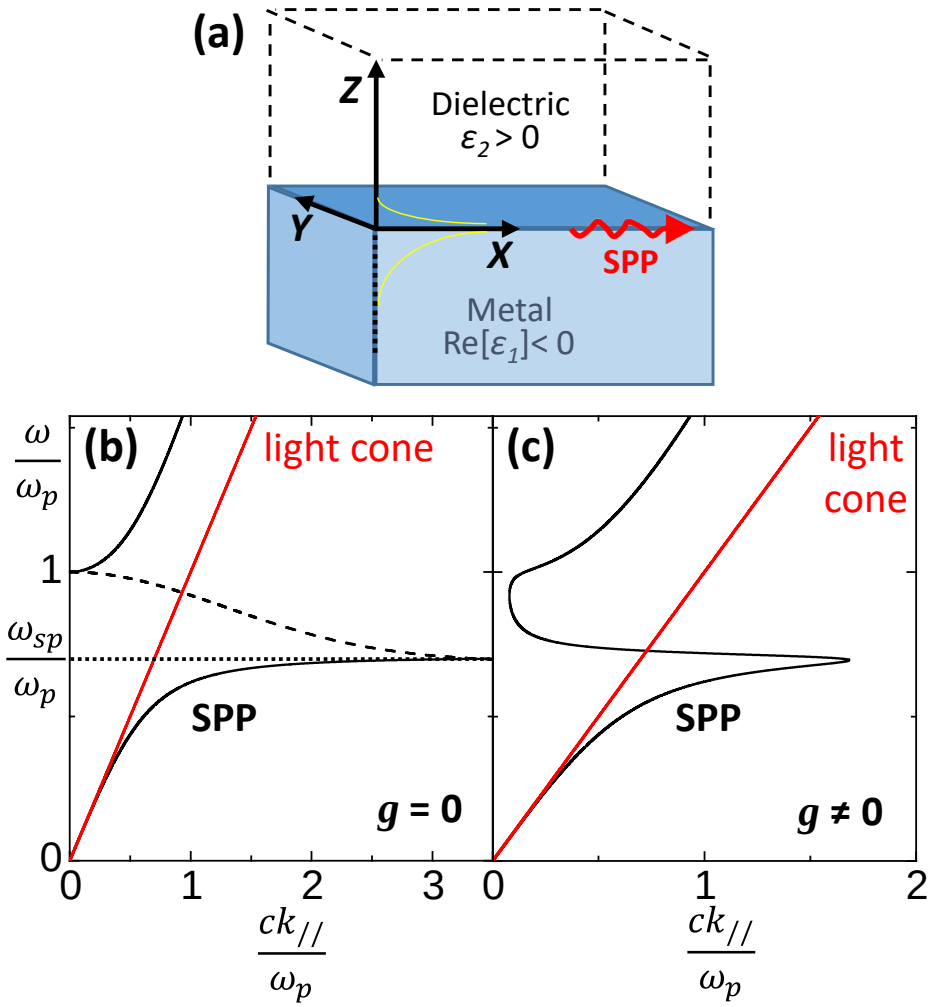


Figure 3.7: **(a)** Geometry for SPP propagation at the interface between a metal ($Z < 0$) and a dielectric ($Z > 0$). **(b-c)** Dispersion relation of SPPs at the interface between air and a metal with negligible (b) and finite (c) plasma broadening, g.

fields in physics and technology where surface effects are concerned, such as detection of molecular and gas species. This implies that one looks for propagating wave solutions that are confined to the interface. A simple geometry is the one depicted in Figure 3.7a: we take X as the direction of propagation of the wave and ignore the variation along the transverse in plane Y-direction. The dielectric constant only changes along the Z-direction, *i.e.* $\varepsilon = \varepsilon(Z)$: the system consists of a single interface between a dielectric medium (2) with real dielectric

constant $\varepsilon_2 > 0$ ($Z > 0$ in Figure 3.7a) adjacent to a conducting medium (1) with dielectric constant $\varepsilon_1(\omega) = \varepsilon_{1\infty} - \frac{\omega_p^2}{\omega^2 + ig\omega}$ ($Z < 0$ in Figure 3.7a), where ε_∞ is the background dielectric constant limit for $\omega \to \infty$ and g is the plasma broadening. Note that $Re(\varepsilon_1) < 0$ is implied by the metallic behaviour of the medium (1).

By solving Helmholtz equation for the electric field and by imposing the requirement of solutions with evanescent decay along the Z-direction perpendicular to the interface, the only surface modes allowed are those with transverse magnetic (TM) polarization, *i.e.* those allowing E_x and E_z as the only nonzero electric field components, and thus H_y as the only nonzero magnetic field component. By further imposing that H_y fulfil the wave equation and the continuity of H_y and εE_z at the interface, we obtain the dispersion relation of the so-called *surface plasmon polariton* (SPP) mode propagating at the interface between the two media[149]

$$\omega = ck_{//}\sqrt{\frac{[\varepsilon_1(\omega)+\varepsilon_2]}{\varepsilon_1(\omega)\varepsilon_2}}\ , \tag{3.28}$$

where c is the speed of light in vacuum and $k_{//}$ is the component of the wavevector k parallel to the interface. The typical dispersion curve of SPP is depicted in Figures 3.7b-c; here we normalize the SPP frequency and wavevector to the plasma frequency, ω_p. For a metal with negligible plasma damping ($g = 0$) (Figure 3.7b), the radiative regime corresponds to the branch at $\omega > \omega_p$; on the other hand, given their bound nature, the SPP excitations are those lying to the right of the light cone. In the limit of large wavevector ($k_{//} \to \infty$), the SPP dispersion approaches the so-called surface plasmon frequency

$$\omega_{sp} = \omega_p \sqrt{\frac{\varepsilon_2}{\varepsilon_1(\omega)+\varepsilon_2}} < \omega_p \,, \tag{3.29}$$

which is thus red-shifted compared to the plasma frequency. Between the radiative and bound regime, a frequency gap is created for frequencies $\omega_{sp} < \omega < \omega_p$ (dashed line in Figure 3.7b). Assuming finite plasma broadening ($g \neq 0$) due to free-electron and interband damping (Figure 3.7c), the metal dielectric function $\varepsilon_1(\omega)$ is complex, and thus also the SPP propagation constant $k_{//}$. The SPP dispersion is now broadened, approaching ω_{sp} at a finite wavevector and allowing quasibound leaky dispersion between frequencies ω_{sp} and ω_p[149].

3.2.1 Plasmonics in highly doped semiconductors (HDSCs)

Plasmonics generally relies on metals due to the high density of free electrons. However, metals also suffer from substantial losses due to interband transitions, grain-boundary scattering in thin films, surface roughness, *etc*.; chemical instability in air and low compatibility with silicon technology represent further limitations to the exploitation of metals[150]. In general, metals have plasma frequencies, ω_p, in the visible-UV spectral ranges of the electromagnetic spectrum due to their high carrier densities (10^{22} - 10^{23} cm^{-3}). On the other hand, highly doped semiconductors (HDSCs) represent interesting alternative candidates for plasmonics due to several appealing features[151, 152]: firstly, the lower carrier densities (10^{16} - 10^{20} cm^{-3}) enable plasma frequencies in the mid-infrared (MIR) spectral range, of relevance for technologically important applications, including gas detection and biosensing[153, 154]; secondly, the carrier density and the plasmonic resonance can be tuned either by doping or geometrical patterning of semiconductors[155], thus enabling routes to cost-effective and compact all-semiconductor plasmonic structures[49, 134].

Achieving a high doping in a semiconductor can be limited by the solid solubility of the dopants[6, 68] and/or by doping compensation effects[69, 70]. In addition, a high density of dopants can degrade the crystal quality and induce internal losses. Thus finding low-loss semiconductor materials for plasmonics presents challenges of fundamental and technological interest[156]. Figure 3.8 shows an overview of the performance of different material classes as low loss materials for plasmonic application. These materials range from metals to semi-metals and semiconductors, and they are compared in terms of interband losses, carrier concentrations and mobilities[156].

To date, a number of HDSCs have been successfully tested, including transparent conducting oxides (TCOs), such as aluminium and gallium zinc oxide[157], indium tin oxide[158], and dysprosium cadmium oxide[159]. These materials have plasmonic resonances in the near-infrared (NIR)[14, 15] and MIR spectral range[16]. Compounds such as SiC[160], (InGa)As[161], and In(AsSb)[49, 155, 162] have also shown good response in the MIR[163]. Within this context, the III-V InAs compound features as a relatively recent addition to this group: it can sustain high doping concentrations[68, 164] with plasmonic resonances over a broad MIR range[165].

In this thesis, we demonstrate a novel approach to exploit InAs as a HDSC for plasmonics in the MIR. As presented in Section 2.2.1, the *post-growth* incorporation of hydrogen (H) atoms in the dilute nitride In(AsN) alloy induces an increase of the electron density, n_e, by two orders of magnitude, up to 10^{19} cm^{-3} [31, 32]. This behaviour, not observed among other III-Vs, makes the highly H-doped In(AsN) alloy a promising candidate for plasmonic applications. In this work (Chapter 5) we demonstrate that In(AsN):H can support MIR surface

plasmon polaritons and that the plasmonic resonance can be spatially tailored and suppressed by photo-annealing[166].

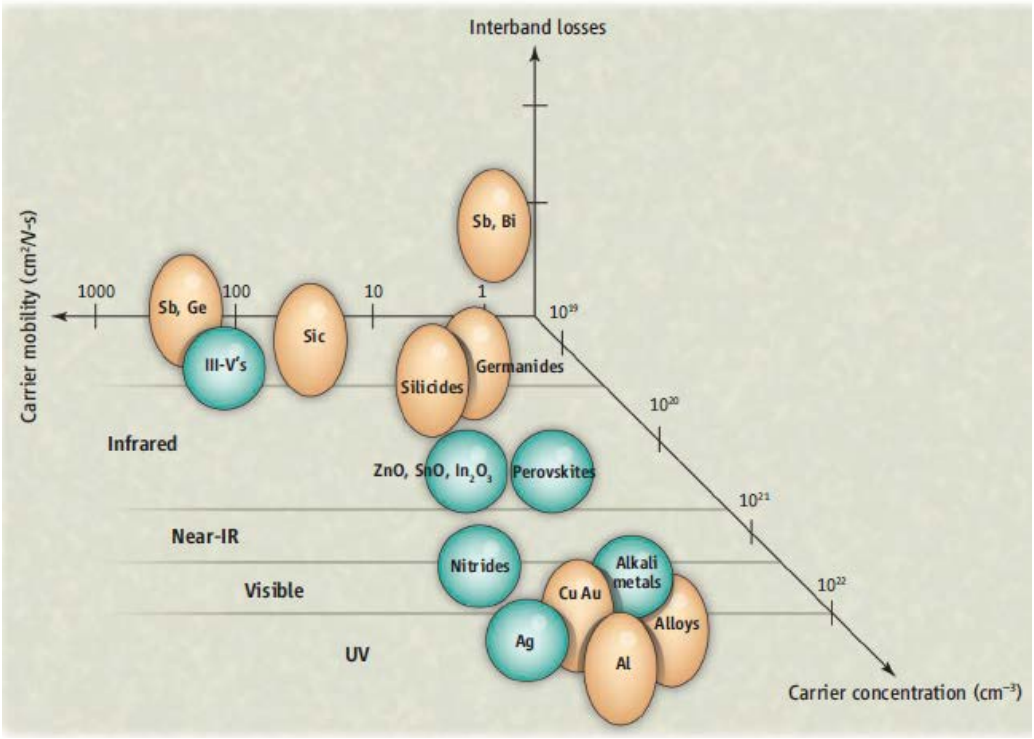


Figure 3.8: A comparison of the performance of different materials as low-loss plasmonic materials in terms of interband losses, carrier concentrations and mobilities[156].

Chapter 4

Samples and experimental techniques

This chapter describes the samples and the experimental techniques used to obtain the results presented in this thesis. Our samples consist of MBE-grown In(AsN) epilayers (4.1.1) and In(AsN)/(InAl)As resonant tunnelling diodes (RTDs) (4.1.2). These were studied and characterized using a range of transport (4.2) and optical (4.3) techniques. The experimental setup used for the topographical studies is also presented in Section 4.4.

4.1 Samples

4.1.1 In(AsN) epilayers and hydrogenation

We used In(AsN) epilayers with thickness t = 0.3 μm (nitrogen content [N] = 1%) and t = 1 μm ([N] = 1.1%). The In(AsN) epilayers were grown by Dr. M. Kesaria and Prof. A. Krier (Lancaster University) using a VG-V80H solid-source molecular-beam-epitaxy (MBE) reactor with a Vecco UNI-bulb radio-frequency (RF) plasma nitrogen-source. In and Ga fluxes were provided by Knudsen thermal-effusion cells. The In(AsN) epilayers were grown at T = 450 °C using an RF power of 200 W and a nitrogen background pressure of 5×10^{-6} mbar. The layers were grown on 250 nm-thick GaAs buffers on semi-insulating (100)-oriented 500 nm-thick GaAs substrate (Figure 4.1a). There is a large lattice mismatch between the In(AsN) epilayer and the GaAs substrate

($\Delta a/a_{InAs}$ ~ 6.6 %), leading to the formation of dislocations at the In(AsN)/GaAs interface[167]. The In(AsN) epilayer has a thickness t = 0.3 - 1 μm and its crystal lattice is not lattice-matched to the GaAs substrate. *In situ* characterization of the grown material was performed by reflection high energy electron diffraction (RHEED).

The as-grown In(AsN) epilayers were hydrogenated using a Kaufman source by Prof. M. Capizzi (Sapienza Universitá di Roma). The schematic diagram of the hydrogenated epilayers and of the experimental setup used for the hydrogenation are shown in Figures 4.1a and 4.2, respectively. Molecular hydrogen (H_2) is pumped into the ionization chamber, where it is dissociated into neutral H-atoms and protons by the electrons emitted from a hot tungsten filament (cathode) and accelerated towards the walls of the chamber (anode). A set of magnets is used to spiral the trajectories of the electrons, thus enhancing the cross-section for the hydrogen dissociation. In order to minimize the sample damage, the beam of hydrogen ions (H^+) is accelerated at low energy by a set of negatively polarized grids held at high voltage. The ion beam then enters the main chamber and impinges on the sample, which is electrically grounded, with

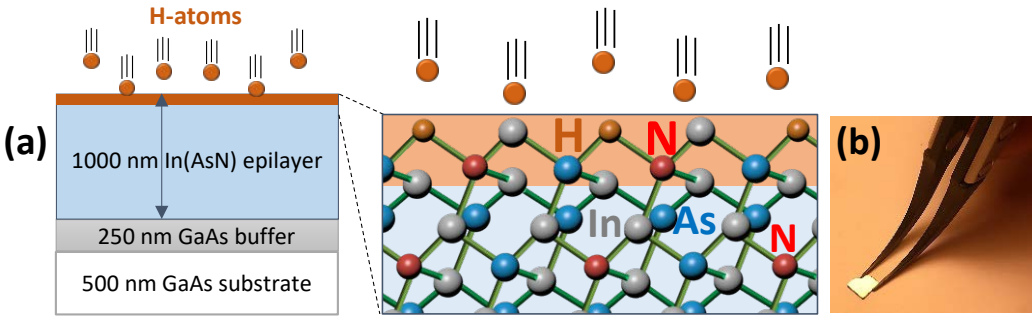


Figure 4.1: **(a)** Schematic diagram of the layer structure of the In(AsN) epilayers. The zoom depicts the creation of a thin conductive channel of In(AsN):H following the hydrogenation of the epilayer. **(b)** A typical In(AsN) wafer studied before and after hydrogenation.

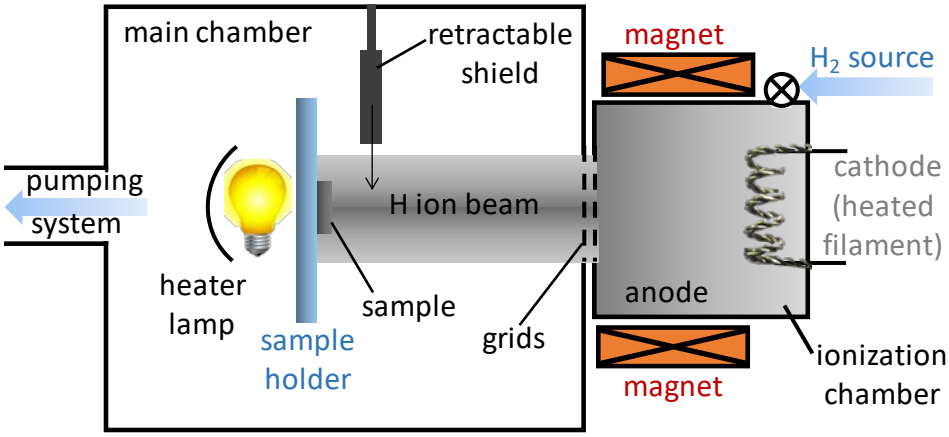


Figure 4.2: Sketch of the experimental setup used for the hydrogenation.

a Gaussian profile (standard deviation, $\sigma \sim 2.5$ cm). Note that σ is much larger than the usual size of the wafers (~ mm) used; thus the hydrogenation process can be regarded as uniform across the sample area.

Since the penetration depth of low-energy protons is only of the order of ~ 1 nm, a sizable in-depth diffusion of the H ions in the sample is achieved by maintaining the sample and the sample holder at a constant temperature (T_H ~300-400 °C) by controlling the voltage of two quartz-iodine projection lamps (650 W each). The H-beam dose (D_H) is determined by monitoring the H-dose rate with a Faraday cup located in front of the sample at the beginning (and checked again at the end) of the hydrogenation process as well as by the hydrogenation duration. Finally, a pressure of ~ 5×10^{-7} mbar is achieved in the main chamber by using a turbo-molecular pump before opening the H-flux, while a vacuum of 2×10^{-3} mbar is maintained during the H-irradiation of the sample. Under the hydrogenation conditions used for our samples (ion beam energy E = 100 eV, $D_H = 3\times10^{17}$ ions/cm^2 at T_H = 375°C for 2 hours), a highly conductive channel of thickness ~ 0.1 μm is created below the surface of the epilayer upon the incorporation of H-atoms, as depicted in Figure 4.1a.

4.1.2 In(AsN)/(InAl)As *p-i-n* resonant tunnelling diodes

For these studies, we designed and grew by molecular-beam epitaxy (MBE) a series of In(AsN) resonant runnelling diodes (RTDs), whose layer structure is depicted in Figure 4.3a. The RTD is a multilayer structure consisting of a 10 nm In(AsN) quantum well (QW) ([N] = 1%) embedded between two 10 nm (InAl)As tunnel barriers ([Al] = 10%). Undoped InAs spacer layers of width 20 nm separate the (InAl)As barriers from 10^{17} cm^{-3} *n*- and *p*-doped InAs layers of width 300 nm on each side of the barriers. The above layers were sandwiched between 10^{18} cm^{-3} *n*- and *p*-doped InAs layers of width 100 nm, which formed *p*- or *n*- low resistance electrical contacts. The structure was grown on an n^+-type InAs substrate at T = 500 °C except for the In(AsN) layer, which was grown at T = 380 °C. For comparison, a control sample was also grown with the same sequence of layers as that described above, except that it contains no nitrogen

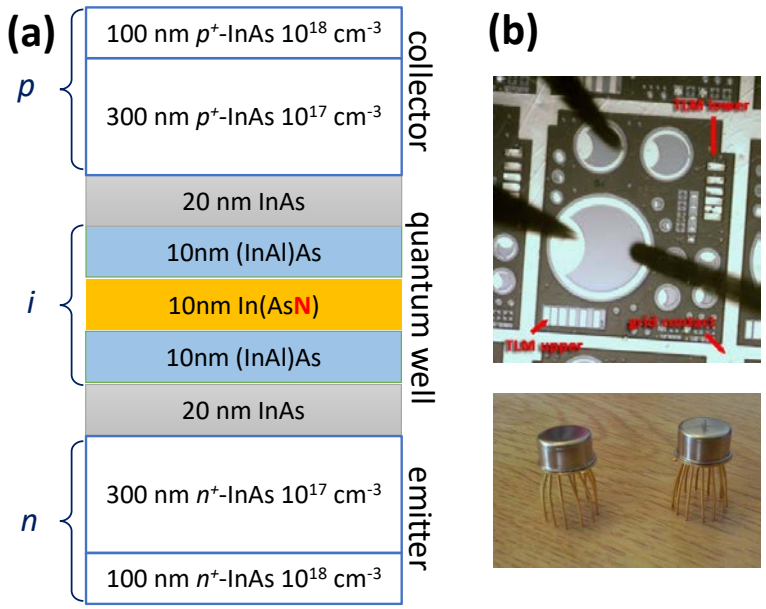


Figure 4.3: **(a)** Schematic diagram of the layer structure of the In(AsN)/(InAl)As *p-i-n* RTDs. **(b)** The samples were processed into optical mesa diodes (top) mounted onto T05 headers (bottom)

and the InAs QW layer is grown at 460 °C. The samples were processed into circular mesa diodes of diameter d = 100, 200 and 400 μm, with Au/Ti ohmic contacts alloyed to the top and bottom doped InAs layers and mounted onto 12-pin T05 headers to perform electrical characterization (Figure 4.3b).

4.2 Experimental techniques: transport studies

4.2.1 Current-voltage (*I-V*) measurements

To acquire the *I-V* characteristic of the *p-i-n* RTDs, the devices were processed into mesa diodes and mounted onto T05 headers, as discussed in Section 4.1.2. Figure 4.4 shows a sketch of the experimental setup used to acquire the low-temperature (4.2 K) *I-V* characteristics of the RTDs. The device was mounted onto a sample probe whose end dips directly into liquid helium to

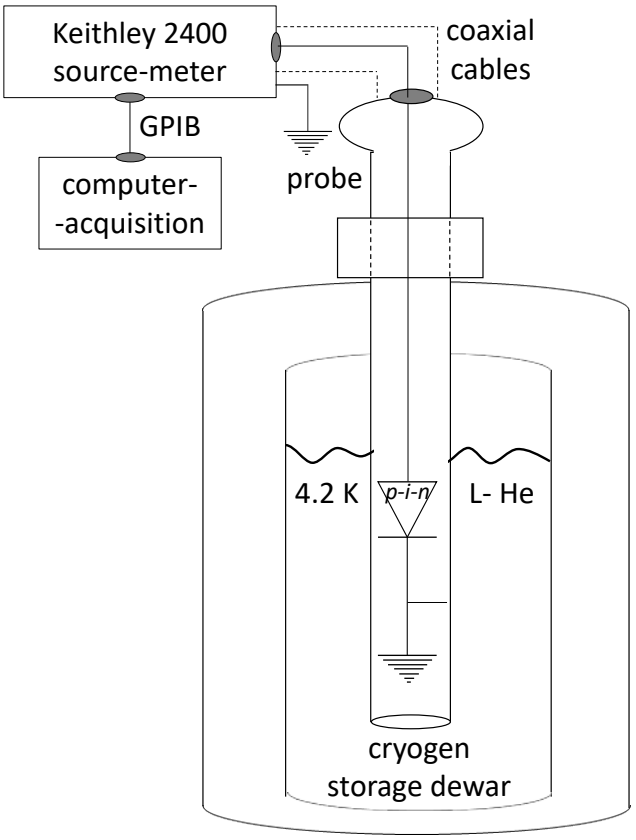


Figure 4.4: Sketch of the experimental setup used to acquire the low-temperature (4.2 K) *I-V* characteristic of the *p-i-n* RTDs.

enable transport measurements at T = 4.2 K. The liquid helium dewar is connected to the ground electrode (Figure 4.4), providing electrical screening to reduce the noise. A Keithley 2400 DC source meter was used as a voltage source and current meter for the RTD. The acquisition of data from the source meter was realized using a programme written with LabView and GPIB interface.

The transport studies on our RTDs were also performed at different temperatures (up to 300K) by using the experimental setup sketched in Figure 4.5. The sample probe is inserted into a cryostat consisting of two insulated environments. The outer shell is kept under vacuum (~10^{-6} mbar) by a turbo pump to enable insulation from the external environment. The inner shell is the sample space and is directly connected to a cryogen storage dewar filled with liquid helium. The helium circulation in the sample space is achieved by using a membrane pump; a flow-meter enables to monitor the flow of helium into the system. The temperature of the sample in the sample space is controlled by a heater connected to the system and by adjusting the helium flow. The sample probe is connected to a Keithley 2400 DC source meter to measure the *I-V* characteristic of the RTDs.

4.2.2 Low-temperature magneto-tunnelling spectroscopy

A magneto-cryostat supplied by Cryogenic Ltd was used to carry out low temperature transport measurements under a magnetic field (see sketch in Figure 4.6a): the cryostat is enclosed by a stained steel outer shell. It contains an outer vacuum chamber (OVC) kept at a temperature T = 77 K by liquid nitrogen (L-N_2) that is inserted via cold traps to limit the liquid helium consumption. The main bath is filled with liquid helium (L-He) at T = 4.2 K. The cryostat core contains a superconducting magnet consisting of two coils, an inner section

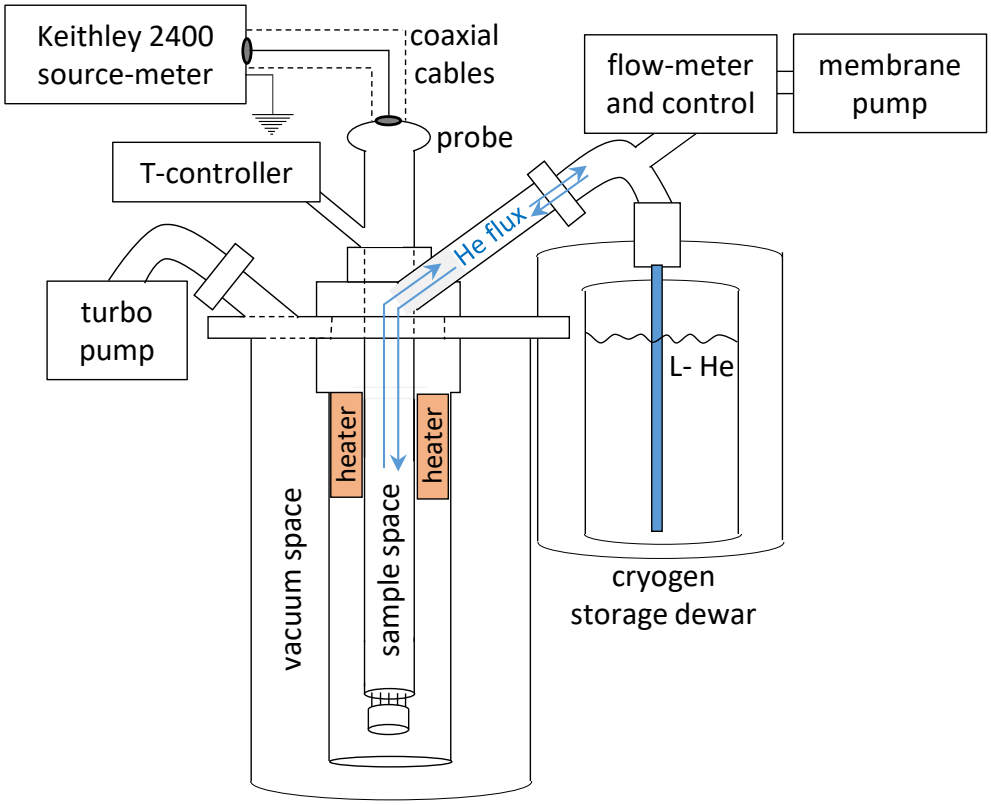


Figure 4.5: Sketch of the experimental setup used to acquire the *I-V* characteristic of the *p-i-n* RTDs at 10 K < *T* < 300 K.

wound from a niobium-tin (Nb_3Sn) wire and an outer section consisting of a niobium-titanium (NbTi) wire. An inner vacuum chamber (IVC) enables isolation from the external environment by an airlock and the insertion of the sample via a probe. The airlock allows to warm up the sample at the He-atmosphere, to prevent condensation. Vacuum insulation enables to cool the sample space down to T = 2 K. A variable temperature inset (VTI) enables to control the temperature of the sample space with a heater (not shown) in the range T = 2 - 250 K.

At T = 4.2 K, the coils are superconducting and support currents up to 100 A, thus enabling to achieve magnetic fields, B, up to 14 T. The sample probe reaches the centre of the magnets, thus minimizing the fluctuations of the

magnetic field lines. For our experiments, we used a probe whose end can be rotated by an arbitrary angle, θ, with respect to the applied magnetic field (see sketch in Figure 4.6b). As extreme cases, the flow of the current, I, through the device can be set both parallel ($\theta = 0°$ or $B = B_{//}$) or perpendicular ($\theta = 90°$ or $B = B_{\perp}$) to the magnetic field.

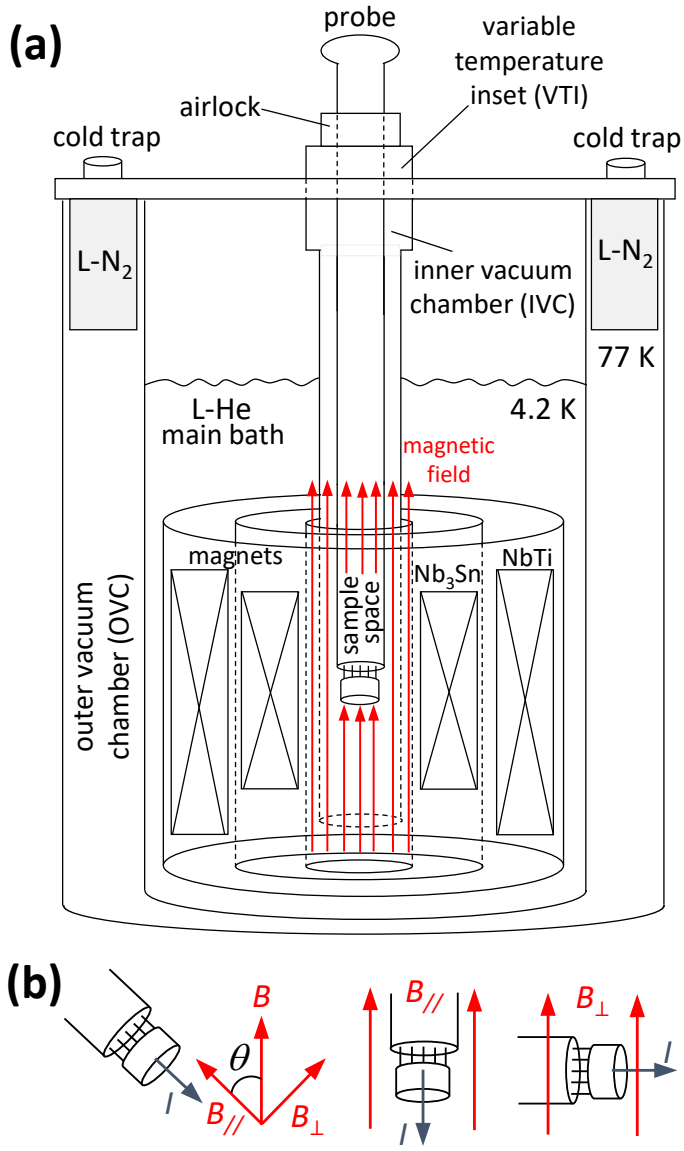


Figure 4.6: **(a)** Sketch of the cryostat used for MTS studies. **(b)** Sketch of the different magnetic field geometries, with the magnetic field applied parallel (//), perpendicular (⊥) or tilted relative to the current flow, I, in the device.

4.3 Experimental techniques: optical studies

4.3.1 Raman spectroscopy

The Raman spectroscopy measurements were carried out using a LabRAM HR-UV spectrometer equipped with a confocal microscope that provides high wavelength resolution down to $\Delta\lambda = 10^{-2}$ nm. The system, whose schematic diagram is reported in Figure 4.7, comprises of the following main components:

- *Optical microscope*: this component is used for imaging and has 3 objectives providing 10×, 50× and 100× magnification. The objectives have focal length f = 18, 3.6, 1.8 mm and numerical aperture NA = 0.25, 0.55, 0.8, respectively.
- *Spectrometer*: the Raman signal is dispersed by a grating (1200 g/mm) and detected by a Si-charged coupled device (CCD) array photodiode, which covers the UV-visible wavelength range λ = 350-800 nm.
- *Optics*: this comprises of mirrors, a beam splitter and filters, used to direct the laser beam from the laser source (He-Ne at λ = 633 nm or a frequency

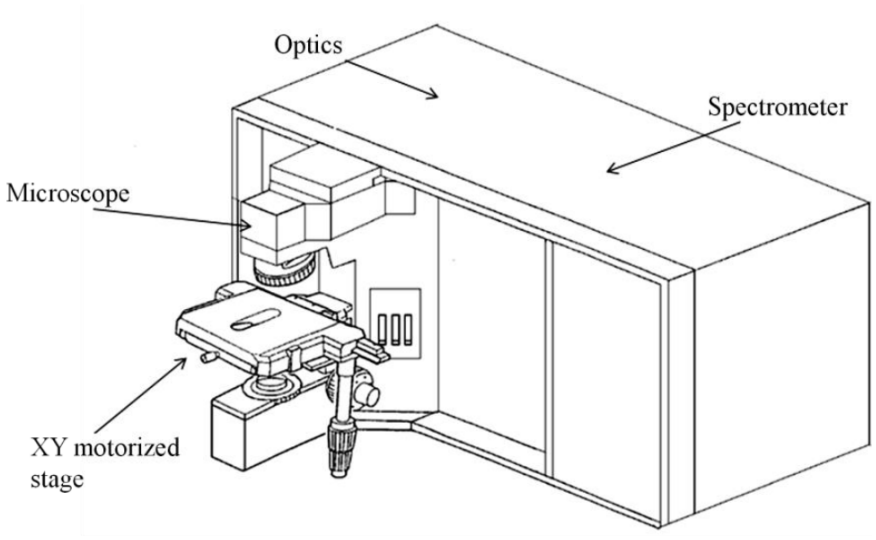


Figure 4.7: Schematic diagram of the LabRAM HR-UV spectrometer[168].

doubled Nd:YVO_4 laser at λ = 532 nm) to the sample and to collect the light from the sample to the detectors.

- *XY/Z motorized stage*: this component can be moved with a spatial resolution of 0.1 μm along the *X*, *Y* and *Z* directions. This component also enables the spatial mapping of the Raman signal coming from the sample by moving the stage point by point with respect to the laser beam.

The schematic diagram of a confocal microscope is shown in Figure 4.8. The laser beam is focused by an objective to a nearly diffraction-limited spot on the sample surface. The photo-excited light from the sample is collected by the same objective and sent to a detector with an adjustable pinhole aperture. In this

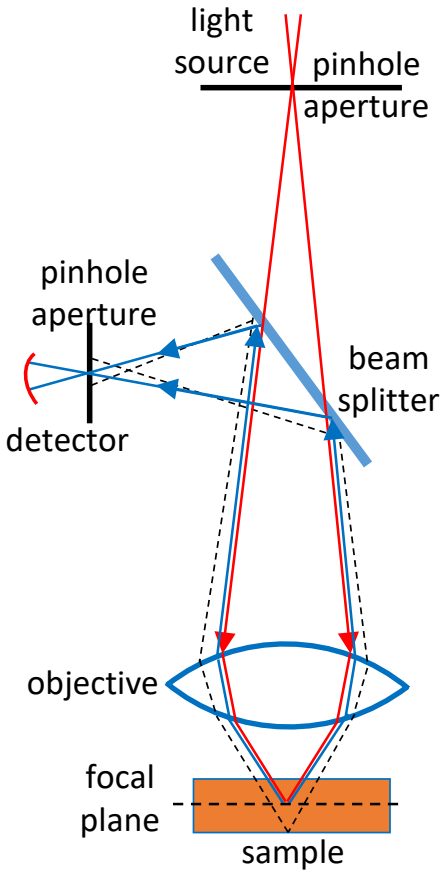


Figure 4.8: Schematic diagram of a confocal microscope, showing the light source, the pinhole apertures, the beam splitter, the objective, the sample and the detector.

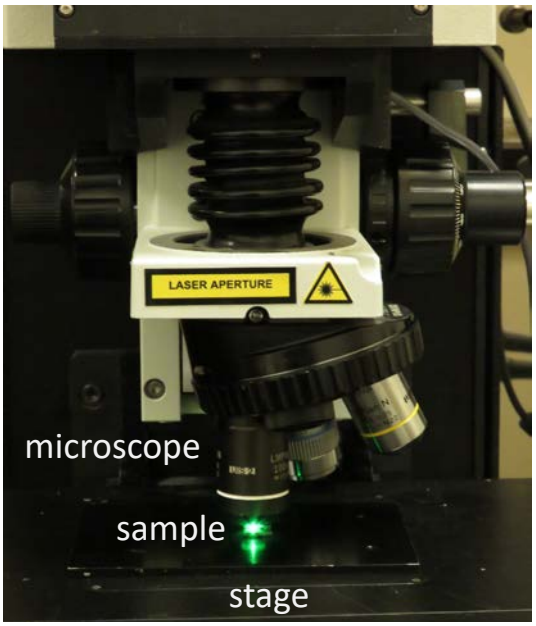


Figure 4.9 Experimental setup for Raman spectroscopy measurements, showing the microscope, the motorized stage, the sample and the focused laser beam.

way, only the light emitted from the spot can pass through the pinhole, which acts to block the light from outside the spot or off the focal plane.

The experimental setup for Raman spectroscopy measurements is shown in Figure 4.9. The laser beam is focused onto the sample by the 100× objective. Using the Rayleigh criterion, the diameter of the spot is given by $d_R = 1.22 \times \lambda / NA$, where $NA = (n \sin\theta)$ is the numerical aperture of the objective, n is the refractive index of the medium between the lens and the focal plane, and θ is the half angle between the marginal converging rays of the light cone. For NA = 0.9, the beam diameter is d_R = 0.86 μm for λ = 633 nm, and d_R = 0.72 μm for λ = 532 nm. This values give the spatial resolution of the confocal microscope. This can be limited by the size of the pinhole. The pinhole aperture should be small enough to ensure high spatial resolution but at the same time large enough to enable sufficient light to be directed into the detector.

4.3.2 Reflectance spectroscopy

The reflectance spectroscopy studies were carried out by myself at the Université de Montpellier. The experimental setup is shown in Figure 4.10. It consists of a Globar light source, a polarizer, a KBr beam splitter, and a Hyperion 3000 microscope coupled to a Vertex 70 FTIR Fourier Transform Infrared (FTIR) spectrometer. The reflectance spectra were acquired in two different configurations.

In the Brewster configuration (Figure 4.11) the *p*-polarized light is incident at an angle θ_i = 60° to the normal to the surface of the sample, and the reflected beam is detected by a deuterated triglycine sulfate (DTGS) detector.

In the attenuated total reflection (ATR) configuration (Figure 4.12) a 20× objective is used to focus the light beam through a Ge prism to a diameter d ~ 100 µm; light impinges on the sample at angles of incidence, θ_i , ranging from 9.8° to 23.6°. The light undergoes total internal reflection at the interface of Ge (refractive index n_{Ge} = 4) with air (n_{air} = 1) for angles θ_i higher than the critical angle, $\theta_c = \sin^{-1}(n_{air}/n_{Ge})$ ~ 14.5°, thus generating evanescent waves. In

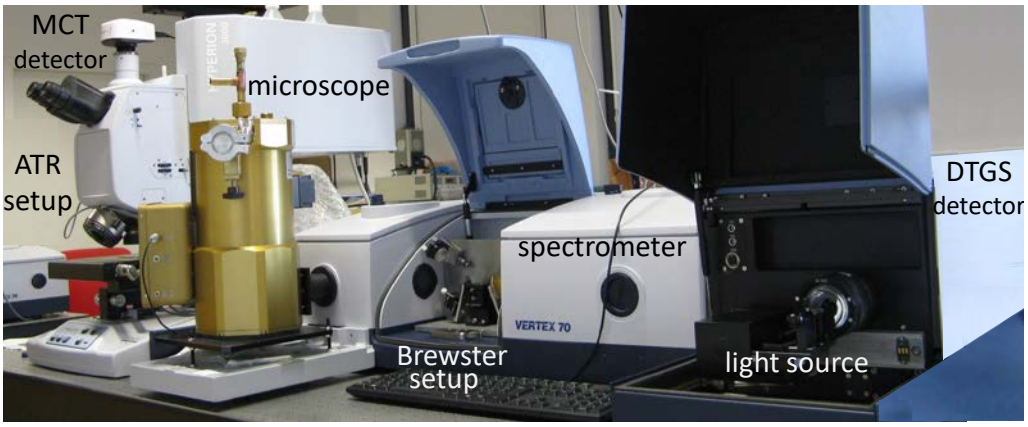


Figure 4.10: Experimental setup for reflectance spectroscopy, showing the light source, the Brewster and ATR setups, the microscope, the spectrometer and the detectors.

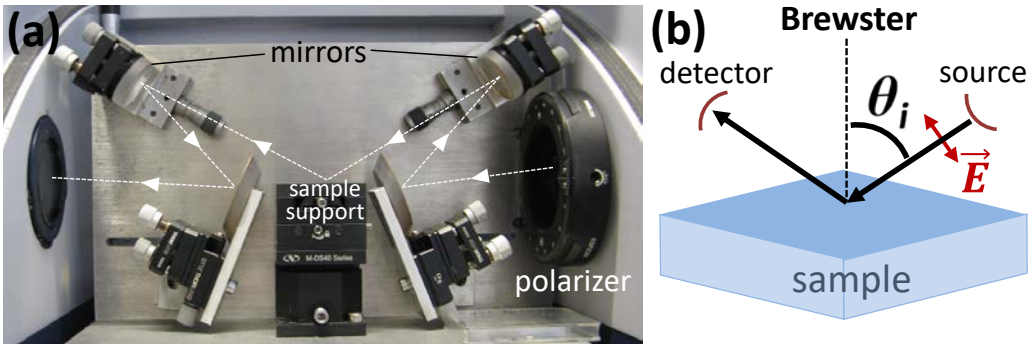


Figure 4.11: (a) Brewster setup: the white dashed line represent the light path from the polarizer, between the mirrors and up to the detector area. **(b)** Sketch of the Brewster configuration, with *p*-polarized light incident at an angle θ_i to the normal to the surface.

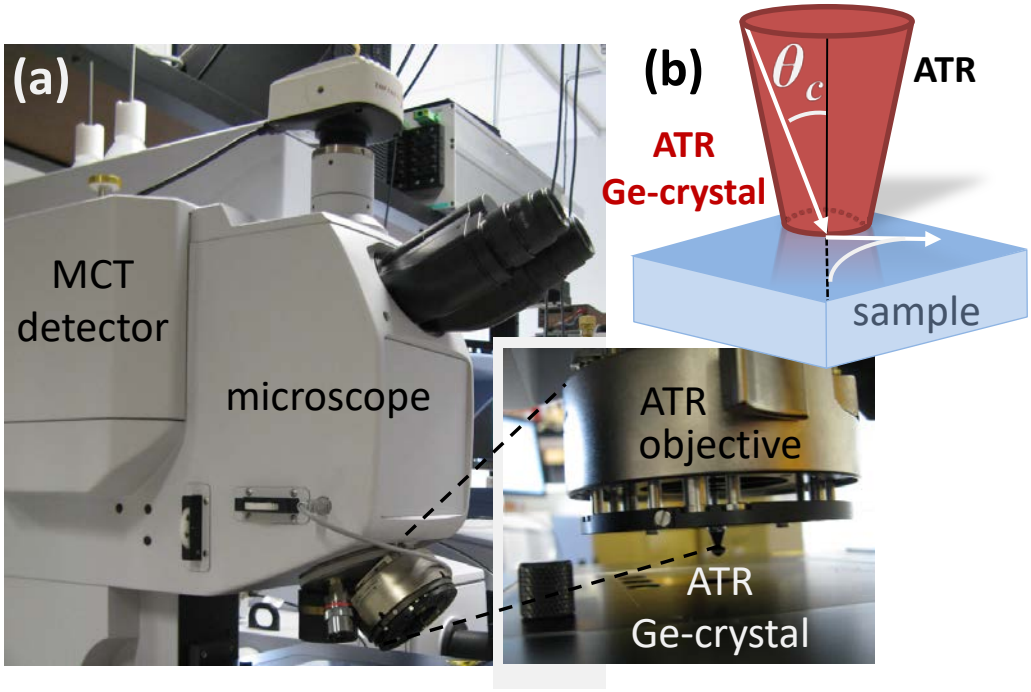


Figure 4.12: (a) ATR setup: the zoom shows the ATR objective and crystal attached to the microscope. **(b)** Sketch of the ATR configuration: light from a Ge prism undergoes total internal reflection at the interface with air at angles higher that the critical angle θ_c .

turn, these excite a surface plasmon polariton (SPP) mode. The reflected light beam is detected using a mercury cadmium telluride (MCT) detector. It should be noted that the light excitation in the ATR setup occurs in the so-called Otto configuration[149], *i.e.* with a thin air gap between the Ge prism and the sample surface, due to a natural mis-orientation of the substrate or by using a controlled wedge. It is also possible to acquire spatial maps of the ATR signal: these are obtained by using a 15× objective, a focal planar array (FPA) with a spatial resolution of 2.5 μm at a wavelength λ = 2.5 μm, and by integrating the reflectance intensity variation with respect to a base line.

4.3.3 Electroluminescence (EL) spectroscopy

The electroluminescence (EL) spectroscopy measurements were carried out by myself at Lancaster University. Electroluminescence experiments enable the study of the recombination of electron-hole pairs that are electrically injected in a semiconductor, as sketched in Figure 4.13 for our *p*-*i*-*n* RTDs.

The experimental setup is sketched in Figure 4.14. The samples are mounted onto a cold finger placed inside an Oxford Instruments cryostat, which comprises of two chambers. The inner chamber, where the sample lies, is evacuated to 10^{-1} mbar using a rotatory pump and then back-filled with helium gas in order to enable heat transfer and cooling to a temperature down to $T \sim 6$ K. The outer chamber is held under vacuum at a pressure of 10^{-2} mbar throughout the cooling process using the rotatory pump for isolation from the external environment. A diaphragm pump is used to transfer the liquid helium from the dewar via the transfer arm into the cryostat. The temperature of the sample can be adjusted using a temperature controller, which regulates the heaters inside the cryostat; a Si diode placed next to the sample allows a more

accurate estimate of the temperature in the sample space. This enabled us to perform temperature studies between 6 K and 300 K. We measure the current-voltage (*I*-*V*) characteristic of the RTD at 6 K < *T* < 300 K by using a DC voltage source, as explained in Section 4.2.1.

The current injected into the device is provided by an Agilent 8114A pulse generator using a 1 kHz pulse frequency with a 50% duty cycle, which is synchronized with a Stanford Research Systems SR810 DSP lock-in amplifier. We estimate the current flowing in our device, I, by measuring the current flowing across an external load (R_{load}) connected to a Tektronix TDS 210 oscilloscope. By measuring the voltage drop across the load (V_{load}), we estimate $I = V_{load}/R_{load}$. From the $I - V$ curve acquired at each temperature for our device (see Section 4.2.1) we then estimate the voltage drop, V, across the diode.

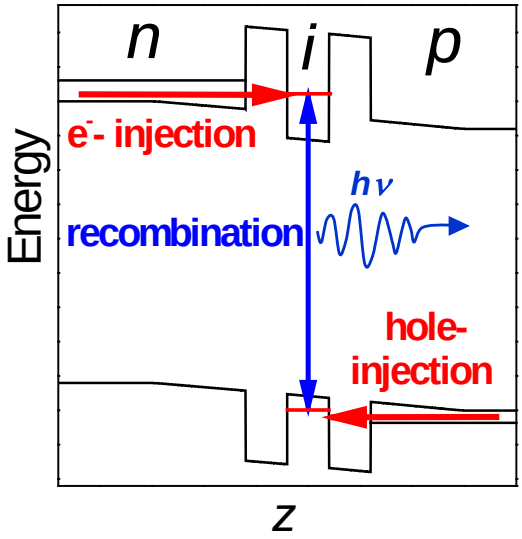


Figure 4.13: Sketch of the energy band diagram of our *p*-*i*-*n* RTDs and its electroluminescence: electrons and holes are electrically injected into the semiconductor from the *n*- and *p*- sides of the structure, respectively; the electron-hole pair then recombines in the intrinsic (*i*) region, emitting a photon of energy $h\nu$.

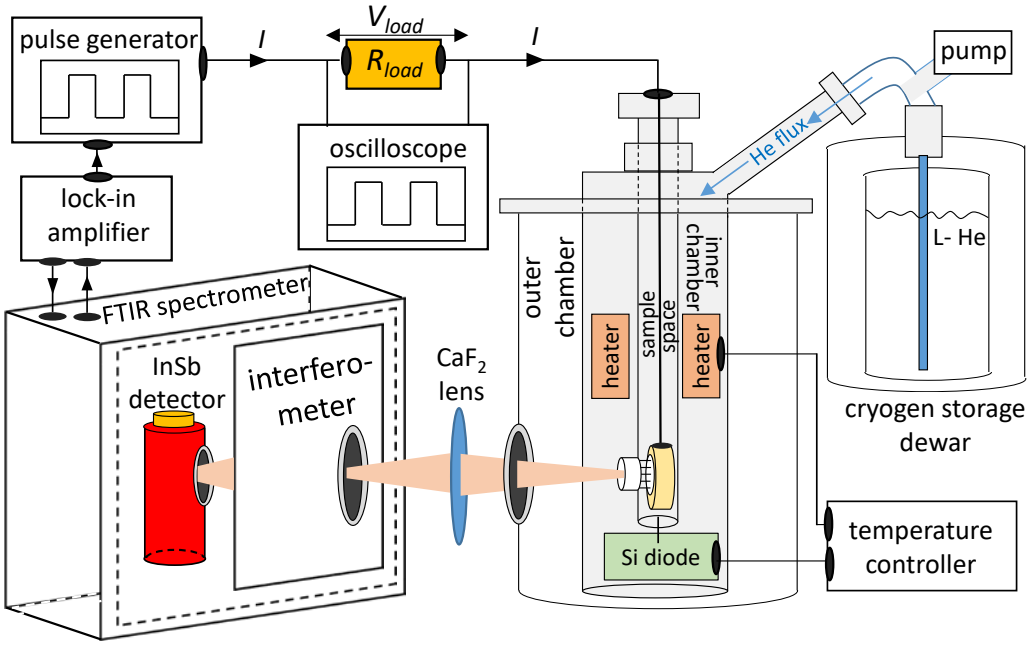


Figure 4.14: Sketch of the experimental setup used for the electroluminescence (EL) studies.

The light emitted from the sample is collected through a CaF_2 lens and focused into a Bruker Vertex 70 Fourier Transform Infrared (FTIR) spectrometer. Here the beam is collimated and directed onto a KBr beam splitter. A set of mirrors constitutes the internal interferometer and enables to scan the interference beam for different wavelengths. The spectral response is calculated by processing the obtained interferogram using a Fourier transform. One of the main advantages of FTIR spectroscopy with respect to dispersive monochromators is that the entire spectrum is measured in a single scan as a function of time, while a normal grating only measures over a narrow range of wavelengths at a time, collecting a small fraction of the signal for each wavelength. The signal is detected by an InSb detector cooled down to 77 K by using liquid nitrogen, amplified by the lock-in amplifier, sent back to the FTIR and processed by an OPUS software.

4.4 Experimental techniques: topographical studies

4.4.1 Scanning electron microscopy (SEM)

A JEOL JSM-7100F field emission gun-SEM (FEG-SEM) (Figure 4.15) was used to investigate the samples in this study. A schematic diagram of an SEM is shown in Figure 4.16. The FEG electron source is a thermal Schottky-type emitter in which a tungsten tip is coated with zirconium oxide giving enhanced thermionic emission to produce a beam with a smaller diameter, a current with a greater density and higher brightness compared to conventional thermionic emitters (such as a simple tungsten hairpin filament). The beam is accelerated down the column typically with an accelerating voltage of 15kV and is then demagnified by a series of electromagnetic lenses whilst the condenser

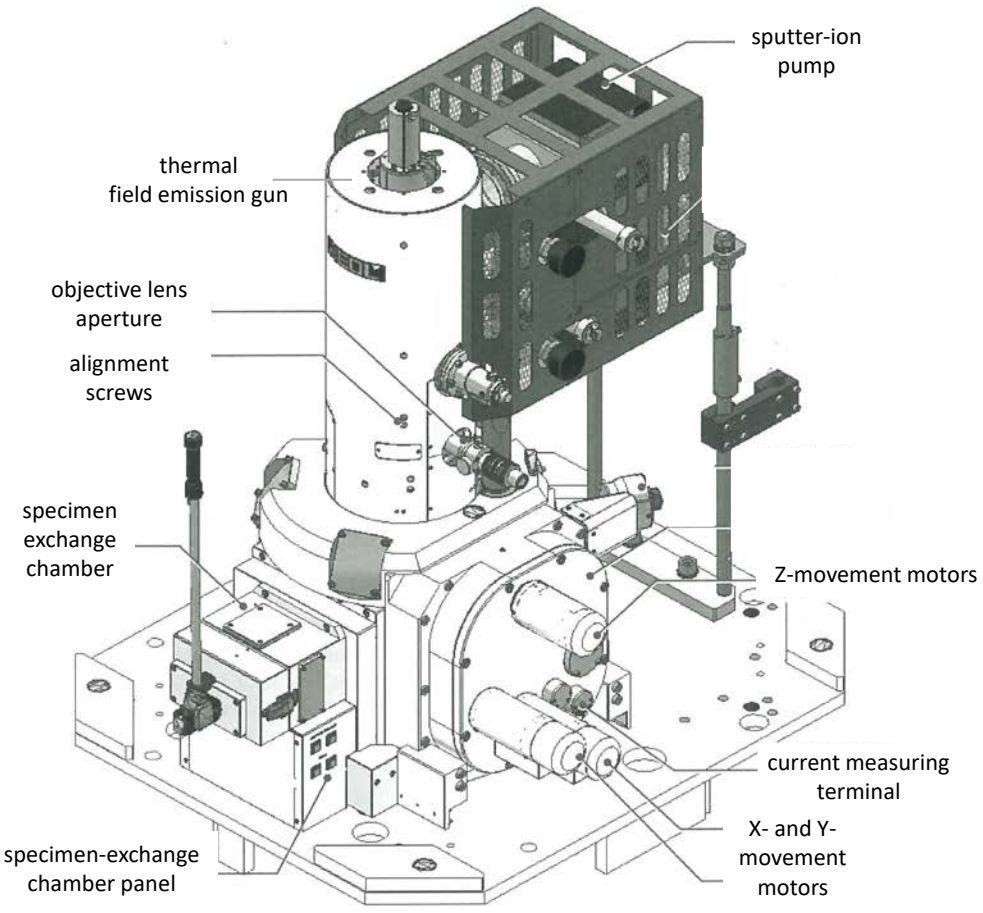


Figure 4.15: Diagram of a JEOL JSM-7100 FEGSEM (adapted from [169]).

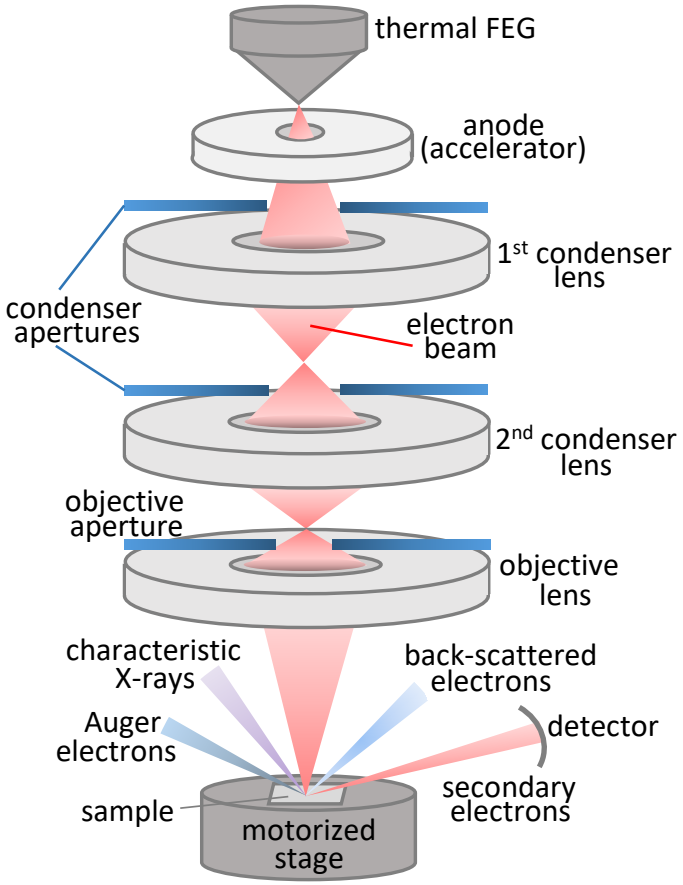


Figure 4.16: Schematic diagram of the main components of an SEM.

apertures help to eliminate high-angle electrons from the beam. The first condenser lens forms the beam and limits the current ("coarse control"), while the second condenser lens makes the beam narrower and coherent ("fine control"). A current measuring terminal with a probe current detector (PCD) enables the measure of the electron beam current that the specimen is exposed to; this value can be controlled by changing the objective lens aperture and/or the microscope's spot size control, according to the desired type of imaging or analysis. For example, the objective aperture can be set to a diameter d = 30, 50, 70 and 110 μm. Finally, the objective lens focuses the beam into a small probe, which is scanned across the specimen surface to create an image.

The interaction of the electron beam with the specimen induces the emission of secondary electrons, which are collected by a detector for secondary electron imaging (SEI). Upon the interaction of the electron beam with the sample, high energy back-scattered electrons (BSE), Auger electrons and characteristic X-ray radiation are also produced. This radiation can be detected and is commonly used to study the elemental composition or crystallographic structure of specimens.

High vacuum conditions ($< 10^{-6}$ Pa) in the microscope column and specimen chamber are achieved by using a turbomolecular pumping system. These conditions are required to enable a long mean free path for electrons, eliminate electrical discharge around the field emitter area, preserve the filament from burning while the accelerating voltage is operational, and reduce contaminations.

The 7100F enables a magnification of > ×500,000 and has a spatial resolution of 1.2 nm and 3.0 nm for an accelerating voltage $V = 30$ kV and 1 kV, respectively. The spatial resolution depends on the electron spot size, which is controlled by condenser lenses, as well as the objective aperture size and the accelerating voltage. The surface topography of our epilayers at different points was imaged by moving the sample with respect to the electron beam with a motorized stage along the plane (*XY*) or perpendicular to it (*Z*). The sample support can also be rotated in the plane or tilted.

The 7100F also enables the direct observation of the specimen surface at a controlled temperature up to 950 °C. For this purpose, the sample is mounted on a Murano 525 Gatan *in situ* heating stage, shown in Figure 4.17. The transferable carriage assembly is coupled with mating electrical contact pins for a heater and a temperature sensor. The sample is mounted on a consumable

semiconductor hotplate made of silicon by using a high temperature carbon paste. The silicon hotplate is in turn located on a ceramic block support. A power booster provides power up to 20 W, while the temperature of the hotplate is controlled by a USB temperature controller, which displays the temperature of a thermocouple that is contacted with the rear of the hotplate. The cooling of the system is realized by a water recirculating system[170].

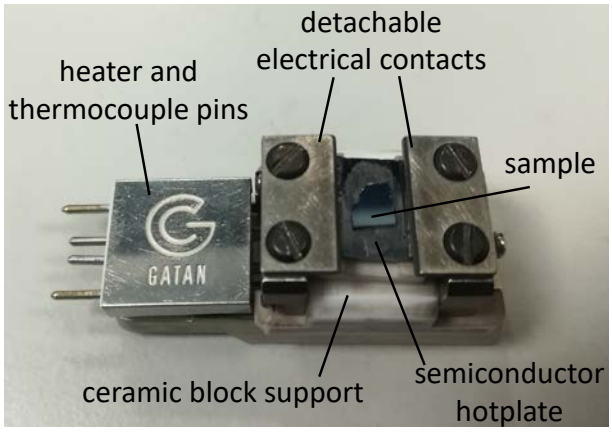


Figure 4.17: Murano 525 Gatan *in situ* heating stage: transferable carriage assembly.

4.4.2 Atomic force microscopy (AFM)

A MFP-3D atomic force microscope was used to study the surface morphology of the In(AsN) and In(AsN):H epilayers. The system enables a sub-angstrom resolution along the *Z* direction (depth) and nanometre resolution along the *XY* plane.

A schematic diagram of the AFM is shown in Figure 4.18: it consists of a low spring constant cantilever with a sharp tip, an IR laser and a four-quadrant-photodiode used as a deflection sensor. The tip of the cantilever is situated close to the sample surface, thus responding to the short range repulsive forces (~ 10 nN) between the tip and the sample surface during the scanning process. The

laser is focused onto the back side of the cantilever and reflected onto the photodiode, which measures the deflection or oscillation amplitude. A feedback controlled piezo enables to correct these deflections to a constant value by triggering the cantilever in the *Z* direction. The feedback voltage from the piezo is correlated to a voltage-distance calibration factor, thus enabling the determination of the morphology at a given *XY* position on the surface. The advantage of AFM is to display the surface coordinates in all three directions without the limitation given by light diffraction in optical microscopes. In order to assess the topographical quality of the surface, the AFM was operated in the non-contact tapping mode.

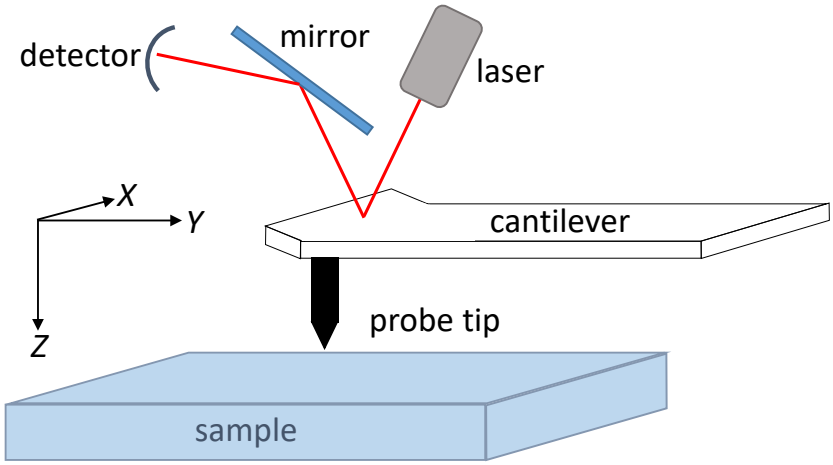


Figure 4.18: Schematic diagram of an atomic force microscope (AFM).

Chapter 5

Mid-infrared plasmonics in highly H-doped In(AsN)

This chapter demonstrates that mid-infrared (MIR) surface plasmon polariton (SPP) modes can be excited in highly H-doped In(AsN) epilayers. *Post-growth* hydrogenation of In(AsN) creates a highly conducting channel near the surface, whose optical excitation creates a SPP mode detected by reflectance techniques. The plasmonic response of In(AsN):H can be spatially tailored and suppressed by photo-annealing with a focused laser beam, which contributes to dissociate the N-H donor complex.

The sample layer composition and growth conditions were described in Section 4.1.1. The reflectance measurements were performed by myself at Université de Montpellier; the Raman spectroscopy studies were performed by myself at University of Nottingham. The experimental setup used for these measurements was described in Sections 4.3.1 (Raman spectroscopy), 4.3.2 (reflectance spectroscopy), and 4.4.2 (atomic force microscopy). These results were published in *Advanced Optical Materials* **6**, 1700492 (**2018**)[166].

5.1 Introduction

The field of plasmonics has rapidly grown in recent years and is a focus of research in photonics. It focuses on the interaction between electromagnetic waves and charge carriers and the resulting plasmonic resonances[149]. It is crucial to achieve high carrier densities in order to obtain detectable plasmonic

effects. For this reason, metals have traditionally been exploited for this purpose. The exploitation of metallic compounds enables the coupling with electromagnetic radiation in the visible-UV spectral range[151]. However, the mid-infrared (MIR) spectral range is still challenging[163] and requires novel materials and cost-effective methods for the fabrication and implementation in several applications, such as security, environmental control, pharmaceuticals, *etc*. For this reason, there is currently an active research path aimed at finding novel low-loss plasmonic materials[156]. Within this context, highly doped semiconductors (HDSCs) have attracted increasing attention[150, 157, 158]. Semiconductors offer high flexibility in tuning the plasmonic response by controlling the carrier density with doping, additionally to the geometrical patterning of the plasmonic grating. The lower carrier densities can be tuned to achieve plasma frequencies in the MIR spectral range. The non-trivial task of achieving high doping levels and maintaining a high crystal quality in semiconductors has encouraged the search of novel solutions to the problem[150].

5.2 Reflectance spectroscopy of surface plasmon polaritons

For these studies, we used hydrogenated In(AsN) epilayers with thickness t = 0.3 μm (1 μm) and N-content [N] = 1% (1.1%) grown by molecular-beam-epitaxy (MBE) on a GaAs substrate. The reflectance spectra on the In(AsN):H epilayers were acquired in the Brewster and the ATR configuration, as described in Section 4.3.2.

Figure 5.1a shows the reflectance spectrum acquired in the Brewster configuration. The spectrum (solid black curve) shows a dip due to a Brewster mode[162], which we model using a transfer matrix formalism (TMF) (dashed black curve in Figure 5.1a). For this model, we consider *p*-polarized light

impinging from air on a sequence of an In(AsN):H layer, a non-hydrogenated In(AsN) layer, and a semi-infinite nominally undoped GaAs substrate. We assume dielectric functions in the high frequency limit for air ($\varepsilon_1 = \varepsilon_{1\infty} = 1$), In(AsN) ($\varepsilon_{2\infty} = 12$), and GaAs ($\varepsilon_3 = \varepsilon_{3\infty} = 10.89$). As presented in Section 4.1.1, the hydrogenation conditions used for our samples enable the penetration of H for a depth t_H = 0.1 μm below the surface. The phononic and plasmonic contributions to the dielectric function of an In(AsN):H layer of thickness t_H are modelled as:

$$\varepsilon_2(\omega, g, \omega_p) = \varepsilon_{2\infty}\left(\frac{\omega_{LO}^2-\omega^2-i\gamma\omega}{\omega_{TO}^2-\omega^2-i\gamma\omega} - \frac{\omega_p^2}{\omega^2+ig\omega}\right), \quad (5.1)$$

where ω_{TO} = 218 cm^{-1} and ω_{LO} = 239 cm^{-1} are the frequencies of the transverse optical (TO) and longitudinal optical (LO) phonons, respectively, and γ = 2.4 cm^{-1} is the phonon broadening. The values of the plasma broadening, g = 90 cm^{-1}, and of the plasma frequency, ω_p = 985 cm^{-1}, are estimated from the fit to the data. Similar values are obtained for In(AsN):H epilayers with different thickness t (see Table 1). The values of ω_p correspond to electron densities n_e = 8×10^{18} cm^{-3} (t = 0.3 μm) and 9×10^{18} cm^{-3} (t = 1 μm). Non-parabolic effects on the first derivative electron mass, $m_e^* = \hbar^2 k/[d\varepsilon(k)/dk]$, due to the electron density are accounted for by modelling the electron energy dispersion as $\varepsilon(k)[1 + \alpha\varepsilon(k)] = \hbar^2 k^2/m_0^*$, where α = 2 eV^{-1}, m_0^* = 0.025 m_0 at k = 0, and m_0 is the electron mass in vacuum[171]. The difference in electron density is attributed to the ~10% difference in the N-content in the two samples. These electron densities are also significantly larger than those in as-grown In(AsN) ($n_e \sim 10^{17}$ cm^{-3})[97, 172].

Table 1. Frequencies of the plasma (ω_p) and of the surface plasmon polariton (ω_{spp}) modes in In(AsN):H epilayers. The value of ω_p is estimated by fitting the reflectance spectra in the Brewster configuration (a) and from the Raman shift of the L_b^+ mode (b); ω_{spp} is obtained from the ATR spectra (c) and from our calculations (d).

Sample	ω_p [a)] [cm^{-1}]	ω_p [b)] [cm^{-1}]	ω_{spp} [c)] [cm^{-1}]	ω_{spp} [d)] [cm^{-1}]
t = 0.3 μm	985	975	890-950	930
t = 1 μm	1050	1030	970-1000	990

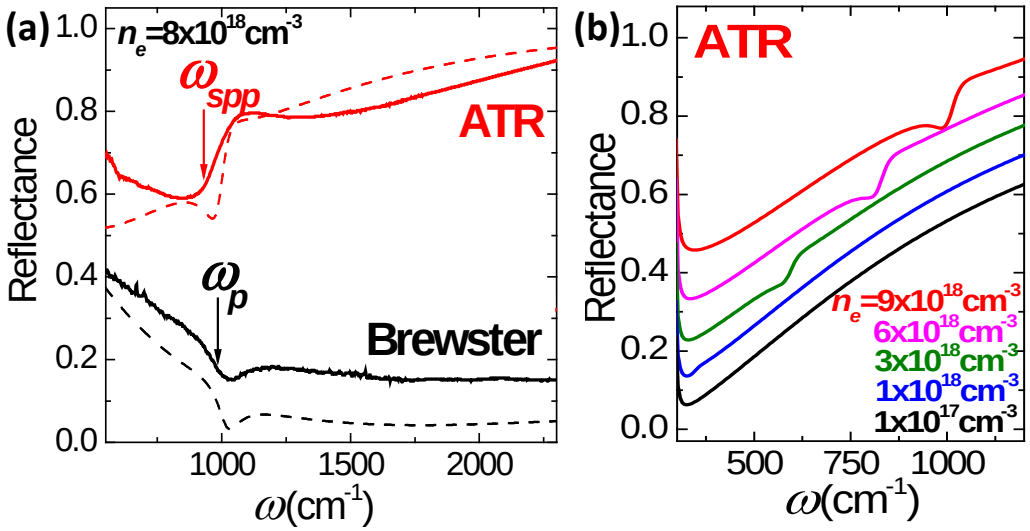


Figure 5.1: (a) Reflectance spectra for the In(AsN):H sample with epilayer thickness t = 0.3 μm and hydrogenated layer thickness t_H = 0.1 μm in the Brewster (solid black line) and ATR (solid red line) configuration. The dashed curves represent the spectra as modelled with a transfer matrix formalism. (**b)** Simulations of reflectance spectra in the ATR configuration for different carrier densities, n_e. For clarity, the spectra are shifted along the vertical axis relative to the curve at $n_e = 1\times10^{18}$ cm^{-3} (blue curve).

The reflectance spectrum acquired in the ATR configuration shows a dip at frequency ω_{spp} ~ 900 cm^{-1} corresponding to the SPP mode (solid red curve in Figure 5.1a). In Figure 5.1b we show simulations of the reflectance spectra in the ATR configuration for different carrier densities, n_e. The frequency ω_{spp} of the measured SPP mode is reproduced by the simulations for $n_e = 9\times10^{18}$ cm^{-3}. Decreasing n_e causes a red-shift and weakening of the SPP mode. In particular, for carrier densities comparable to those observed in as-grown In(AsN) (n_e ~ 10^{17} cm^{-3})[97, 172], the reflectance spectrum shows no resonance, as also observed experimentally.

The ATR spectra were acquired at different positions, separated by 100 μm or 1 mm (see the Insets in Figure 5.2a-b, respectively). In Figure 5.2, we plot the signal as ATR $= -\log(I_R/I_I)$, where I_R and I_I are the intensities of the reflected and incident light beam, respectively. We observe that the frequency of the SPP resonance peak is non-homogenous over length scales of ~ 1 mm (Figure 5.2b). This variation is likely to be caused by the inhomogeneity of the as-grown material[102]. We assess the large-scale non-uniformity of as-grown In(AsN) by Raman spectroscopy. The Raman maps in Figure 5.3a reveal a non-

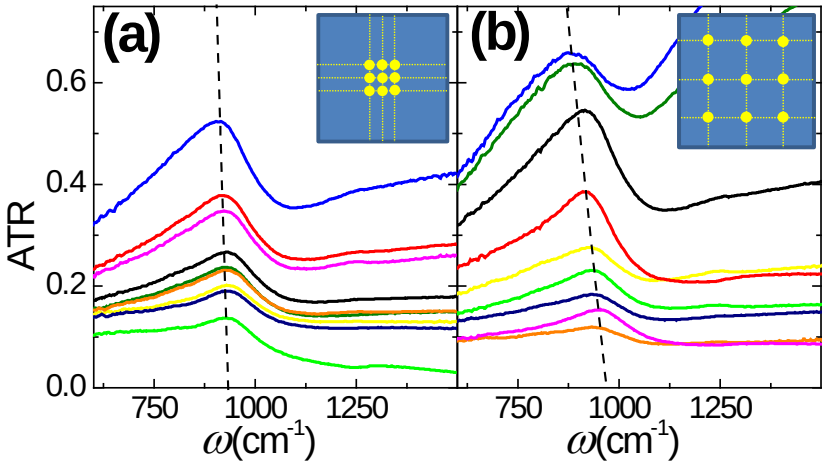


Figure 5.2: ATR spectra at positions separated by 0.1 mm **(a)** and 1 mm **(b)** for the In(AsN):H sample with thickness t = 0.3 μm.

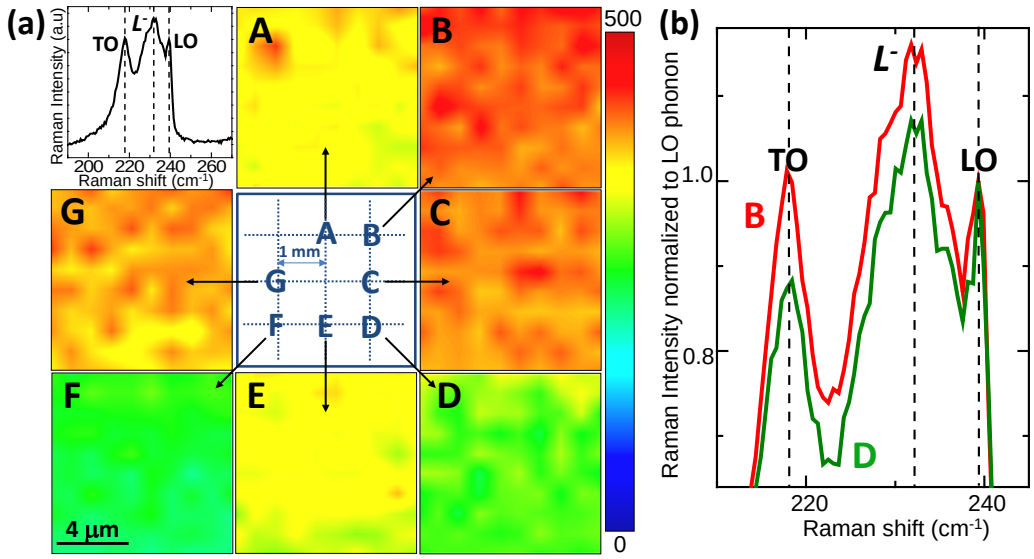


Figure 5.3: (a) Raman maps of the integrated intensity of the TO and LO phonons on as-grown In(AsN) (t = 0.3 µm). The maps are acquired in the spectral range 200-260 cm^{-1} over the areas A-G, separated by a distance of 1 mm. Inset: representative Raman spectrum showing the TO, L^- and LO modes. **(b)** Representative Raman spectra normalized to the LO phonon intensity. The spectra are acquired at positions B and D.

uniform intensity of the Raman signal in the frequency range of the TO and LO phonons (Inset of Figure 5.3a). This non-uniformity is accompanied by changes in the relative intensity of the TO (I_{TO}), L^- (I_-) and LO (I_{LO}) modes. The TO and L^- modes are forbidden in the back-scattering configuration and thus disorder-activated[173, 174]. As shown in Figure 5.3b, the intensity ratios I_{TO}/I_{LO} and I_-/I_{LO} change by ~ 10% over a 2 mm distance, indicating a large-scale non-uniformity of as-grown In(AsN), as also assessed by other techniques[102]. The non-homogeneous N-content and defects in In(AsN) may thus induce a non-uniform hydrogen incorporation. However, as mentioned in Section 4.1.1, we note that the hydrogenation process is uniform: the standard deviation of the

H-beam Gaussian profile (σ ~ 2.5 cm) is much larger than the sample size (~ 0.4 cm). Plasmonic devices can be still developed on length scales where these variations are small (< 100 μm, Figure 5.2a). We measure values of ω_{spp} ranging from 890 to 950 cm^{-1} (970-1000 cm^{-1}) for t = 0.3 μm (t = 1 μm). These are smaller than ω_p and match well those obtained by modelling the SPP dispersion for a single interface between air (ε_1 = 1) and the In(AsN):H epilayer $\left(\varepsilon_2(\omega) = \varepsilon_{2\infty} - \frac{\omega_p^2}{(\omega^2 + ig\omega)}\right)$, see dashed red curve in Figure 5.1a and the corresponding values in Table 1.

As further explained in Section 3.2, the dispersion of the SPP mode is given by

$$\omega = ck_{//}\sqrt{\frac{[\varepsilon_1+\varepsilon_2(\omega)]}{\varepsilon_1\varepsilon_2(\omega)}}, \tag{5.2}$$

where c is the speed of light in vacuum and $k_{//}$ is the component of the

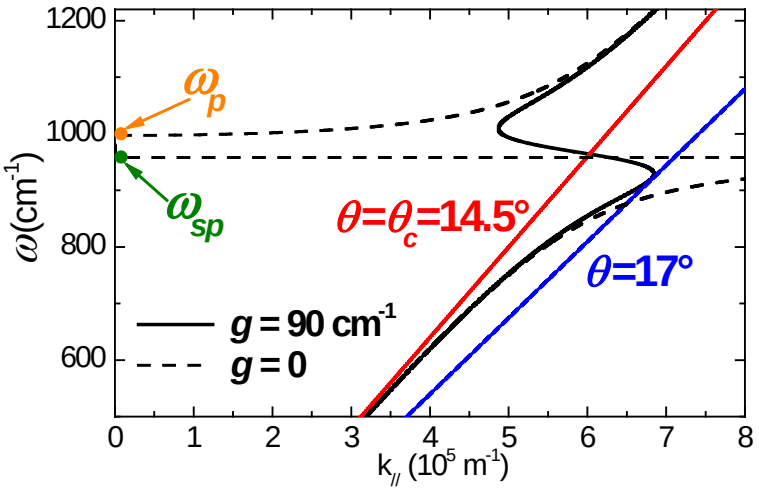


Figure 5.4: Dispersion for the SPP mode with broadening g = 0 (dashed black curve) and g = 90 cm^{-1} (solid black curve). The straight lines represent dispersions of the light cones from the Ge prism at $\theta = \theta_c$ = 14.5° (red line) and θ = 17° (blue line). The plasma (orange dot) and surface plasmon (green dot) frequencies are also shown at $k_{//}$ = 0.

wavevector parallel to the interface[149]. Figure 5.4 shows the dispersion calculated for negligible plasma broadening, $g = 0$ (dashed black curve), and finite plasma broadening, $g = 90$ cm^{-1} (solid black curve). As indicated in Figure 5.4, the SPP resonance can be excited if light from the Ge prism is incident at angles $14.5° < \theta < 17°$, consistent with the requirement for total internal reflection.

As introduced in Section 4.3.2, an air gap between the Ge prism and the In(AsN):H layer is required to achieve total internal reflection and thus observe the SPP mode in the so-called Otto configuration[149]. This can occur due to the natural tilting of the sample or can be induced intentionally. Figure 5.5a shows a colour map of the integral of the reflectance intensity in the spectral range of the SPP mode. This reveals an intensity gradient, thus suggesting a natural tilting of the surface and the existence of an air gap between the Ge prism and the In(AsN):H epilayer. The blue areas in the colour map correspond to regions with a larger air gap, thus leading to total internal reflection and the SPP resonance (Figure 5.5b). We estimate a small tilting of the surface at an angle $\phi^* \sim 0.5°$. This corresponds to an air gap t_{air} of up to ~ 0.9 μm, consistent with the value obtained from the simulation of the ATR spectrum in Figure 5.1a ($t_{air} = 1$ μm, dashed red curve). We estimate the natural tilting of the epilayer by performing the ATR studies for different tilted angles of the sample relative to the horizontal support, *i.e.* $\phi = 0°, \pm 1°$, *etc* (see sketch in Figure 5.5c). Since in both the $\phi = 0°$ and $\phi = -1°$ configurations the ATR spectra are the same, by taking into account that the Ge prism has a cylindrical symmetry, we deduce that the natural tilting of the epilayer is $\phi^* \sim 0.5°$. From the diameter of the contact zone of the Ge prism, $d_{Ge} = 100$ μm, we thus estimate an air gap of up to ~ 0.9 μm.

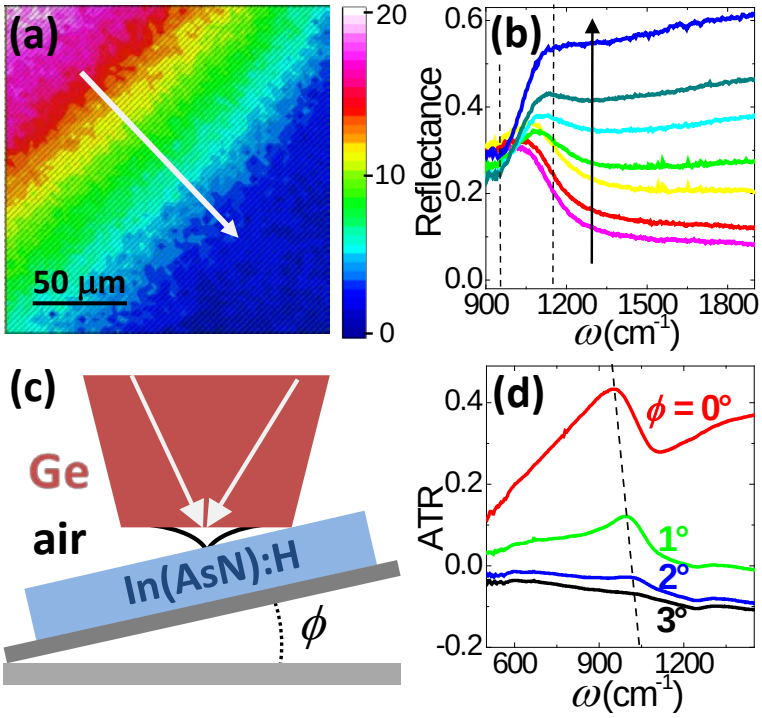


Figure 5.5: (a) Integrated intensity of the reflectance signal from 950 cm^{-1} to 1150 cm^{-1} for the In(AsN):H sample with thickness t = 1 µm. **(b)** Reflectance spectra in the ATR configuration acquired along the white arrow in the colour map. **(c)** Sketch of the modified ATR setup: the sample is tilted by an angle ϕ relative to the horizontal support. This creates an air gap between the Ge prism and the In(AsN):H epilayer. d) ATR spectra at various angles ϕ = 0°- 3°.

To probe further the role of this air gap, the ATR spectra were acquired for different tilted angles ϕ = 0°- 3° of the In(AsN):H epilayer relative to the horizontal support of the sample (Figure 5.5c-d): the SPP resonance tends to weaken and to blue-shift with increasing ϕ. We attribute this behaviour to the increase of the air gap with ϕ, thus leading to the exponential decay of the evanescent wave and a modified SPP ω-$k_{//}$ dispersion.

5.3 Raman spectroscopy of plasma modes

Further insights into the plasmonic effects were inferred from Raman spectroscopy studies. These were performed in the back-scattering configuration with incident light of wavelength λ = 633 nm and power $P \sim 1$mW. In Figure 5.6a, left panel, the comparison of the Raman spectrum of In(AsN) (blue curve) with that of In(AsN):H (red curve) evidences a broad feature L_s^- ($\omega_s^- = 232$ cm^{-1}) between the TO (ω_{TO} = 218 cm^{-1}) and LO (ω_{LO} = 239 cm^{-1}) phonon frequencies. This feature weakens upon H-incorporation. The same comparison also shows the insurgence of a phonon-plasmon coupled mode, L_b^+, centred at 975 cm^{-1}, in the Raman spectrum of In(AsN):H (red curve in Figure 5.6a, right panel).

The frequencies of the phonon-plasmon coupled modes, $L_b^\pm$, for bulk In(AsN):H and in the limit of wavevector $k \approx 0$ are shown in Figure 5.7a and are given by[175]:

$$\omega_b^\pm = \frac{1}{\sqrt{2}}\sqrt{\left(\omega_p^2 + \omega_{LO}^2\right) \pm \sqrt{\left(\omega_p^2 + \omega_{LO}^2\right)^2 - 4\omega_p^2\omega_{TO}^2}}\,. \qquad (5.3)$$

The position of the L_b^+ mode, which has a strong dependence on n_e, corresponds to a plasma frequency consistent with that estimated from the reflectance spectra in the Brewster configuration (see Table 1). The Raman shift of the corresponding L_b^- mode is expected to coincide with that of the TO mode (ω_b^-= 218 cm^{-1}) at $n_e \sim 10^{19}$ cm^{-3}.

As regards the L_s^- mode, it is well known that a two-dimensional (2D) surface accumulation layer forms in InAs[133, 176] and In(AsN)[172]. This enables a coupling with the unscreened LO phonon and involves scattering at high

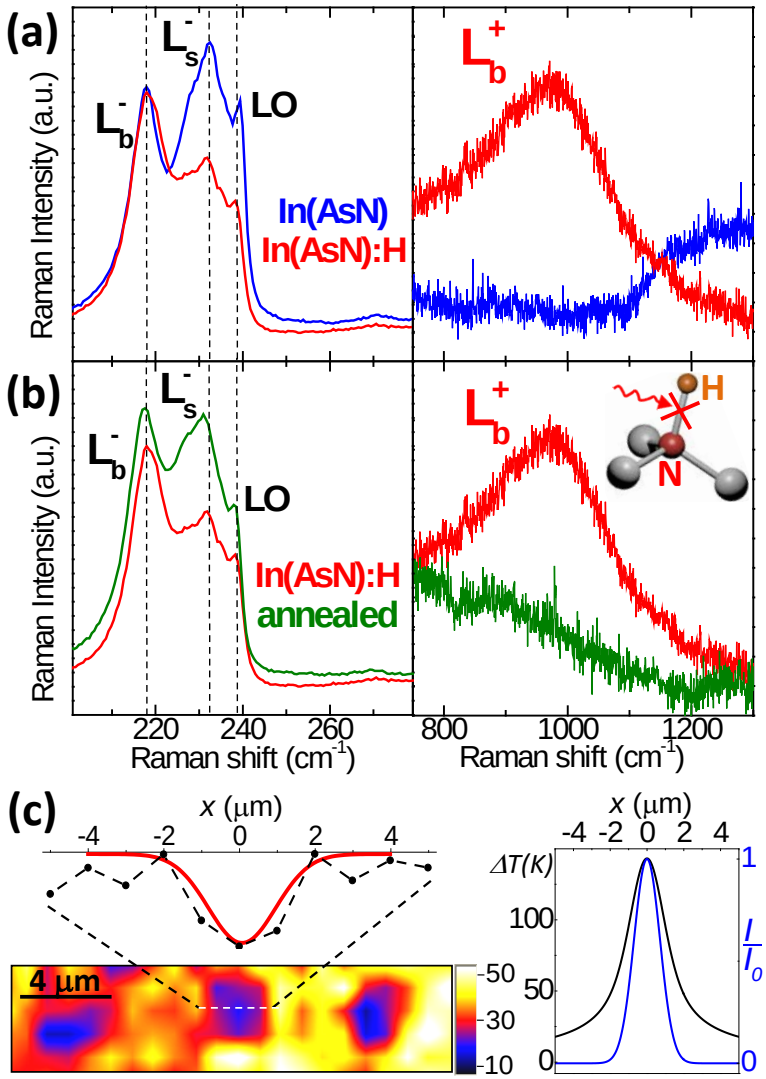


Figure 5.6: a) Raman spectra showing the L_b^-, L_S^-, LO (left panel) and L_b^+ (right panel) modes in In(AsN) (blue curve) and In(AsN):H (red curve). **b)** Raman spectra showing the L_b^-, L_S^-, LO (left panel) and L_b^+ (right panel) modes in In(AsN):H before (red curve) and after (green curve) laser annealing. Inset: sketch of the dissociation of the N-H bond due to laser excitation. **c)** Left: map of the L_b^+ intensity after laser annealing of three different spots, and profile of the L_b^+ intensity along the white dashed line: dots connected by black dashed lines are the data, the continuous red curve is the Gaussian fit to the data. Right: temperature increase, ΔT, for laser impinging power P = 10 mW (black line) and normalized intensity of the laser beam, I/I_0, (blue line) versus position x.

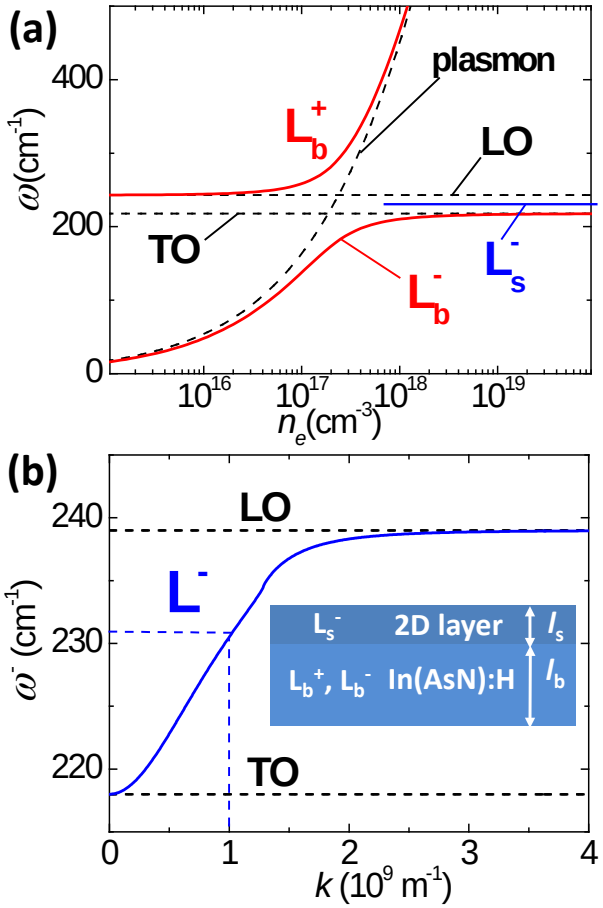


Figure 5.7: (a) Frequency of the phonon-plasmon coupled modes, $L_b^{\pm}$ (red curves) and L_s^- (blue curve), as a function of the electron density n_e in In(AsN):H. Here *b* and *s* stand for *bulk* and *surface*, respectively. The black horizontal dashed lines represent the TO and LO phonons, while the dashed black curve represents the plasmon dispersion. **(b)** Frequency of the L^- mode, ω^-, (solid blue line) as a function of wavevector *k*, between the LO and TO phonons (horizontal dashed black lines). Inset: sketch of the 2D accumulation layer of thickness l_s at the surface of a bulk In(AsN):H layer of thickness l_b .

wavevectors *k*. For a layer extending over a typical length l_s, the range of allowed wavevectors is $\Delta k \sim 2/l_s$, which can be comparable with the Thomas-Fermi screening wavevector. In this case, the surface LO-plasmon coupled

mode, L_s^-, can be at a frequency intermediate between ω_{TO} and ω_{LO}[173, 174, 177] (Figure 5.7b). We model the modification of the ω^- dispersion as (Figure 5.7b):

$$\omega^- = \sqrt{\omega_{TO}^2 + \frac{(\omega_{LO}^2 - \omega_{TO}^2)}{\varepsilon(k,\omega)}}\ , \tag{5.4}$$

where $\varepsilon(k,\omega)$ is the frequency and wavevector dependent dielectric function[177]. Given that $\omega_p >> \omega_{LO}$, we use the static value of the dielectric function:

$$\varepsilon(k,0) = 1 + \frac{k_s^2}{k^2}\left[0.5 + \frac{k_F}{2k}\left(1 - \frac{k^2}{4k_F^2}\right) ln\left(\left|\frac{k+2k_F}{k-2k_F}\right|\right)\right], \tag{5.5}$$

where $k_F = (3\pi^2 n_e)^{1/3} \sim 6\times10^8$ m^{-1} is the Fermi radius of the filled sphere in the conduction band and $k_S = \sqrt{\frac{k_F m_e^* e^2}{\pi^2 \hbar^2 \varepsilon_r \varepsilon_0}} \sim 3\times10^8$ m^{-1} is the Thomas-Fermi screening wavevector[177]. From the calculated dispersion, we estimate that the measured position of the L_s^- mode corresponds to a surface accumulation layer with thickness $l_s \sim 2$ nm. In summary, the Raman spectra reveal the "surface" L_s^- mode at $\omega_s^- = 232$ cm^{-1}, the "bulk" L_b^- mode at $\omega_b^- = 218$ cm^{-1}, and the L_b^+ mode at $\omega_b^+ = 975$ cm^{-1}.

5.4 Tuning plasma modes by laser annealing

To study the tunability of plasmonic effects, the In(AsN):H samples were photo-annealed with a focused laser beam with λ = 633 nm (Inset in Figure 5.6b). The light diffraction limit at this wavelength is given by the laser spot diameter $d = 1.22\,\lambda$ / NA ~ 1 μm, where NA (= 0.8) is the numerical aperture of our 100× objective. The annealing was performed at impinging powers up to P = 15 mW and exposure times $\tau \geq 300$ s. As shown in Figure 5.6b, following the laser annealing the intensity of the L_s^- mode is almost fully restored to that of the In(AsN) sample (left panel) and the L_b^+ feature disappears (right panel). This suggests the dissociation of the N-H bond and the local removal of hydrogen

from the lattice (see Inset of Figure 5.6b, right panel), thus restoring locally the pristine conditions of as-grown In(AsN).

Figure 5.6c (bottom left panel) shows the Raman map of the L_b^+ intensity over three different positions of the sample that are laser annealed. Three clear minima in the intensity are seen, thus confirming a local quenching of the L_b^+ mode. We fit the intensity distribution of the L_b^+ mode over the annealed spots with a Gaussian profile of full-width-half-maximum (FWHM) ~ 2 μm (top left panel), which is larger than the light diffraction limit (~ 1 μm). This broadening is attributed to a thermal effect[178]: we estimate that the laser beam causes a temperature rise of up to ΔT = 140 K that extends over a sample region wider than the laser spot (Figure 5c, right panel). This large increase of T is reached at relatively low powers due to the high absorption coefficient ($\alpha \sim 10^7$ m^{-1} at λ = 633 nm) and low thermal conductivity (K = 27 W m^{-1} K^{-1} at T = 300 K) of In(AsN). See Appendix B for a more detailed calculation.

We note that that the annealing conditions used in our experiment do not cause any topographic modification of the surface. Figure 5.8a shows atomic force microscopy (AFM) images of the In(AsN) layers before (left panel) and after (right panel) hydrogenation. The average surface roughness is similar (< 10 nm) in both the as-grown and hydrogenated In(AsN). Here we focus on the effect of the laser annealing on the surface topography of (InAsN):H. For the range of laser powers (P up to 15 mW at λ = 633 nm) and exposure times (τ up to 15 minutes) required to quench the L_b^+ mode, the annealing does not cause any surface damage (see spot A in Figure 5.8b-c and AFM z-profile in Figure 5.8d). Topographic changes are induced for high laser power exposures, as shown for the laser annealed spot B in Figure 5.8b-c-d, produced using P = 50

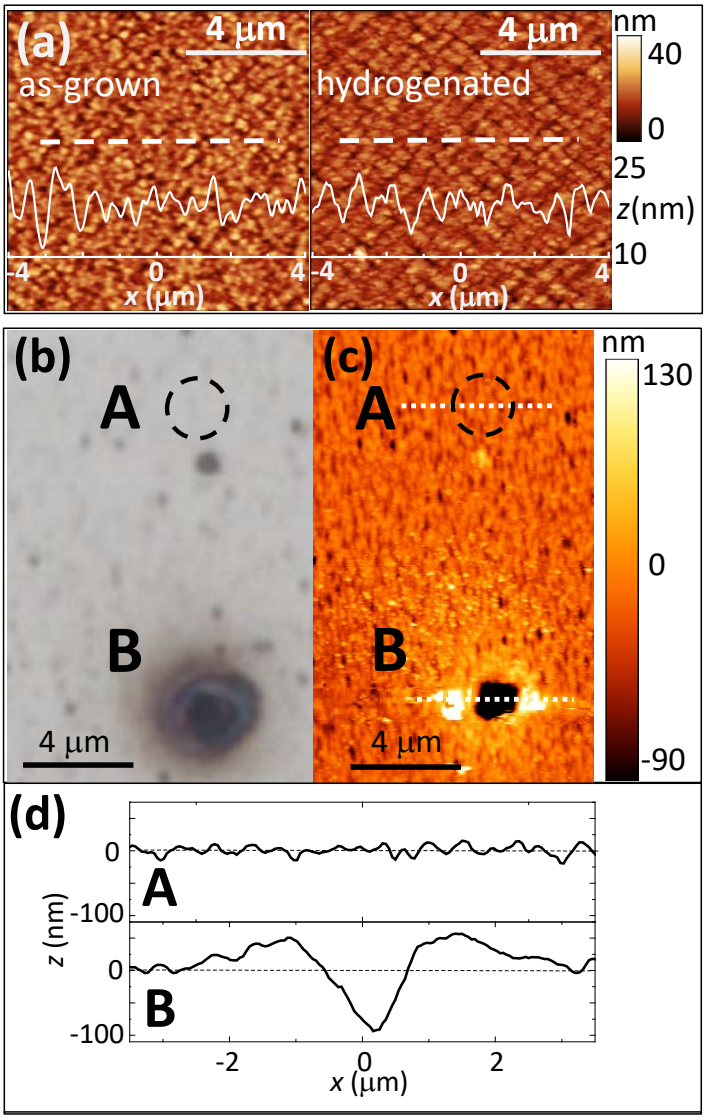


Figure 5.8: (a) AFM images of as-grown (left) and hydrogenated (right) In(AsN). Insets: *z*-profiles along the white dashed lines. **(b)** Optical image of two spots A and B in In(AsN):H) (t = 1 μm), laser annealed at powers P = 15 mW (spot A) and 50 mW (spot B. **(c-d)** AFM image (c) and *z*-profile (d) of spots A and B.

mW and τ = 120 s: a "crater" is revealed in the optical and AFM images (Figures. 5.8b-c), and the AFM *z*-profile (Figure 5.8d). This corresponds to a temperature rise of up to ΔT > 880 K, due to the decrease in thermal conductivity

at higher T [179]. The estimated temperature rise is also close to the melting temperature of InAs, T_{melt} = 940 °C.

Therefore, hydrogen-implantation followed by laser writing at powers P up to 15 mW is a reproducible and non-destructive process that paves the way to patterning on a micrometric scale the plasmonic modes of In(AsN) via a modulation of the electron density.

5.5 Summary

In summary, we have demonstrated that the incorporation of hydrogen in the dilute nitride alloy In(AsN) with [N] = 1% induces a surface plasmon polariton (SPP) mode at frequencies ω_{spp} ~ 900-1000 cm^{-1}, which correspond to MIR wavelengths λ ~ 10 - 11 μm. We attribute the occurrence of this mode to the H-enhanced electron density. The N-atoms play a key role in the incorporation of hydrogen: they trap the H-atoms, whose small size and high diffusivity in the host crystal enables an increase in the electron density up to n_e ~ 10^{19} cm^{-3} near to the surface. A similar increase of carrier density could be achieved for different N-concentrations under appropriate hydrogenation conditions[30]. We demonstrated that plasmonic effects in In(AsN):H can be selectively suppressed on a micrometre scale by a local laser annealing.

The dissociation of the N-H bond by laser writing offers a viable route to large-scale device fabrication and a means to pattern the electron density and plasmonic properties with micrometric resolution. The possibility to monitor the lateral size of the patterns, as well as the doping of the host crystal, could enable microscopic studies of plasmonic gratings and plasmonic phenomena near a surface, with potential for applications including detection of target gas

fingerprints and molecular sensing in the MIR range. Compared to the traditional doping of InAs during the growth, which requires wet chemical etching to realize plasmonic gratings, the *post-growth* H-doping of In(AsN) has potential for engineering plasmonic properties via selective hydrogen incorporation and/or removal by laser writing.

Chapter 6

Dissociation of the N-H complex by electron beam annealing

This chapter reports on preliminary studies of the effect of electron beam annealing on the dissociation of the N-H complex in the highly doped In(AsN):H semiconductor compound. These studies are conducted using the focused electron beam of a field emission gun-scanning electron microscope (FEG-SEM). The spatial distribution of the H-atoms and the surface morphology of the epilayers are probed by Raman spectroscopy and atomic force microscopy (AFM).

The SEM imaging and the Raman spectroscopy studies were performed by myself at the University of Nottingham. The sample layer composition and growth conditions are described in Section 4.1.1. The experimental setup is described in Section 4.3.1 (Raman spectroscopy), Section 4.4.1 (SEM) and Section 4.4.2 (AFM). These results are in preparation for a journal publication.

6.1 Electron beam annealing of In(AsN):H

We have shown in Chapter 5 that the dissociation of the N-H complex by laser writing enables us to modify locally the electron density, n_e, and, correspondingly, the plasmonic properties of In(AsN):H. However, this approach is limited by the diffraction limit of the laser source. Thus, it would be of great interest to develop a different method to control plasmonic properties

with nanometre spatial resolution. For example, as discussed in Section 4.4.1, a focused electron beam could achieve diffraction limits down to the nanometre scale, depending on the kinetic energy of the electrons.

The In(AsN):H samples were exposed to the focused electron beam of a field emission gun-scanning electron microscope (FEG-SEM). In our initial studies, the exposure was performed at room temperature with an accelerating voltage V_{acc} = 20 kV, impinging electron current I = 28 nA, and exposure time τ = 5 min. In order to achieve such high values of the current, the objective aperture was set to d = 70 μm. Following the exposure, images of the annealed spot were acquired by using the same FEG-SEM. The SEM imaging studies were performed with an accelerating voltage V_{acc} = 15 kV and by reducing the objective aperture to d = 30 μm, in order to obtain a smaller impinging electron current, I < 0.2 nA, and thus to avoid additional modifications of the surface.

The SEM image of a typical e-beam annealed spot is shown in Figure 6.1a. A modification of the surface is clearly visible (see dashed white circle). To assess the nature of this modification, single spot Raman measurements were acquired at different positions. Representative Raman spectra are shown in Figures 6.1b-c and correspond to positions I, II and III, indicated by the white asterisks in Figure 6.1a. The spectra were acquired by using a laser of wavelength λ = 532 nm, power P = 1 mW and acquisition time τ = 45 s. The Raman spectra show that at the position of the e-beam annealed spot (II) the plasmonic Raman mode, L_b^+ , is quenched (Figure 6.1b), suggesting a local reduction of the electron density, n_e. Also, the L_s^- mode becomes stronger than the L_b^- and the longitudinal optical (LO) phonon modes (Figure 6.1c). A similar behaviour is observed under laser annealing (see discussion in Sections 5.3-5.4).

Atomic force microscopy (AFM) studies were performed to evaluate the effect of the e-beam annealing on the surface topography. Figures 6.2a-b show the SEM (Figure 6.2a) and the AFM (Figure 6.2b) images of an e-beam annealed spot. No visible topographical modification is revealed, as shown by the AFM *z*-profile (Figure 6.2c) acquired along the dashed line in Figure 6.2b. This shows a similar average surface roughness (< 10 nm) in both the annealed and non-annealed regions. Thus a non-destructive modification of the electron density of a *post-growth* highly doped semiconductor can be achieved by e-beam writing. This is assigned to the dissociation of the N-H complex by the electron beam.

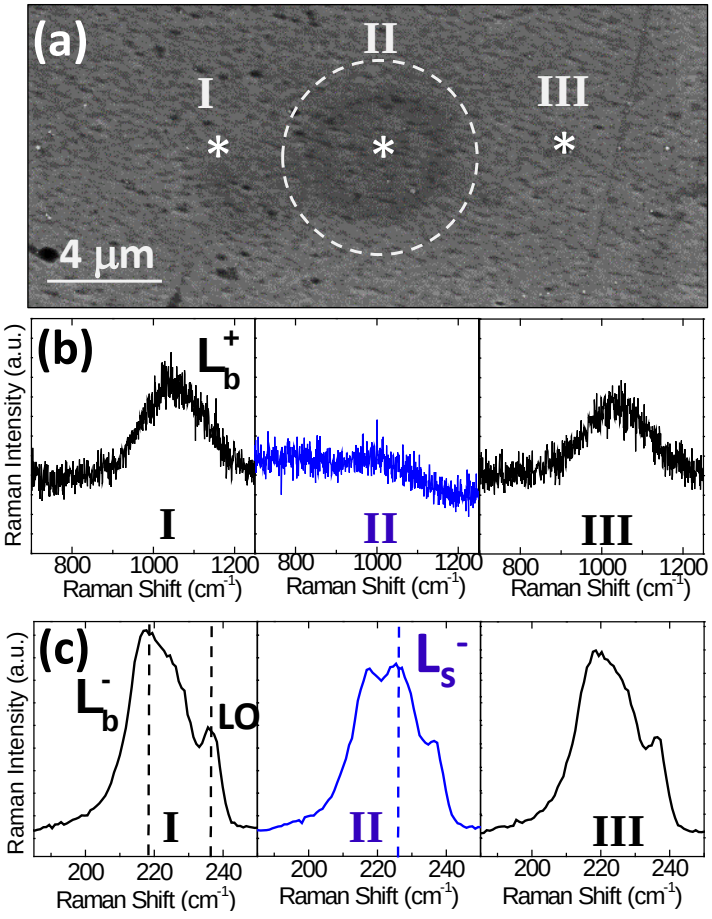


Figure 6.1: **(a)** SEM image of the sample region annealed with an e-beam (exposure: V_{acc} = 20 kV, I = 28 nA, τ = 5 min, T = 25 °C; imaging: V_{acc} = 15 kV, I < 0.2 nA). **(b-c)** Single spot Raman spectra of the plasmonic L_b^+ (b) and the L_b^-, LO and L_s^- (c) Raman modes, acquired at positions I, II and III.

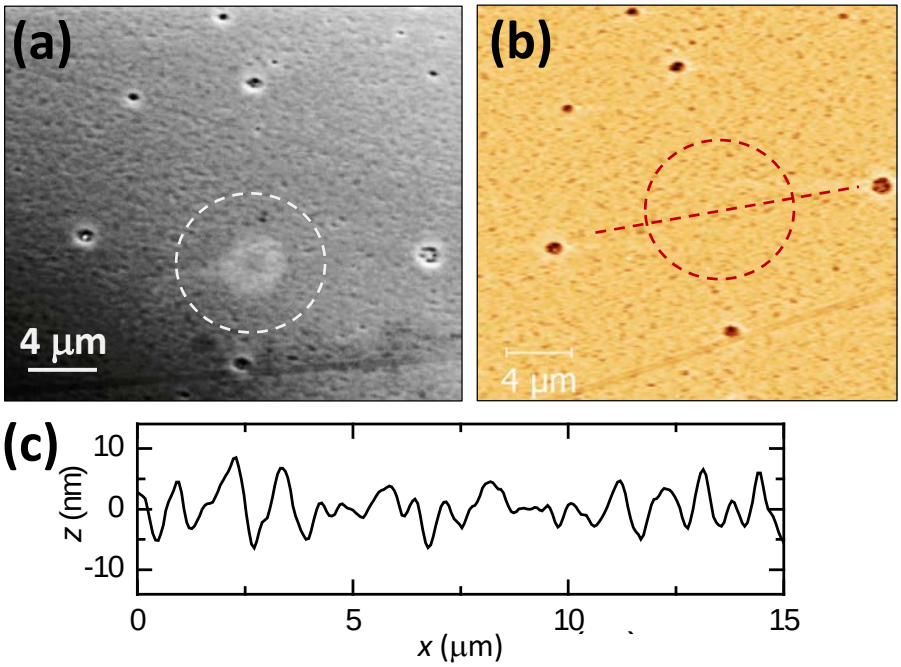


Figure 6.2: **(a)** SEM image of a region annealed with an e-beam (exposure: V_{acc} = 20 kV, I = 28 nA, τ = 5 min). **(b)** AFM image of the region around the e-beam annealed spot. **(c)** AFM *z*-profile acquired along the straight dashed line in (b).

6.2 Mapping the H-distribution by Raman spectroscopy

A further insight into the e-beam induced modification of the electron density of In(AsN):H can be obtained by the correlation between the SEM image (Figure 6.3a) and the spatial map of the intensity of the plasmonic L_b^+ mode (Figure 6.3b) around an annealed spot. The spot was annealed with an impinging current I = 45 nA and exposure time τ = 15 min. The colour map of the intensity of the L_b^+ mode (Figure 6.3b) was acquired using a laser of wavelength λ =532 nm, power P = 1 mW and acquisition time τ = 20 s. Figure 6.3c shows representative Raman spectra of the L_b^+ peak acquired at the positions indicated by the numbers in Figure 6.3b. The contrast from the SEM image (Figure 6.3a) shows a dark region around the brighter annealed spot. This dark ring corresponds to the red area of the colour map in Figure 6.3b, *i.e.* regions of high

intensity of the L_b^+ mode, around a minimum at the centre of the spot (blue area). This is confirmed by inspection of the spectra in Figure 6.3c, from which both a blue shift in the L_b^+ peak position and an increase of the L_b^+ intensity can be observed moving from the centre to the boundaries of the annealed spot.

Figure 6.3d shows the profile of the integrated intensity of the L_b^+ mode around the e-beam annealed spot. Three different regions can be identified: the

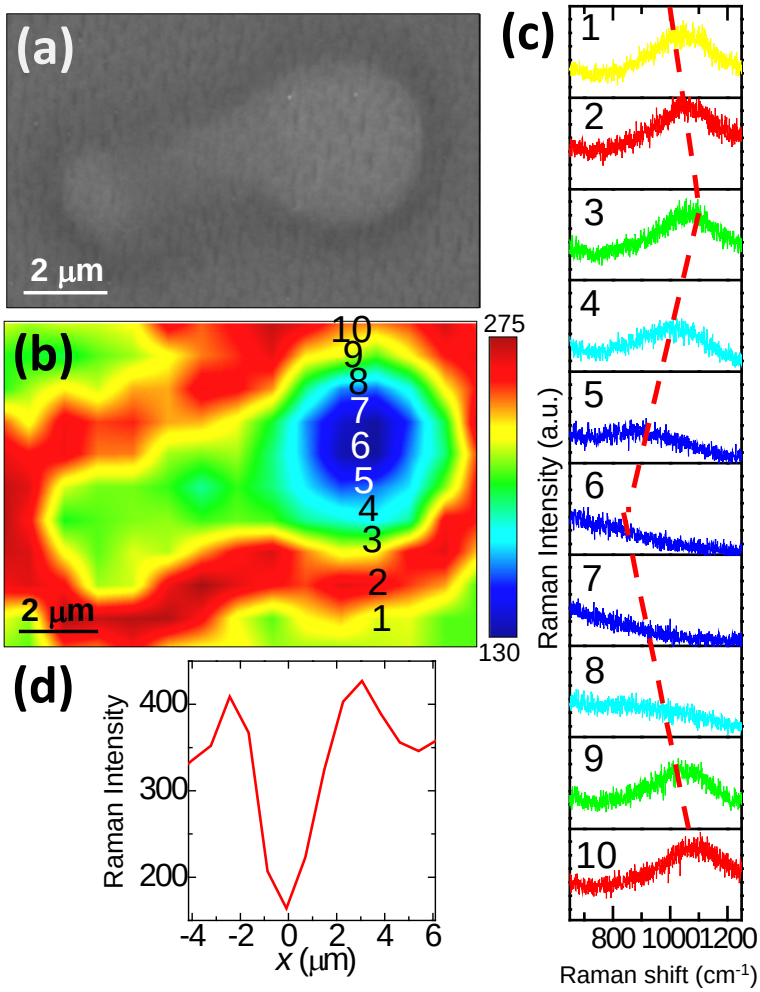


Figure 6.3: **(a)** SEM image of a spot annealed with an e-beam (exposure: V_{acc} = 20 kV, I = 45 nA, τ = 15 min). **(b)** Colour map of the L_b^+ Raman mode intensity. **(c)** Representative Raman spectra acquired at the positions indicated by the numbers in (b). **(d)** Spatial profile of the integrated intensity of the L_b^+ mode across the e-beam annealed spot.

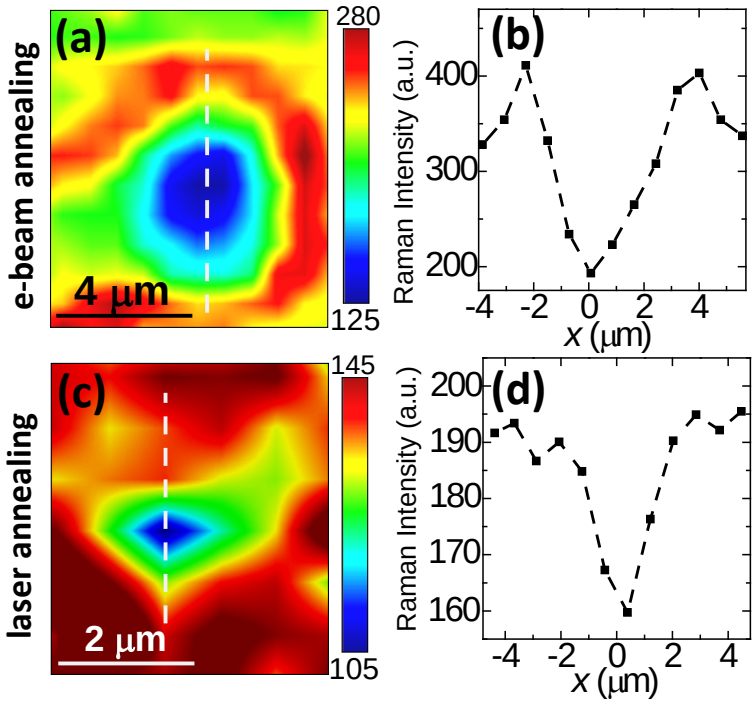


Figure 6.4: Top: colour map **(a)** and spatial profile **(b)** of the integrated intensity of the L_b^+ Raman mode for an electron annealed spot. Bottom: colour map **(c)** and spatial profile **(d)** of the integrated intensity of the L_b^+ Raman mode for a laser annealed spot.

centre of the annealed spot (corresponding to a minimum in intensity), the boundaries of the spot (corresponding to two maxima in intensity), and the non-annealed area. This profile suggests that following the dissociation of the N-H complex, the H-atoms tend to accumulate around the annealed spot. This non-uniform increase of the L_b^+ intensity around the annealed spot differs from what observed by laser annealing. For comparison, Figure 6.4 shows the colour map and the spatial profile of the L_b^+ intensity for an electron (Figures 6.4a-b) and a laser (Figures 6.4c-d) annealed spot. In the case of laser annealing, the L_b^+ intensity profile (Figure 6.4d) does not reveal any maxima around the annealed spot, contrary to what observed for the e-beam annealed spot (Figure 6.4b). Our

data show different spatial profiles of the plasmonic L_b^+ mode following an e-beam and laser annealing, suggesting a different interaction of electrons and photons with the N-H complex.

6.3 Temperature-dependent electron annealing studies

To evaluate the contribution of thermal effects to the dissociation of the N-H donor complex and/or on the H-diffusion in the lattice, the In(AsN):H samples were e-beam annealed at different temperatures: T = 25 °C (Figure 6.5),

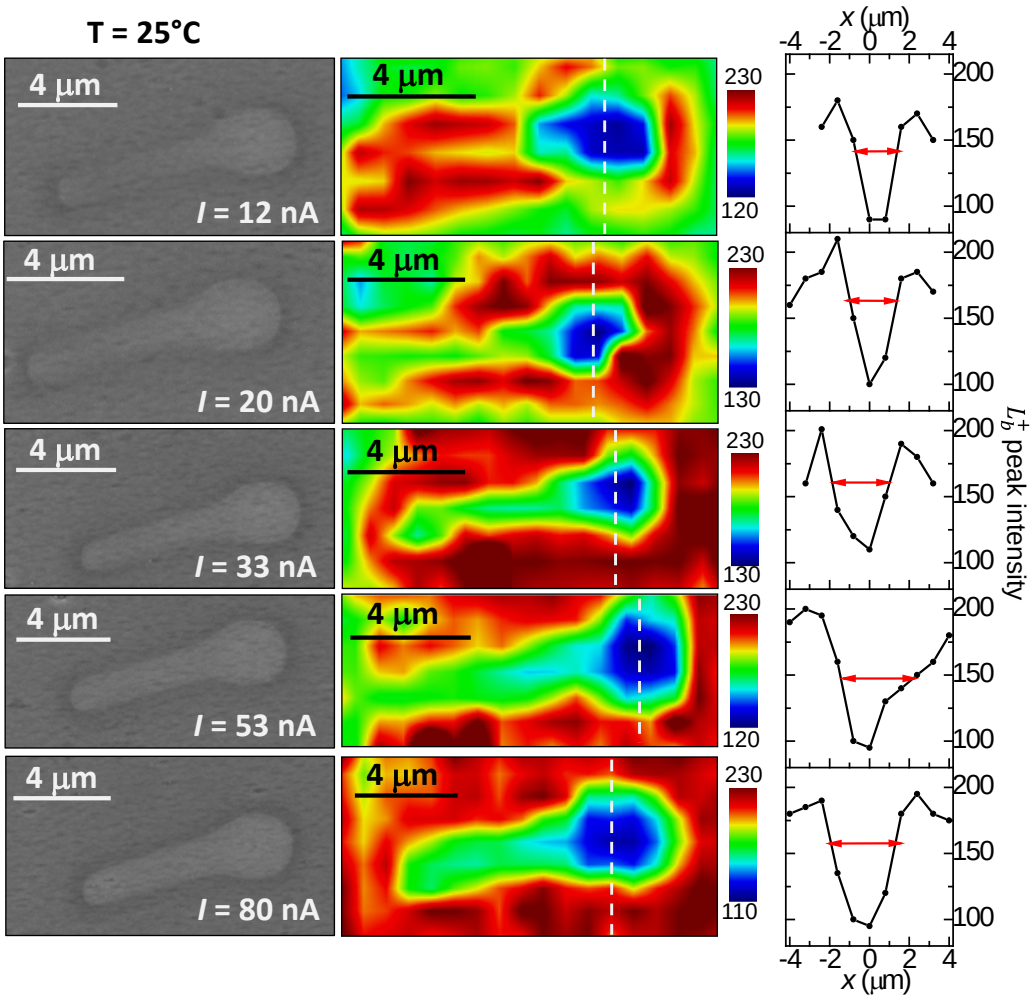


Figure 6.5: Left: SEM images of spots annealed at T = 25 °C with an exposure time τ = 15 min and current I = 12, 20, 33, 53, 80 nA. Right: colour maps and spatial profile of the intensity of the L_b^+ Raman mode acquired along the white dashed lines.

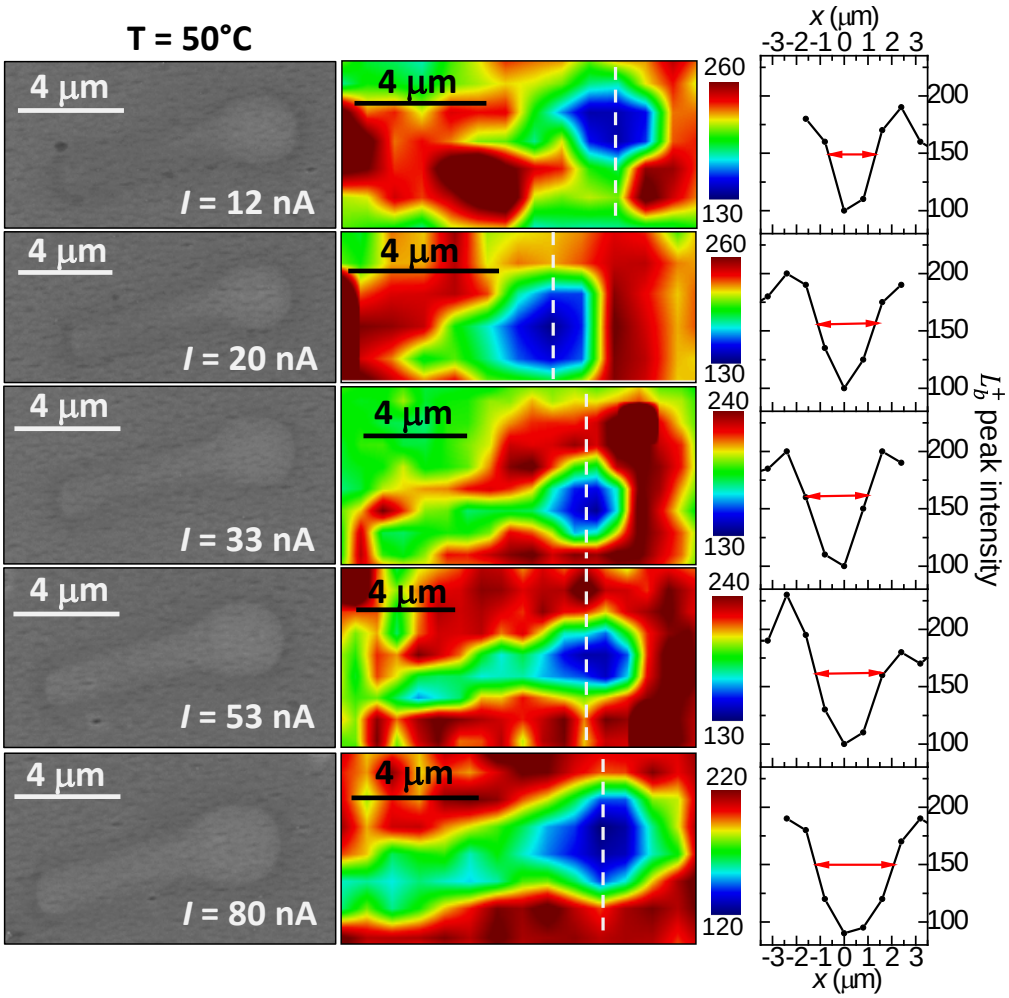


Figure 6.6: Left: SEM images of spots annealed at T = 50 °C with an exposure time τ = 15 min and current I = 12, 20, 33, 53, 80 nA. Right: colour maps and spatial profile of the intensity of the L_b^+ Raman mode acquired along the white dashed lines.

50 °C (Figure 6.6), 100 °C (Figure 6.7) and 150 °C (Figure 6.8). The left panels in Figures 6.5-6.8 show the SEM images of the annealed spots; the right panels show the colour maps of the L_b^+ Raman intensity and the corresponding intensity profile of the L_b^+ mode along the white dashed lines in the colour maps. The exposures were performed at different impinging electron currents I = 12, 20, 33, 53, 80 nA, as indicated in the SEM images. At a given temperature, the

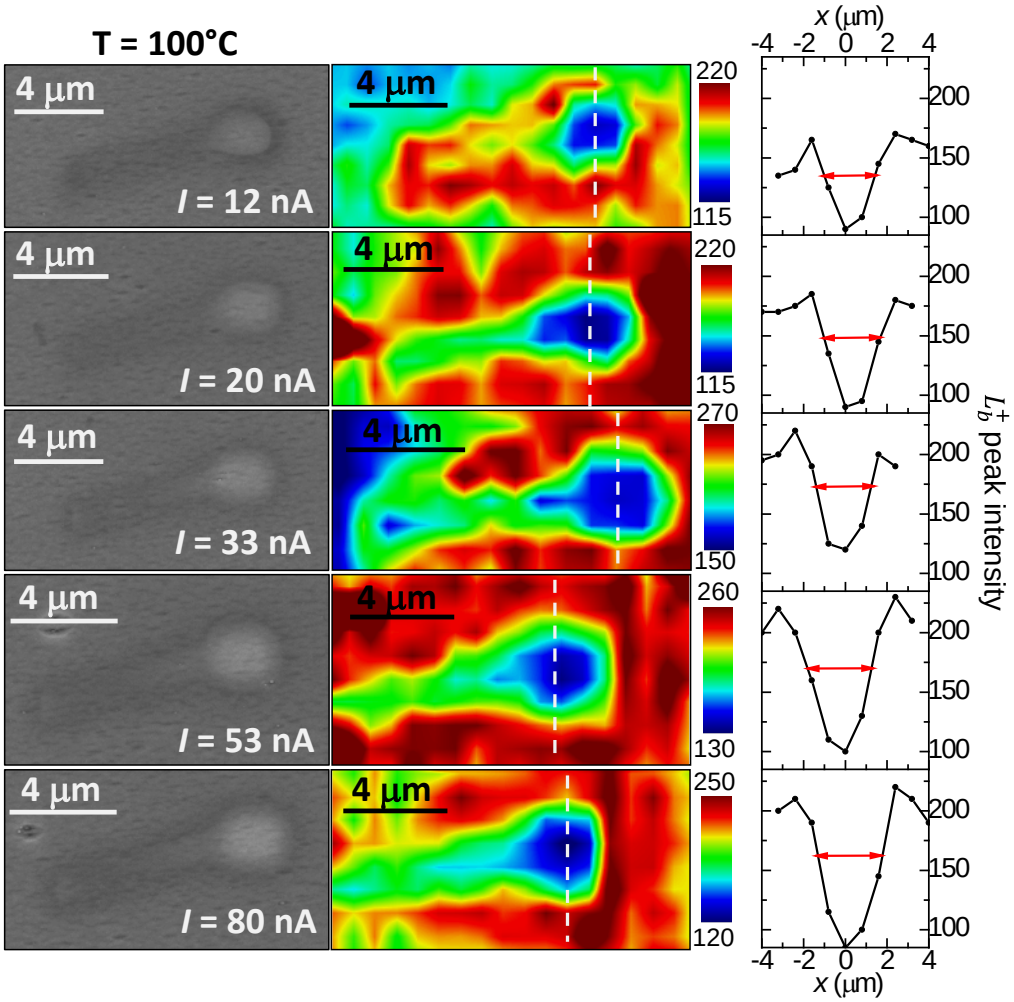


Figure 6.7: Left: SEM images of spots annealed at T = 100 °C with an exposure time τ = 15 min and current I = 12, 20, 33, 53, 80 nA. Right: colour maps and spatial profile of the intensity of the L_b^+ Raman mode acquired along the white dashed lines.

region of the intensity minimum tends to broaden with increasing current. This broadening is due to the increasing e-beam spot size. The contrast between the bright spot and the boundaries in the SEM images also increases with increasing values of I. This is consistent with an increased dissociation of the N-H complex at larger fluxes of impinging electrons. Correspondingly, the minimum in the L_b^+ intensity profile tends to become more pronounced.

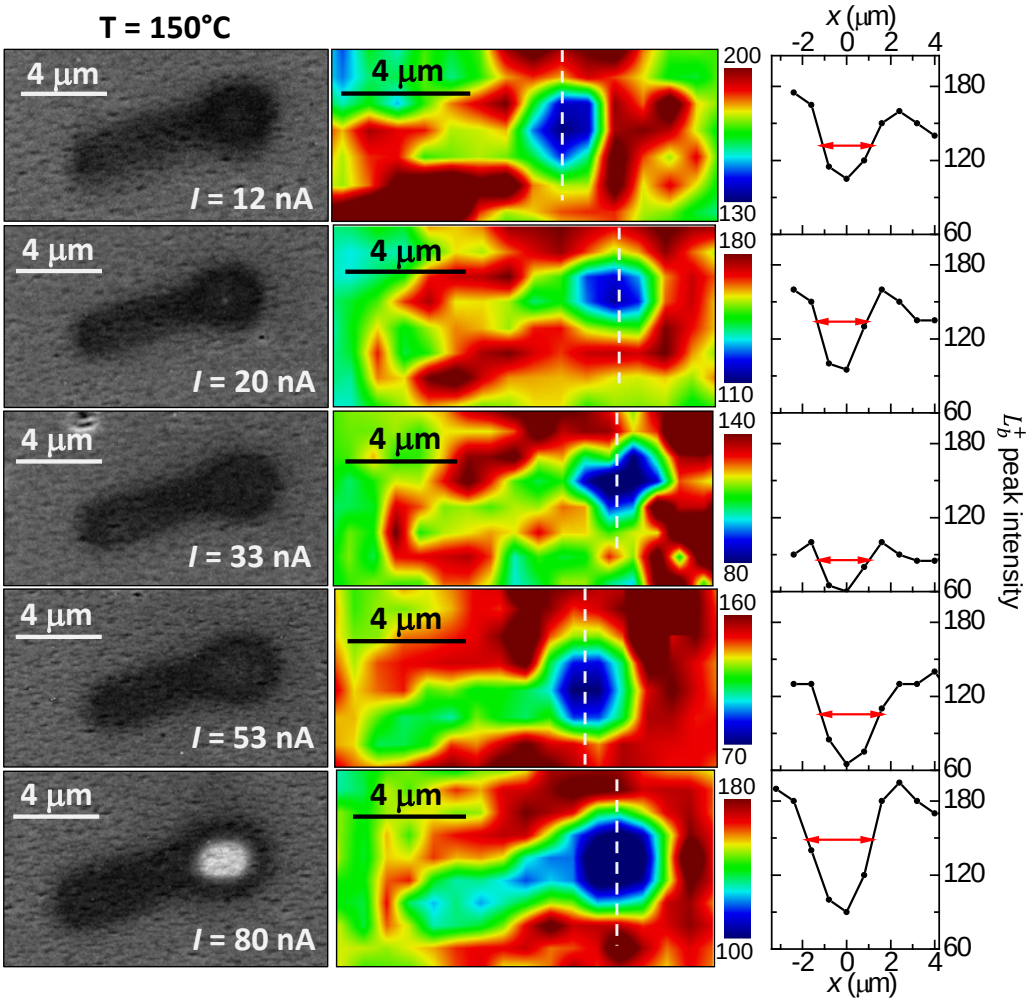


Figure 6.8: Left: SEM images of spots annealed at T = 150 °C with an exposure time τ = 15 min and current I = 12, 20, 33, 53, 80 nA. Right: colour maps and spatial profile of the intensity of the L_b^+ Raman mode acquired along the white dashed lines.

The SEM images show that the contrast between the annealed spot and the boundaries becomes more blurred with increasing T from 25 °C (Figure 6.5) to 100 °C (Figure 6.7). This suggests that a better uniformity in the H-distribution can be achieved at higher T. At the highest temperature (T = 150 °C, Figure 6.8), the annealed region looks more uniform and overall darker. Notably, the contrast between the annealed spot and the boundaries shows a

significant increase for the highest values of current, I = 80 nA, and temperature, T = 150 °C (lowest panel in Figure 6.8). Note that the highest temperature reached in this experiment (T = 150 °C) is very close to that estimated on the sample surface for the laser annealing (see Section 5.4 and Appendix B).

6.4 Summary

In summary, we have investigated an alternative approach to the dissociation of the N-H complex in the highly doped In(AsN):H compound by e-beam annealing. The exposure of In(AsN):H to a focused electron beam induces a decrease of the electron density, n_e, in the crystal with no visible surface damage. However, a close inspection of the spatial distribution of the plasmonic L_b^+ Raman mode indicates a non-uniform increase of n_e around the annealed spot. This feature suggests that the impinging electron beam may induce an accumulation of hydrogen around the annealed spot. This effect is not observed under laser annealing, which induces a dissociation of the N-H complex and the diffusion of the H-atoms by thermal and photonic effects. Indeed, spots that are e-beam annealed at different temperatures (T = 25-150 °C) suggest that high temperatures are beneficial to achieve a better homogeneity in the spatial distribution of hydrogen and thus for an effective modification of the plasmonic properties of the crystal. It is worth considering the impinging power densities used in the two annealing studies. The conditions used for the laser annealing (powers P ~ 15 mW on a diffraction-limited spot of area A ~ 1 μm^2) correspond to a power density $D_{phot} = P/A$ ~ 10^{10} W/m^2. For the e-beam annealing, the area of the annealed spot is A ~ 10 μm^2, as estimated from the SEM images and the Raman colour maps. For a beam of electrons accelerated

by a voltage V_{acc} = 20 kV and with a current in the range I = 10-80 nA, the power density is $D_{el} = I \times V_{acc}/A \sim 10^7$-$10^8$ W/m^2, much lower than D_{phot}. Note that the two experiments were performed under similar exposure times, τ = 15 min.

These results pave the way to a reproducible and non-destructive route for the local patterning of the electron density of a *post-growth* highly doped semiconductor. It should be noted that in our current studies the spatial resolution of the e-beam annealed spots is limited to a few μm due to the high electron currents (I > 10 nA) required to achieve an effective H-removal from the lattice. However, optimizing the experimental conditions (*i.e.* temperature, exposure time, impinging electron dose and/or accelerating voltage) could enable to achieve similar effects with a smaller beam spot size. The different modification of the electron density upon laser and e-beam annealing also encourages further theoretical studies and models to investigate the formation and dissociation of the N-H complex, and the dynamics of the H-diffusion in the crystal.

Chapter 7

Resonant Zener tunnelling via zero-dimensional states in an In(AsN) diode

This chapter demonstrates a new type of Zener tunnelling in an In(AsN)/(InAl)As resonant tunnelling diode (RTD). The incorporation of nitrogen in the quantum well layer of the RTD creates zero-dimensional (0D) states that are localized on nanometre length-scales. These levels provide intermediate states that act as "stepping stones" for resonant tunnelling of electrons across the diode and give rise to a negative differential resistance (NDR) that is weakly dependent on temperature. We probe the size of the 0D states by magneto-tunnelling spectroscopy (MTS).

The sample layer composition and growth conditions are described in Section 4.1.2. The transport measurements were performed by myself at the University of Nottingham. The experimental setup used for these measurements is described in Section 4.2. These results were published in *Scientific Reports* **6**, 32039 (**2016**)[143].

7.1 Introduction

Interband tunnelling of charge carriers through a forbidden energy gap, known as Zener tunnelling[135], is a phenomenon of fundamental and technological interest. Its experimental observation in the Esaki *p-n* semiconductor diode has led to the first demonstration and exploitation of

quantum tunnelling in a condensed matter system. Zener tunnelling has played a key role in the understanding of quantum phenomena in condensed matter physics and has been investigated in several material systems. Renewed interest in Zener tunnelling has emerged from the research on graphene[180], where relativistic electrons can tunnel through a potential barrier without back scattering, a phenomenon called Klein tunnelling[181]. The quantum tunnelling of carriers through a diode has also lately shown great potential for relevant applications such as random number generation and cryptography[182, 183]. On the other hand, Zener tunnelling via zero dimensional (0D) states remains largely unexplored due to lack of suitable structures and materials for its observation. Here we report on Zener tunnelling involving 0D states formed by the incorporation of N-atoms in the narrow gap semiconductor InAs.

7.2 Negative differential resistance in In(AsN)/(InAl)As RTDs

For these studies, we designed and grew by molecular-beam epitaxy (MBE) a series of In(AsN) RTDs whose schematic band diagram at zero applied bias is shown in Figure 7.1a. Figure 7.1b shows the low temperature (T = 2K) current-voltage, *I-V*, characteristic for the In(AsN)/(InAl)As RTD.

For low applied biases of both polarities, the *I-V* curve exhibits an ohmic region; with increasing forward bias the current rises up to a maximum, *D*, at V ~ 0.06 V, followed by a region of negative differential resistance (NDR), in which the DC current decreases in two well-defined steps. These steps are accompanied by a self-sustained oscillatory current, which arises from the instability of the device circuit induced by the NDR. When the device is connected to an oscilloscope, we observe a significant increase of the RF noise generation at frequencies of ~ kHz in the bias region of the NDR. Closer

inspection of the *I-V* and of the differential conductance, *dI*(*V*)*/dV*, curve also reveals a broad feature, E_1, at $V \sim 0.35$ V (see Inset of Figure 7.1b).

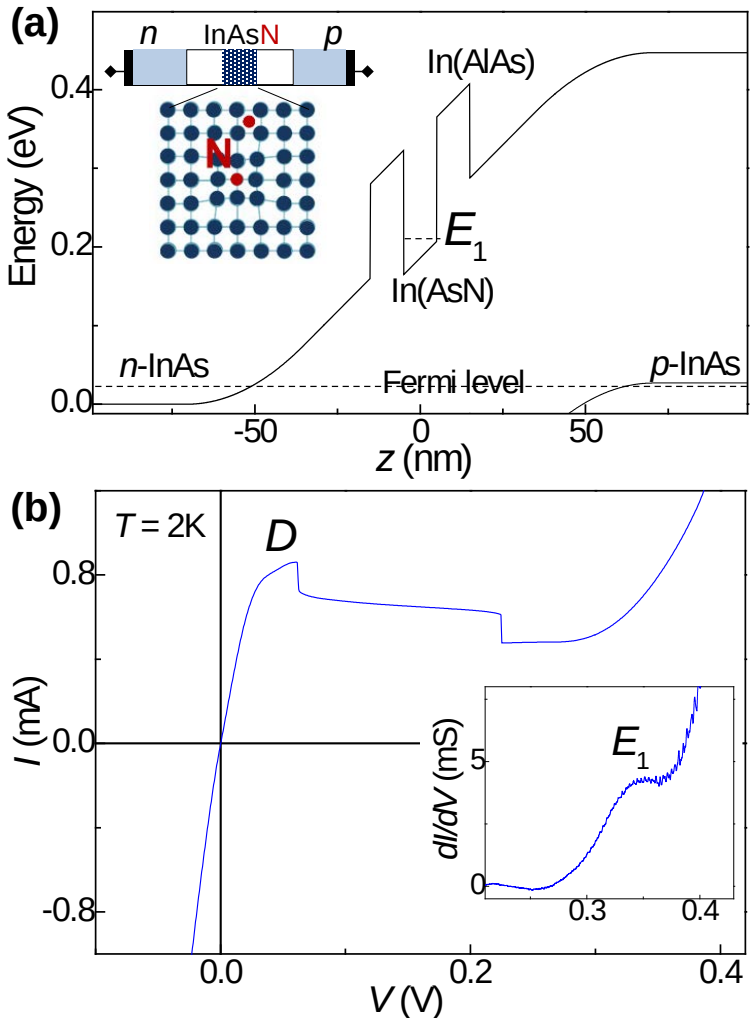


Figure 7.1: (a) Energy band diagram of a *p-i-n* In(AsN)/(InAl)As resonant tunnelling diode (RTD) at thermal equilibrium. The black dotted lines indicate the Fermi energy and the lowest quasi-bound electron state E_1 of the In(AsN) QW. Inset: Sketch of the *p-i-n* diode with the In(AsN) QW in the intrinsic (*i*) layer, and substitutional and interstitial N-atoms in InAs. **(b)** Current-voltage (*I-V*) curve at $T = 2$K for an In(AsN) RTD with mesa diameter $d = 100$ µm showing a strong peak *D*. Inset: d*I*(*V*)/d*V* curve showing a weak resonant feature E_1.

The temperature dependence of the *I-V*s for an In(AsN)/(InAl)As RTD is compared with that for a control sample with no nitrogen (Figure 7.2). The striking difference between the two sets of the *I-V* curves is the absence of the strong peak *D* and of the associated NDR in the control device. This is a clear indication that the occurrence of peak *D* and of the NDR region is strongly correlated to the presence of quantum states associated with the N-atoms. Also, Figure 7.2a shows that peak *D* is weakly affected by temperature over an extended temperature range up to $T \sim 200$K. In contrast, the *I-V* curves of the control sample exhibits a conventional diode-like behaviour (Figure 7.2b).

7.3 Resonant Zener tunnelling through N-induced zero-dimensional states

Since peak *D* occurs at biases ($V \sim 0.06$ V) that are much lower than the built-in potential ($V \sim 0.4$ V) of the diode and is absent in the control device, we exclude the possibility that it arises from tunnelling of charge carriers through the two-dimensional (2D) subband states of the In(AsN) QW, which generates only a weak feature, E_1, at a significantly higher bias, $V \sim 0.35$ V, close to the flat-band voltage (Inset of Figure 7.1b). We propose instead that *D* is due to Zener tunnelling of electrons through the forbidden energy gap between the *n*- and *p*-sides of the diode. Zener tunnelling in conventional diodes can cause a significant current when there is spatial overlap between occupied states in the conduction band (CB) of the *n*-layer and the empty states near the top of the valence band (VB) in the *p*-layer. The strength of the Zener tunnel current is enhanced for the case of a narrow energy band gap, thin barrier width and/or small carrier effective mass[135, 184, 185]. Since the carrier effective masses and

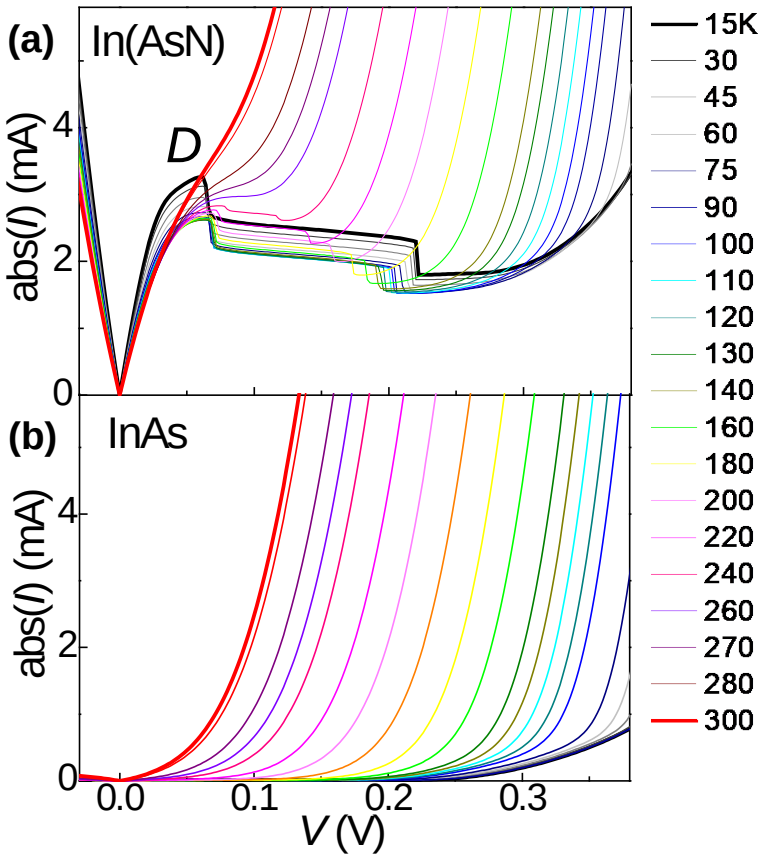


Figure 7.2: Current-voltage (*I*-*V*) characteristics at temperatures *T* from 15K to 300K of In(AsN) **(a)** and InAs **(b)** RTDs with mesa diameter *d* = 200 µm.

band gap energy of InAs and In(AsN) with [N] = 1% are very similar[97], one should expect a relatively weak Zener tunnel current in both devices. The presence of the strong resonance *D* only in the In(AsN) RTD suggests that Zener processes are enhanced by tunnelling processes through N-induced localized states in the energy gap of In(AsN).

The weak *T*-dependence of peak *D* indicates that the N-induced levels are strongly confined, thus providing an effective path for tunnelling of electrons at various *T*. We note instead that for large positive biases ($V > 0.2$ V), the *I*-*V* curves of the InAs and In(AsN) RTDs and their temperature dependence are very similar (Figure 7.2). In this bias regime, thermal diffusion of carriers over

the junction's energy barrier represents the dominant contribution to the current and the *T*-dependence of *I* is well described by a thermally activated behaviour:

$$I \sim \exp(-E_a/k_B T) \tag{7.1}$$

where E_a is an activation energy that depends on the applied bias: E_a decreases with increasing *V*, extrapolating to zero at the flat-band bias, *V* ~ 0.4 V, corresponding to the built-in potential of both diodes (Figure 7.3a). On the other hand, E_a strongly deviates from this trend for the In(AsN) RTD at lower positive biases (*V* < 0.2 V), where it tends to saturate. This suggests that in this bias regime the current is not thermally activated and that the thermal diffusion of

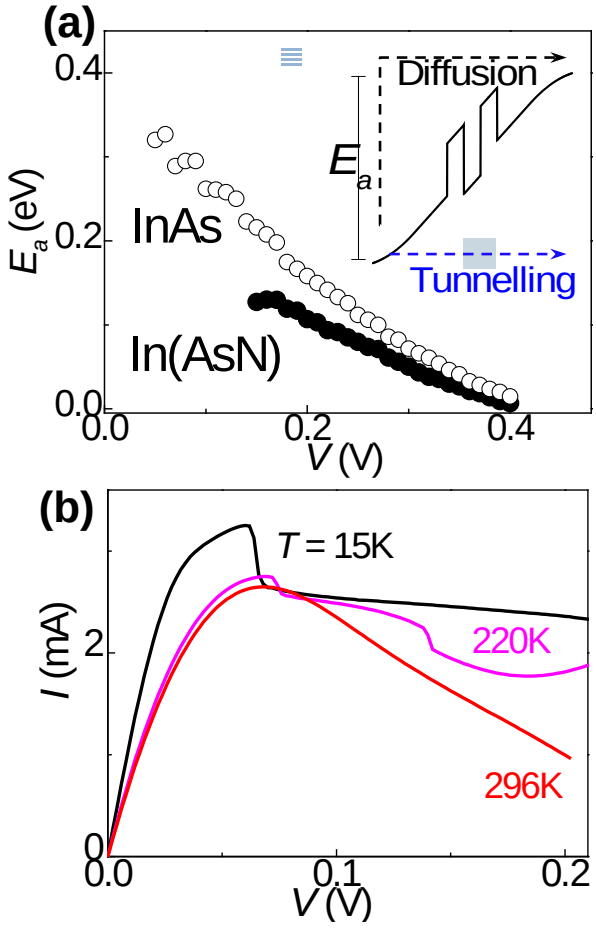


Figure 7.3: (**a)** Bias dependence of the activation energy E_a describing the dependence of the current *I* on temperature, *i.e.* $I \sim \exp(-E_a/k_B T)$. Inset: sketch of electron diffusion and tunnelling. (**b)** *I*-*V* characteristics of the In(AsN) RTD at *T* = 15K, 220K and 296K after subtraction of the diffusion current.

carriers competes with the tunnelling of carriers through the band gap assisted by N-induced levels (Inset of Figure 7.3a). Figure 7.3b shows representative *I-V*s for the In(AsN) RTD after subtraction of the contribution of diffusion current, as measured in the device without nitrogen: peak *D* and the NDR are only weakly affected by *T* and can be clearly seen up to room temperature, as expected for electrons tunnelling into strongly localized 0D states.

7.4 Magneto-tunnelling spectroscopy of zero-dimensional states

Here we exploit the effect of magnetic fields on the tunnelling of electrons from the *n*- to the *p*- side of the RTD to probe the size of strongly localized 0D states arising from the N-incorporation in the QW layer. The resonant transmission of electrons through N-induced localized states is qualitatively different from Zener tunnelling of electrons in GaAs/AlAs QW *p-i-n* RTDs, where quasi-localized electric-field dependent states in the QW modulate the Zener current under an applied reverse bias[186], and from Zener tunnelling via the gate-induced localized states of narrow-gap double-quantum-wire structures[187]. Other sensitive techniques such as scanning tunnelling microscopy (STM)[144] can be used to probe the spatial form and size of the wave function of a 0D state. However, STM is an invasive and destructive technique mostly suitable for 0D states on a surface.

In our case, in order to study localized states below a surface incorporated in a real semiconductor, we exploit magneto-tunnelling spectroscopy (MTS)[145-147]. As explained in further detail in Section 3.1.2, this technique exploits the effect of the classical Lorentz force on the motion of an electron: when an electron tunnels from the emitter into the 0D state, it acquires an additional in-plane momentum given by $\hbar\Delta k_y = -eB_x s$, where s is the tunnelling distance

along the tunnelling direction z from the emitter to the localized 0D state and B_x is the magnetic field applied perpendicular to z (Inset of Figure 7.4a). The variation of the tunnel current with $B_x \propto \Delta k_y$ is determined by the size of the matrix element that governs the quantum transition of an electron as it tunnels

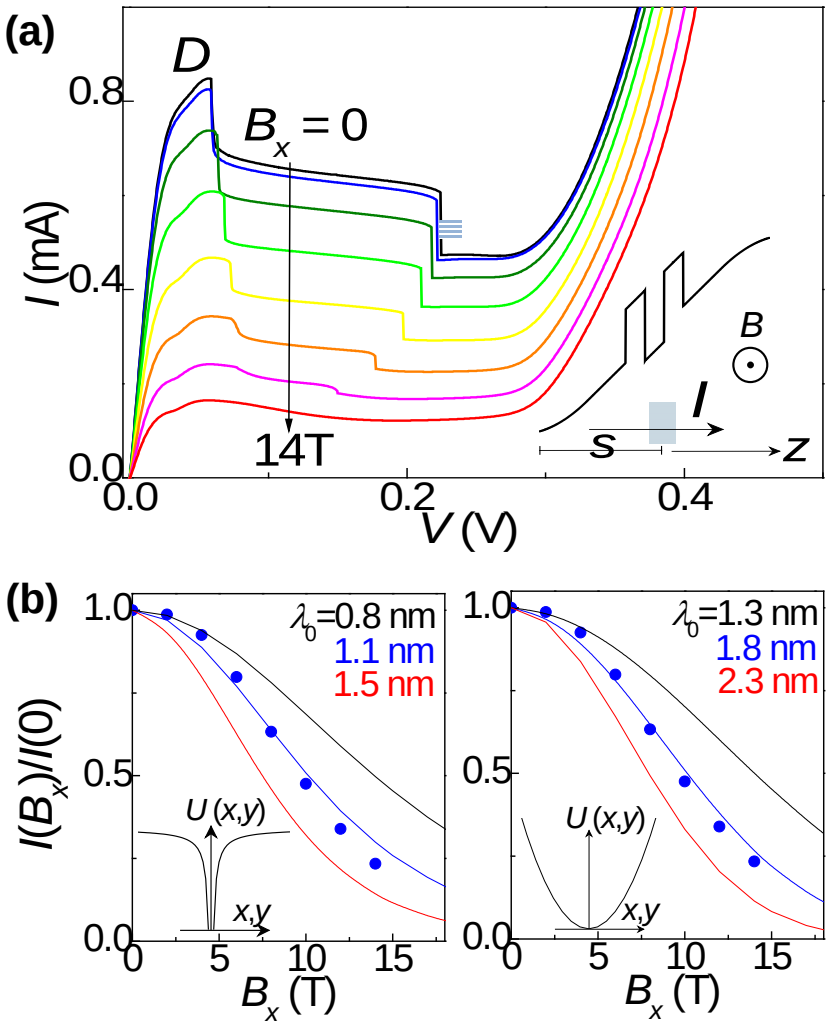


Figure 7.4: (**a**) Current-voltage (*I*-*V*) curves at magnetic fields B_x = 0, 2, 4, 6, 8, 10, 12, 14 T, applied perpendicular to the direction z of the current for an In(AsN) RTD with mesa diameter d = 100 μm (T = 2K). **(b)** Measured (dots) and calculated (lines) dependence of the normalized current $I(B_x)/I(0)$. The model shown in the two panels is for a Coulomb (left) and an harmonic (right) potential $U(x, y)$. In each panel, different curves correspond to different sizes λ_0 of the electronic wave function.

into the 0D state and hence probes the electron probability density in Fourier space of the localized state[147].Figure 7.4a shows the B_x-dependence of the *I*-*V* curve: with increasing B_x, the intensity of peak *D* displays a marked decrease, stronger than that observed at high voltages ($V > 0.2$ V). Figure 7.4b compares the measured B_x-dependence of the peak current height of feature *D* (blue dots) with that calculated (solid lines) using a transfer Hamiltonian model of resonant tunnelling through a localized state for two different forms of the confining potential (Insets of Figure 7.4b). In our model, we assume separability of the 0D wave function into in-plane (*xy*) and normal (*z*) components, and express the normalized tunnel current, $I(B_x)/I(0)$, as $|M(B_x)/M(0)|^2$, where $M(B_x)$ and $M(0)$ are the overlap integrals in the *xy*-plane of the emitter and the N-induced localized states for $B_x > 0$ and $B_x = 0$, respectively. The calculated and measured magnetic field dependencies differ from those expected for Zener tunnelling between extended states in magnetic field[188] and are discussed in the following section.

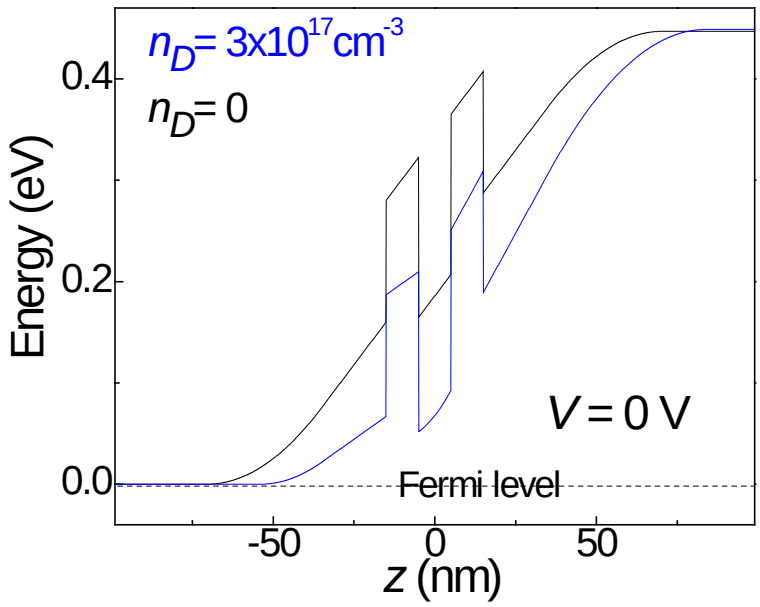


Figure 7.5: Calculated profile of the CB edge at applied biases $V = 0$ V for a donor states density $n_D \sim 3\times10^{17}$ cm^{-3} (blue line) and $n_D \sim 0$ (black line).

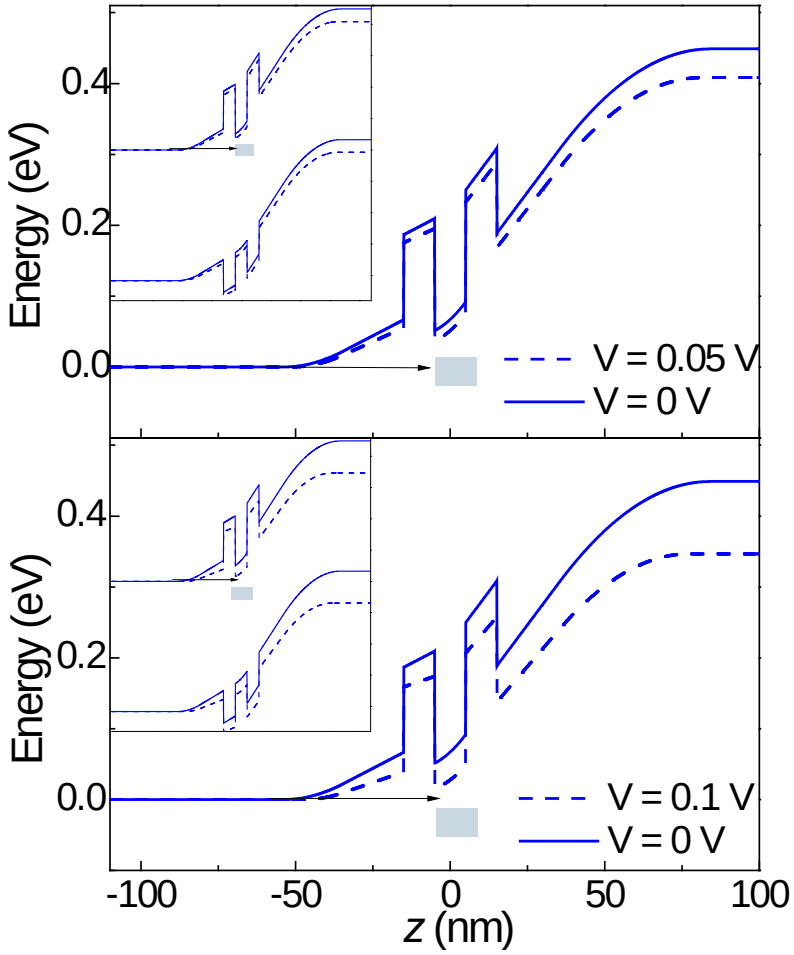


Figure 7.6: Calculated profile of the CB edge at applied biases V = 0 V (solid line) and V = 0.05 V, 0.1 V (dashed lines). The arrow sketches tunnelling of electrons from the *n*-emitter layer into localized states of the In(AsN) layer (shaded rectangle). Insets: profile of both the CB and VB edges under the same bias conditions illustrated in the main panels.

We model the energy band diagram of the RTD by solving Schrödinger's and Poisson's equations. The N-incorporation in the well leads to a lowering of the energy of the quasi-2D ground state subband of the QW by ~ 30 meV compared to InAs. Also, nitrogen introduces donor states with density n_D ~ 3×10^{17} cm^{-3} for [N] ~ 1%, as measured from Hall studies of In(AsN) epilayers[172]. Figure 7.5 shows the CB potential profile of the RTD at thermal

equilibrium for a concentration of ionized donors $n_D = 3\times10^{17}$ cm^{-3} in the QW, which create a non-uniform electric field compared to $n_D = 0$.

When a small voltage, *V*, is applied (Figure 7.6, top panel), resonant tunnelling through a particular N-related energy state in the gap of In(AsN) should lead to a resonance in the *I-V*, whenever a filled state in the negatively biased electron emitter *n*-layer is resonant with an adjacent empty localized N-related state in the In(AsN) layer. Since these states may be located at different positions in the well, we can expect a distribution of energy levels and/or tunnelling distances, and correspondingly a broadened resonance. In the measured *I-V*, we do not observe any resonant feature, but a current that is significant larger than that of a control sample with no nitrogen.

For sufficiently high bias voltages, no states are available for electron tunnelling (Figure 7.6, bottom panel) and the current decreases, thus leading to NDR in the *I-V*. From the band profile in Figure 7.6 and the measured *I-V* curve, we estimate that the 0D states lie at an energy $E > 40$ meV below the CB minimum of In(AsN). This is significantly larger than the binding energy for a shallow donor in InAs ($E_0 \approx 1.6$ meV) and is consistent with the weak dependence on temperature of peak *D*.

To model the B_x-dependence of the peak *D* (Figure 7.4), we examine different forms of the confinement potential:

- for a Coulomb potential of the form $U(x,y) = -e^2/(4\pi\gamma\varepsilon_0\varepsilon_r\rho)$, where ε_r is the relative permittivity, $\rho = \sqrt{x^2+y^2}$, and γ is an empirical parameter describing the effect of the QW potential on the donor, the electron wave function in the *xy*-plane is described by $\psi(x,y) \sim e^{-\rho/\lambda_0}$, where λ_0 is an effective Bohr radius[189];

- a confining potential can also be induced in the QW by a small number of closely spaced electrical charges[190] or a variation in the N-composition. Since such a potential is approximately parabolic close to its minimum, its ground state is a simple harmonic wave function. Thus for a parabolic potential $U(x,y) = m_e^*\omega^2\rho^2/2$, where m_e^* is the electron effective mass and ω is the angular frequency of the harmonic oscillator, the wave function in the *xy*-plane is given by $\psi(x,y) \sim e^{-\rho^2/2\lambda_0^2}$, where $\lambda_0 = \sqrt{\hbar/m_e^*\omega}$.

For the Coulomb and parabolic potentials, respectively, we express the B_x-dependence of the normalized tunnel current as[147, 189]:

$$\frac{I(B_x)}{I(0)} = \frac{|M(B_x)|^2}{|M(0)|^2} = \frac{1}{[1+(B_x/\tilde{B})^2]^3} \quad , \tag{7.2}$$

and

$$\frac{I(B_x)}{I(0)} = \frac{|M(B_x)|^2}{|M(0)|^2} = \exp(-\frac{B_x^2}{\tilde{B}^2}) \, , \tag{7.3}$$

where $\tilde{B} = \hbar/es\lambda_0$, s is the average tunnel length from the emitter to the bound state. From the calculated band energy profiles, we estimate *s* ~ 30 nm for *V* = 0.05 V.

As shown in Figure 7.4b, the calculated $I(B_x)$ curves reproduce accurately the data if we take λ_0 = (1.1 ± 0.1) nm for the Coulomb potential and λ_0 = (1.8 ± 0.1) nm for the harmonic potential. Although we cannot establish the specific form of the wave function, we can conclude that the N-induced states responsible for peak *D* are strongly confined. Using a 3D (2D) hydrogenic model, the value of λ_0 gives an *effective* Rydberg energy E_0 = 30 meV (120 meV). Our estimate of the spatial extent of the defect is also consistent with the evanescent wave model of a defect state in the energy gap. For a state at an energy of E_0 below the conduction band minimum, $\psi(x,y) \sim e^{-\kappa\rho}$, with $\kappa =$

$\sqrt{2m_e^* E_0}/\hbar$. Using $m_e^* = 0.026\ m_0$ and $E_0 > 40$ meV, as obtained from the voltage position of peak *D* and the energy band diagram of Figure 7.6, we derive a typical length $\kappa^{-1} < 5.9$ nm.

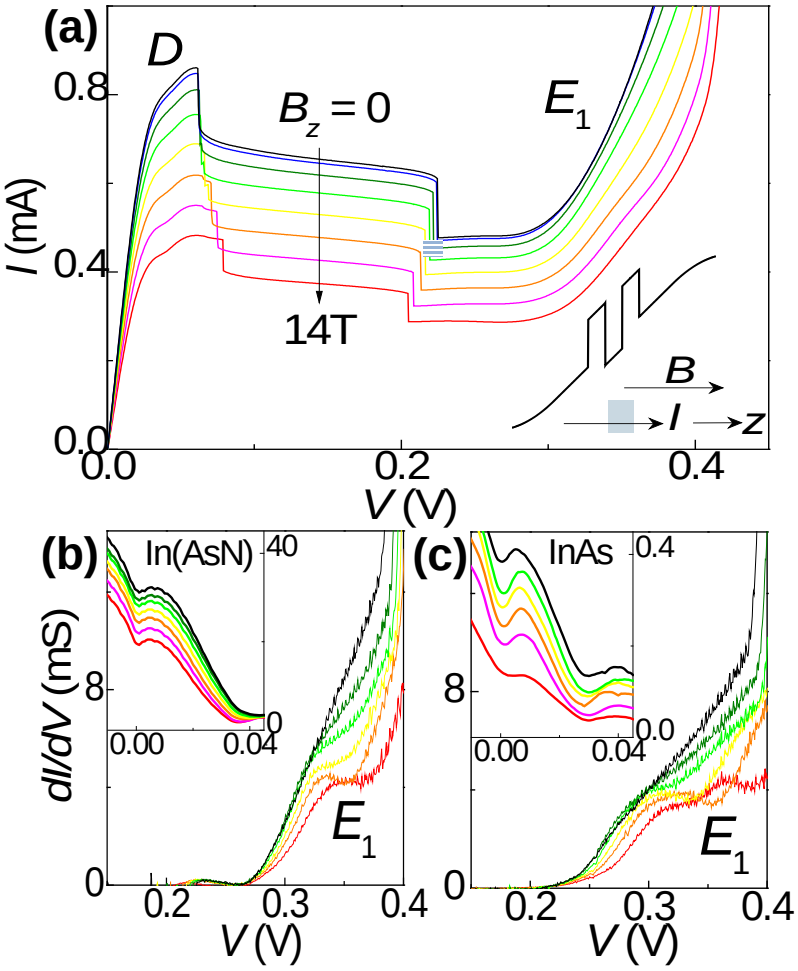


Figure 7.7: (a) Current-voltage (*I-V*) curves at magnetic fields B_z = 0, 2, 4, 6, 8, 10, 12, 14 T, applied parallel to the direction *z* of the current for an In(AsN) RTD with mesa diameter *d* = 100 μm (*T* = 2K). (**b-c)** Differential conductance *dI*(*V*)*/dV* curves versus B_z in the bias region of electron tunnelling into the first subband, E_1, of the In(AsN) (b) and InAs (c) QW for B_z =0, 4, 6, 8, 10, and 14 T. The insets show the *dI*(*V*)*/dV* curves at small applied biases (*T* = 2K).

As shown in Figure 7.7a, a magnetic field applied parallel to the direction of current (B_z) has instead only a weak effect on peak *D*. The weaker effect on Zener tunnelling can be understood considering that for this orientation of *B* up to 14T, the magnetic confinement length in the plane of the QW, $l_z = (\hbar/eB_z)^{1/2}$, is always larger than λ_0: for B_z = 14T, l_z = 6.8 nm > λ_0. Thus the N-localized states are not greatly modified by the confining potential of the magnetic field; also, they have a weak effect on the tunnelling of electrons into the QW subbands (see feature E_1 in the *dI*(*V*)/d*V* curve in Figure 7.6b). Tunnelling of electrons into the lowest Landau level (LL) of the first QW subband (*n* = 1) produces a small diamagnetic shift of E_1 with increasing B_z, as is also observed in the control sample (Figure 7.7c). A modulation of the *dI(V)/dV* curve due to tunnelling of electrons into the first two LLs can also be seen in the control sample, where E_1 splits into distinct features at B_z > 10 T. Finally, closer inspection of the *dI/dV* curves reveals a series of weak, but sharp resonant features at *V* = 0 V and 0.03 V (inset of Figures 7.7b-c). These are observed in all RTDs (with and without nitrogen) and are assigned to tunnelling of electrons from the *n*- to the *p*-sides of the diode without and with the emission of longitudinal optical (LO) phonons, which have energy $\hbar\omega_{LO}$ = 29 meV in InAs.

The effects of the incorporation of N on the electronic band structure of several III-Vs has been examined extensively in earlier work[15, 16, 99, 191, 192]. The majority of these studies has focused on wider band gap (InGa)(AsN) compounds, where the incorporation of N leads not only to isolated substitutional N-atoms but also to the formation of N-N pairs, where a group III atom has two N nearest neighbours, and of higher-order N-clusters with energies

below and above the CB minimum. In the narrow band gap alloy In(AsN), the same clusters are expected to lie well-above the CB edge[99] and thus they cannot be responsible for the localized energy levels in the band gap that we have identified in our tunnelling experiments.

On the other hand, non-substitutional N-related crystal defects are known to form in dilute nitrides[191-193], including In(AsN)[102]. For our In(AsN) layers, we have conducted high-resolution x-ray diffraction (HRXRD) studies to evaluate the N-composition and crystal quality. The HRXRD studies were compared with time-of-flight secondary ion mass spectroscopy (ToF-SIMS) to assess the purity of the layers and the total amount of N. The N-content obtained by ToF-SIMS was found to be higher (by about 5%) than that derived from the analysis by Vegard's law of the HRXRD data and that difference increases with increasing N-content[102]. This behaviour, which was also observed in the dilute nitride Ga(AsN) alloy[193], suggests the incorporation of non-substitutional N into the crystal lattice, such as N–As split interstitials, N-antisites, and interstitial N. The identification of the specific crystal defects and the modelling of their energy levels require further investigation.

7.5 Summary

In summary, we have presented the first experimental study of a Zener tunnel diode based on the MIR alloy In(AsN). The *I*-*V* characteristics at low *T* show an extended region of NDR as well as an ohmic behaviour around zero bias that we attribute to Zener tunnelling of electrons from the *n*- to the *p*-side of the diode, assisted by N-induced levels. The weak temperature dependence of the NDR over an extended temperature range indicates that the levels are strongly confined in the In(AsN) QW layer. Magneto-tunnelling spectroscopy

demonstrates that these levels are localized over a characteristic length $\lambda_0 \sim 1.5$ nm and lie below the CB minimum of In(AsN).

The presence of N-related defects is known to be the main cause of deterioration of both optical and electrical properties of wider band gap dilute nitrides. For the narrow band gap In(AsN) alloy, although disorder effects tend to be significantly weaker due to the different energy position of the N-N pairs and N-clusters, the incorporation of nitrogen is still accompanied by the creation of localized states in the energy gap. Tunnelling of carriers into these states could increase leakage currents and noise levels in optical and electrical devices, such as MIR LEDs and photodetectors. Our RTD structures allow us to sensitively probe such states; also, electron tunnelling through these states give rise to NDR that is only weakly affected by temperature, thus offering potential applications for non-linear components in electronics and MIR photonics.

Chapter 8

Electroluminescence studies of In(AsN) resonant tunnelling diodes

This chapter describes electroluminescence (EL) spectroscopy studies of In(AsN)/(InAl)As RTDs under different applied voltages and temperatures. We report on a bias-tuneable EL signal in the wavelength range λ = 3-5 μm at low temperatures (T = 6-50 K). This involves tunnelling of electrically injected carriers into the extended and localized states of the In(AsN) QW, followed by carrier recombination. We also report on up-conversion luminescence (UCL) over a large range of temperatures (T = 77-300 K) and applied voltages.

The transport EL measurements were performed by myself at Lancaster University. The sample layer composition and growth conditions are described in Section 4.1.2. The experimental setup is described in Section 4.3.3. These results are in preparation for a journal publication.

8.1 Electroluminescence (EL) of In(AsN)/(InAl)As RTDs

Figure 8.1 shows the EL spectra of an In(AsN)/(InAl)As RTD with mesa diameter d = 800 μm acquired at different applied biases, V, and at temperatures T = 6-100 K. To follow the evolution of the EL peak under a varying V, we also plot in Figure 8.2 the colour maps of the normalized EL intensity as a function of photon energy, $h\nu$, and applied voltage, V. Similar plots are shown in Figure

8.3 (EL spectra) and Figure 8.4 (normalized EL colour maps) for T = 120-300 K. In these Figures, the drop in EL intensity around $h\nu = 0.29$ eV is due to CO_2-absorption.

From the EL spectra and colour maps, we envisage three different temperature regimes:

- At low temperatures (T = 6-50 K) (Figure 8.1 and 8.2) and $V > 0.40$ V the EL spectra show two close peaks at energies $h\nu \sim 0.375$ eV (peak I) and $h\nu \sim 0.395$ eV (peak II). Their energy position is weakly dependent on the applied voltage for $V > 0.40$ V. We note that both these energies are smaller than the energy of the electron-hole recombination from the electron and hole ground states in the QW ($h\nu_X \sim 0.43$ eV). We thus attribute these features to the recombination of carriers from dopant impurities in the QW. We describe further this point in Section 8.2.

On the other hand, for $V < 0.40$ V, the main EL emission (peak I) has a strong dependence on the applied bias and shifts towards lower energies with decreasing V towards a broad band centred at $h\nu \sim 0.32$ eV (peak III). The strong bias-dependence and the broad III-emission suggest carrier recombination from defect states and that in this bias regime the emission of the RTD depends on the alignment of the emitter and/or collector states with defects states in the band gap, such as the 0D N-related states presented in Chapter 7. We also note that peak III occurs at energies $h\nu$ between $h\nu = eV - \hbar\omega_{LO}$ and $h\nu = eV - 2\hbar\omega_{LO}$, where $\hbar\omega_{LO}$= 29 meV is the longitudinal optical (LO) phonon energy of InAs. Thus we attribute this low-bias EL peak to the recombination of injected carriers from N-related defect states following the emission of one or two LO phonons.

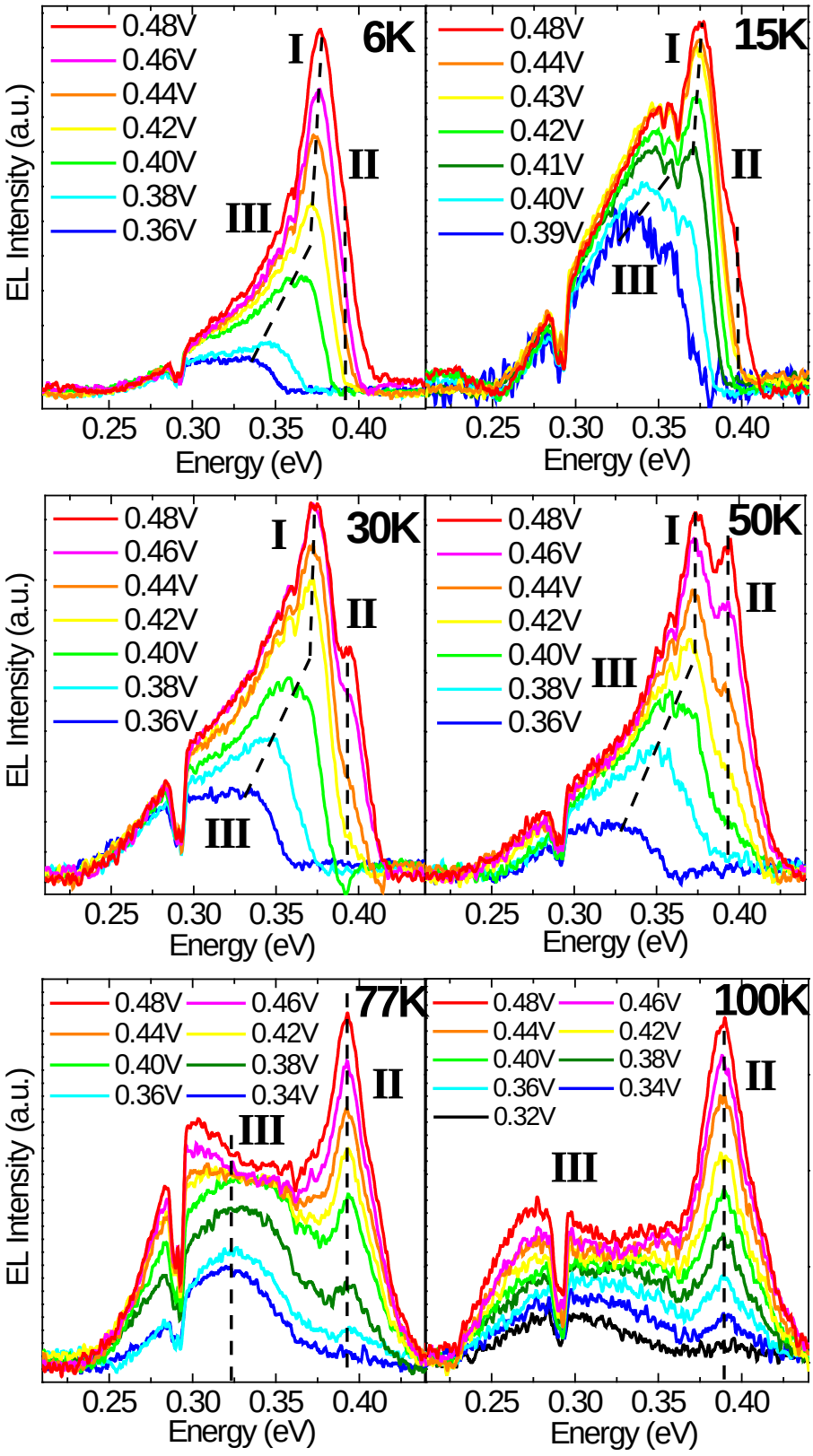


Figure 8.1: EL spectra of an In(AsN)/(InAl)As resonant tunnelling diode (RTD) at different applied biases and at temperatures T = 6-100 K.

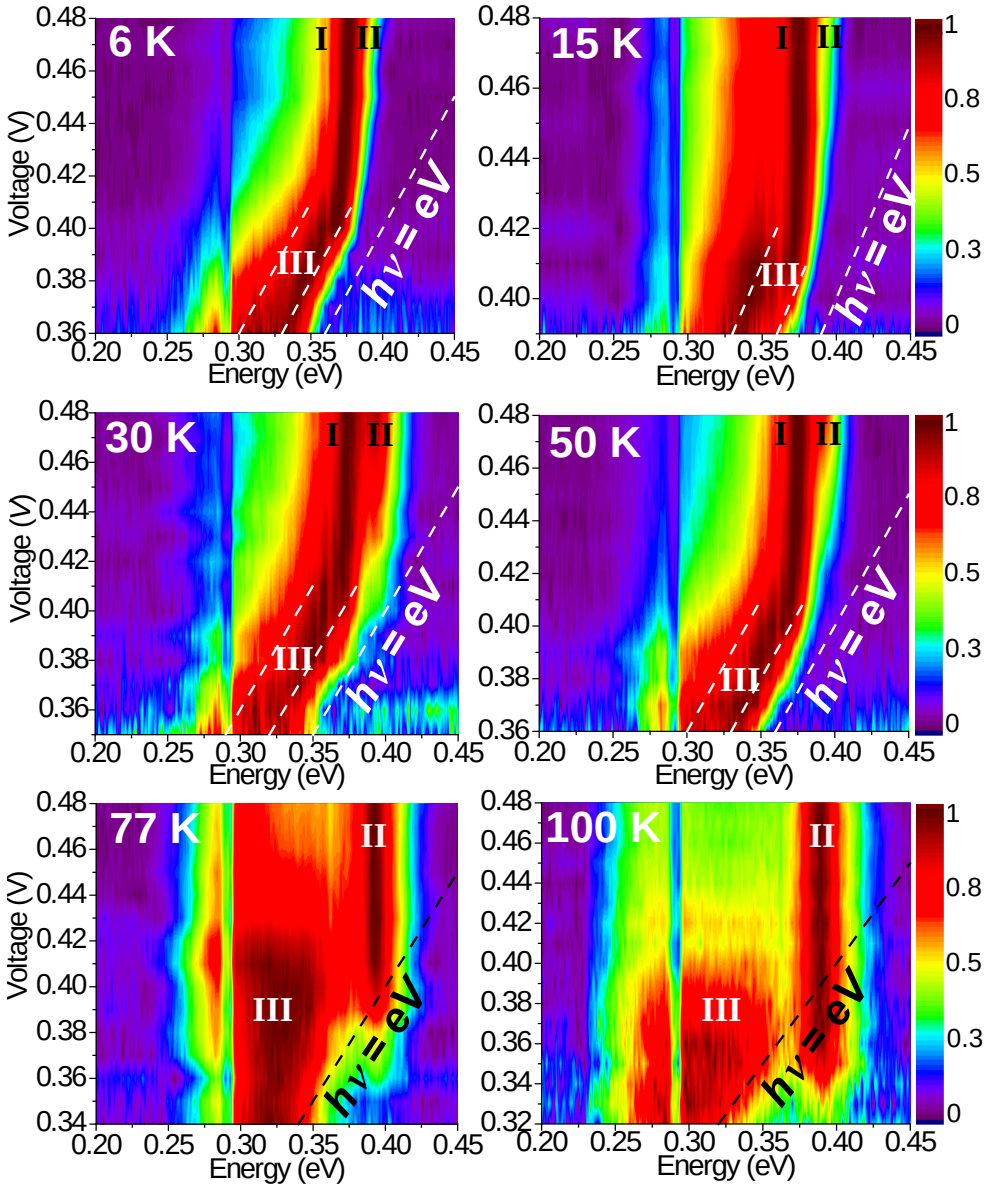


Figure 8.2: Colour maps of the normalized EL intensity as a function of photon energy and applied bias at T = 6-100 K. The dashed lines represent the conditions $h\nu = eV$, $h\nu = eV - \hbar\omega_{LO}$ and $h\nu = eV - 2\hbar\omega_{LO}$, where $\hbar\omega_{LO}$ = 29 meV is the energy of the longitudinal optical (LO) phonon of InAs.

- At intermediate temperatures (T = 77-100 K) (Figure 8.1 and 8.2), we observe two distinct peaks, a narrow high energy peak at ~ 0.390 eV (peak II) and a broader low energy band between 0.27 eV and 0.35 eV (peak III). The EL peak positions of both peaks II and III are weakly dependent on the applied bias

in this temperature range. These peaks remain distinct for all the applied biases and there is no evidence of the evolution of the I-peak onto the III-band with decreasing applied voltages, as observed for $T < 77$ K.

- At temperatures $T > 120$ K (Figure 8.3 and 8.4) the intensity of peak III weakens with increasing temperature. Peak II is dominant in this temperature regime and its position does not depend on the applied voltage. However, its position decreases with increasing temperature, consistent with the reduction of the band gap energy.

The temperature dependence of the band gap energy, E_g, of InAs is accounted for by using Varshni equation[95]:

$$E_g(T) = E_g(0) - \alpha \frac{T^2}{T+\beta}, \tag{8.1}$$

where $E_g(0)$ = 0.415 eV is the band gap energy of InAs at T = 0 K, α = 2.76 $\times 10^{-4}$ eV/K and β = 83 K. The additional reduction of the band gap in the In(AsN) QW due to the N-incorporation was accounted for by using the band anticrossing (BAC) model, as described in Paragraph 2.1.1. The calculated value of the *e-h* recombination energy, $h\nu_X$, for the In(AsN) QW is shown in Figure 8.5 for N-content [N] = 1% (dashed red curve), [N] = 1.3% (dashed magenta curve) and [N] = 1.5% (dashed black curve). A deviation from the nominal N-composition can have a significant effect on the reduction of the band gap energy of In(AsN). The calculated curves for $h\nu_X$ are compared with the *T*-dependence of the energy peak position of peaks I (black triangles), II (blue dots) and III (green squares) at $V \sim 0.40$ V. At low *T*, the *T*-dependence for peaks I and II deviates from that expected for $h\nu_X$. This suggests that at $T < 77$ K peaks I and II arise from the recombination of carriers from donor and/or acceptor

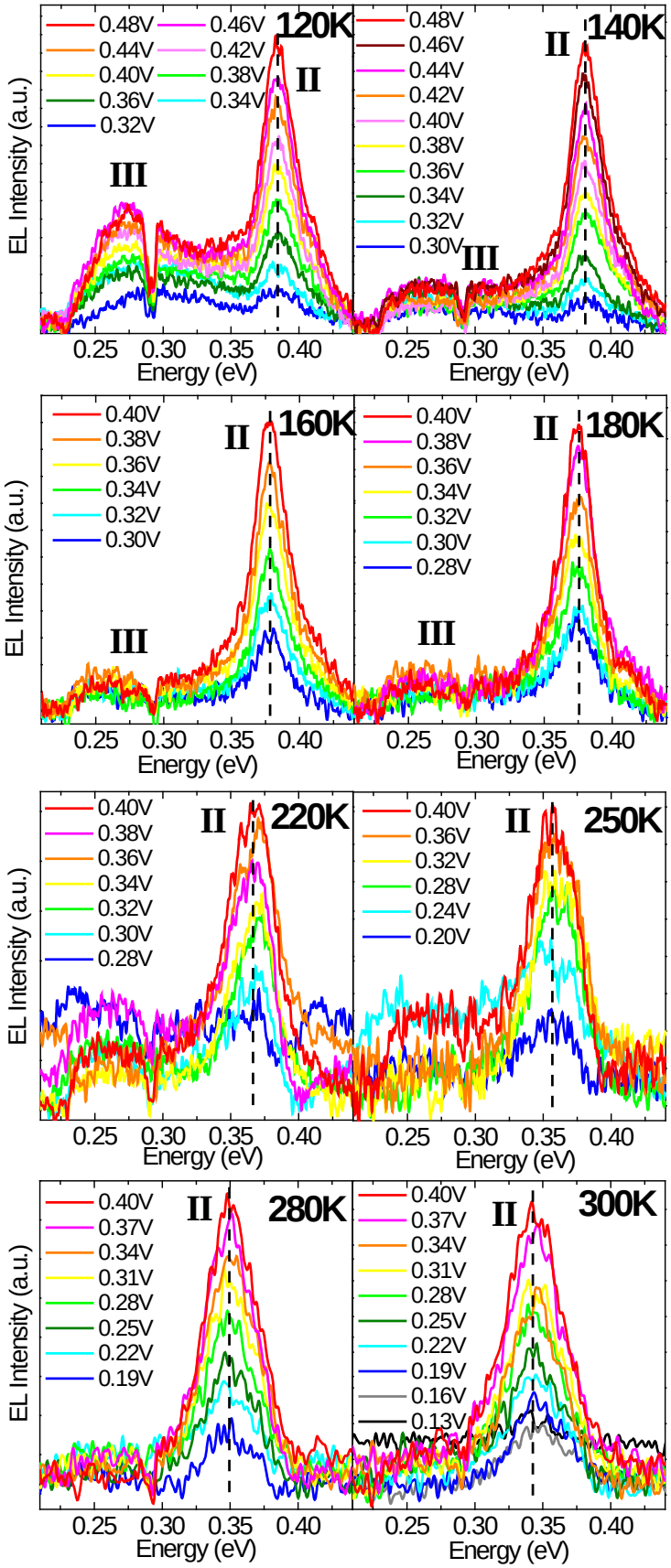


Figure 8.3: EL spectra of an In(AsN)/(InAl)As RTD at different applied biases and at temperatures T = 120-300 K.

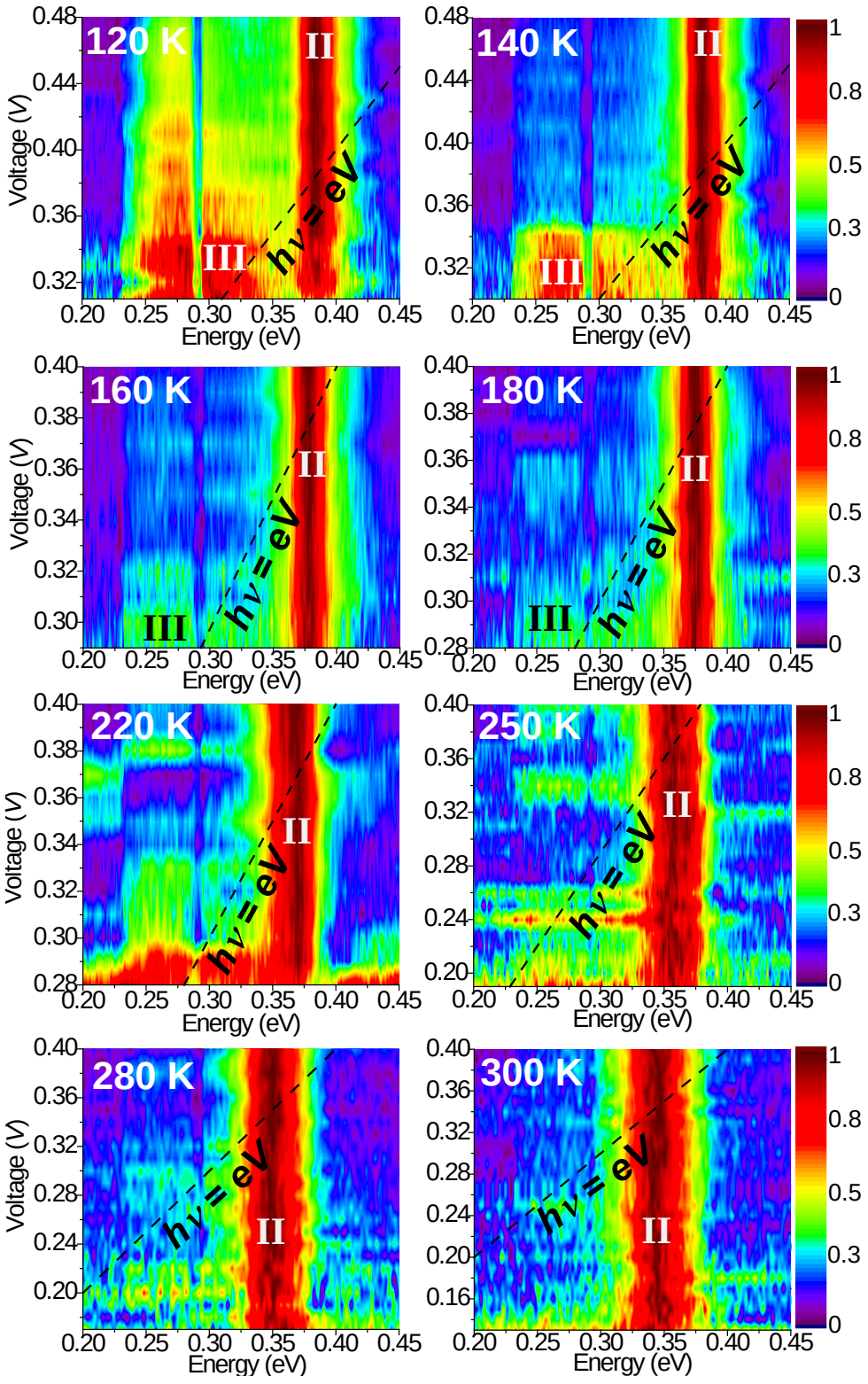


Figure 8.4: Colour maps of the normalized EL intensity as a function of photon energy and applied bias, at T = 120-300 K. The black dashed line represents the condition $h\nu = eV$.

states in the QW. With increasing *T* (above 77 K) these states become ionized. Thus with increasing *T*, the *e-h* recombination from the QW becomes dominant and the EL emission energy of peak II follows the *T*-dependence of $h\nu_X$. Also, peak III occurs at energies that are significantly smaller than $h\nu_X$. This suggests that this peak arises from carrier recombination from deep states in the band gap.

Notably, for temperatures $T > 77$ K, we also observe photon emission at energies higher than the excitation energy. This phenomenon, also referred to as up-conversion luminescence (UCL), was previously observed also in InAs/GaAs self-assembled quantum dots in both photoluminescence[194] and electroluminescence[195, 196] experiments. The region of UCL corresponds to emission in the energy range $h\nu > eV$ in the colour maps of Figures 8.2 and 8.4.

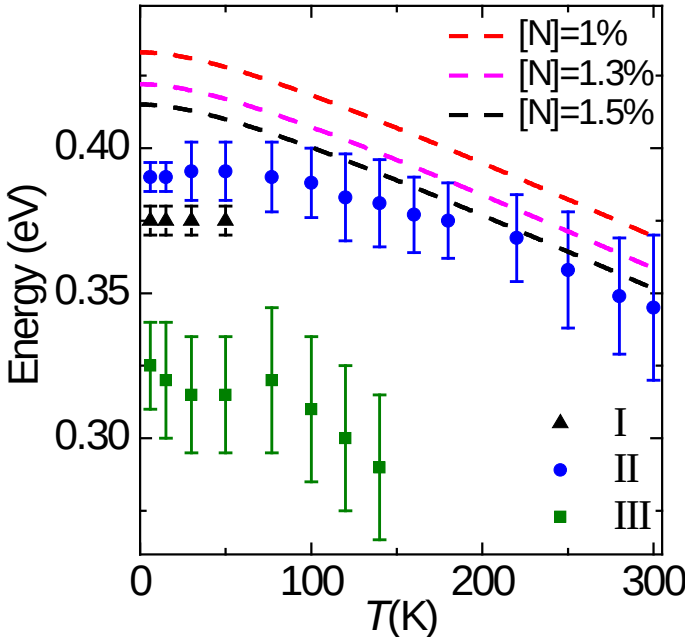


Figure 8.5: Temperature dependence of the energy position of peak I (black triangles), II (blue dots) and III (green squares). These are compared with the temperature dependence of the *e-h* recombination energy, $h\nu_X$, of the In(AsN) QW with nitrogen content [N]=1% (dashed red curve), [N]=1.3% (dashed magenta curve) and [N]=1.5% (dashed black curve).

8.2 Modelling charge injection and recombination

We model the energy band diagram of the RTD by solving Schrödinger's and Poisson's equations, as done in Section 7.4. Figure 8.6 shows the calculated band diagram at T = 6 K and under flat band conditions. The energies of the bound electron and hole states in the QW layer are calculated as explained in Appendix A. We estimate the energy of the electron (hole) ground state to be E_1^e= 48 meV (E_1^h= 8 meV), calculated from the bottom of the CB (top of the VB) of the In(AsN) QW. These states are labelled as *E* and *H* in Figure 8.6, respectively. We also assume the presence of defect states in the band gap. We estimate that the N-related 0D states (labelled as *N* in Figure 8.6) lie at an energy E > 40 meV below the CB minimum of In(AsN), as explained in Section 7.4.

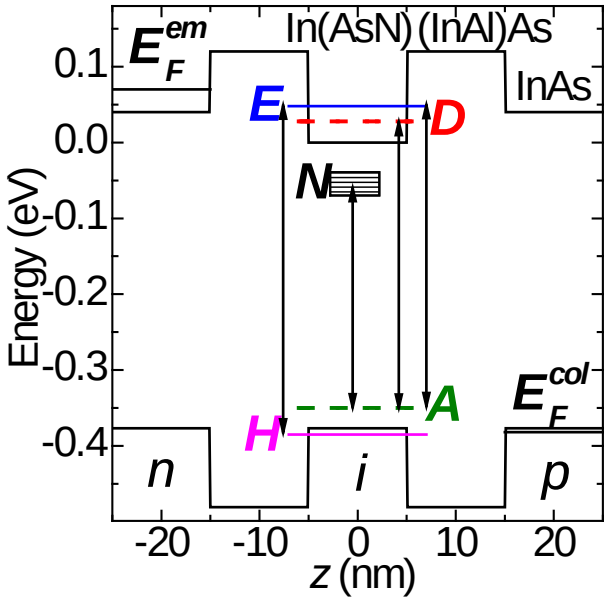


Figure 8.6: Energy band diagram of an In(AsN)/(InAl)As RTD at T = 6 K and at the flat band conditions. The diagram shows the electron (*E*) and hole (*H*) ground states in the QW, as well as donor (*D*), acceptor (*A*) and N-related (*N*) states. The arrows indicate optical transitions between different states.

Also, deep acceptor levels (labelled as *A* in Figure 8.6) are known to form in InAs, with binding energies (E_b) between 35 meV and 50 meV[96, 197]. As for the donors, these may include shallow donor states (E_b ~ 2 meV) or cluster of donors (E_b ~ 10-20 meV)[96] (labelled as *D* in Figure 8.6). However, it should be noted that the binding energies of donor and acceptors states are generally different in quantum confined structures.

The Fermi energies of the emitter/collector state shown in Figure 8.6 are estimated as:

$$E_F^{em} = \frac{\hbar^2}{2m_e^*}(3\pi^2 n_e)^{2/3} \tag{8.2}$$

and

$$E_F^{col} = \frac{\hbar^2}{2m_{hh}^*}(3\pi^2 n_h)^{2/3}\ , \tag{8.3}$$

respectively, where m_e^* = 0.025 m_0 (m_{hh}^*= 0.41 m_0) is the electron (heavy hole) effective mass of InAs and n_e (n_h) is the electron (hole) density in the emitter (collector) layer, as described in Section 4.1.2. We thus estimate E_F^{em} = 30 meV and E_F^{col} = 2 meV. Note that, since $m_e^* \ll m_{hh}^*$, $E_1^e \gg E_1^h$ and $E_F^{em} \gg E_F^{col}$.

We now examine the injection and recombination of carriers at various *T* and *V*. In Figure 8.7 we plot the colour map of the EL intensity versus *V* and $h\nu$ for *T* = 6 K, 100 K and 300 K, along with the corresponding current-voltage, *I*-*V*, characteristic.

The *I*-*V* curve at *T* = 6 K (Figure 8.7a) shows the expected exponential diode-like *I*-*V* for biases above the flat band conditions (*V* > 0.4 V): in this bias regime, the main contribution to the current is from the thermal diffusion of electrons (holes) from the *n*- (*p*-) to the *p*- (*n*-) side of the diode. Correspondingly, the EL emission (peaks I and II) arises from the recombination of carriers from the In(AsN) QW due to dopants and/or QW bound states, and

the emission energy has a weak dependence on the applied bias. For biases below the flat band conditions ($V < 0.4$ V), the current has a much weaker bias dependence. Under this bias regime, the current arises mainly from Zener tunnelling of electrons into defect states in the band gap of In(AsN). Thus the current is strongly suppressed and the EL emission occurs at lower energies (peak III).

The contribution to the current of Zener tunnelling through defect states becomes less dominant with increasing temperature (as already shown in Figure 7.2a). At $T = 100$ K (Figure 8.7b), a deviation from the exponential increase of the current with the applied voltage is still partially visible ($V < 0.38$ V). At low applied biases, a broad EL band can also be seen at an energy $h\nu \sim 0.3$ eV (peak III). However, even when this emission is detected, the higher energy peak II is dominant, consistent with the thermal diffusion of carriers. Finally, at $T = 300$ K (Figure 8.7c), a much higher current flows through the diode. Even at applied biases below the flat band conditions, electrons and holes have enough energy to thermally diffuse, leading to an EL emission (peak II) whose energy position is weakly dependent on the applied voltage.

We plot the modelled band diagrams for $T = 6$K (Figure 8.8), 100K (Figure 8.9), and 300K (Figure 8.10). For each temperature, along the colour map of the normalized EL intensity (a), we plot the band diagram corresponding to a selected voltage range, below (b), close to (c) and above (d) the flat band condition at that temperature. In the colour maps, we mark the EL peak at the selected voltages with a white asterisk.

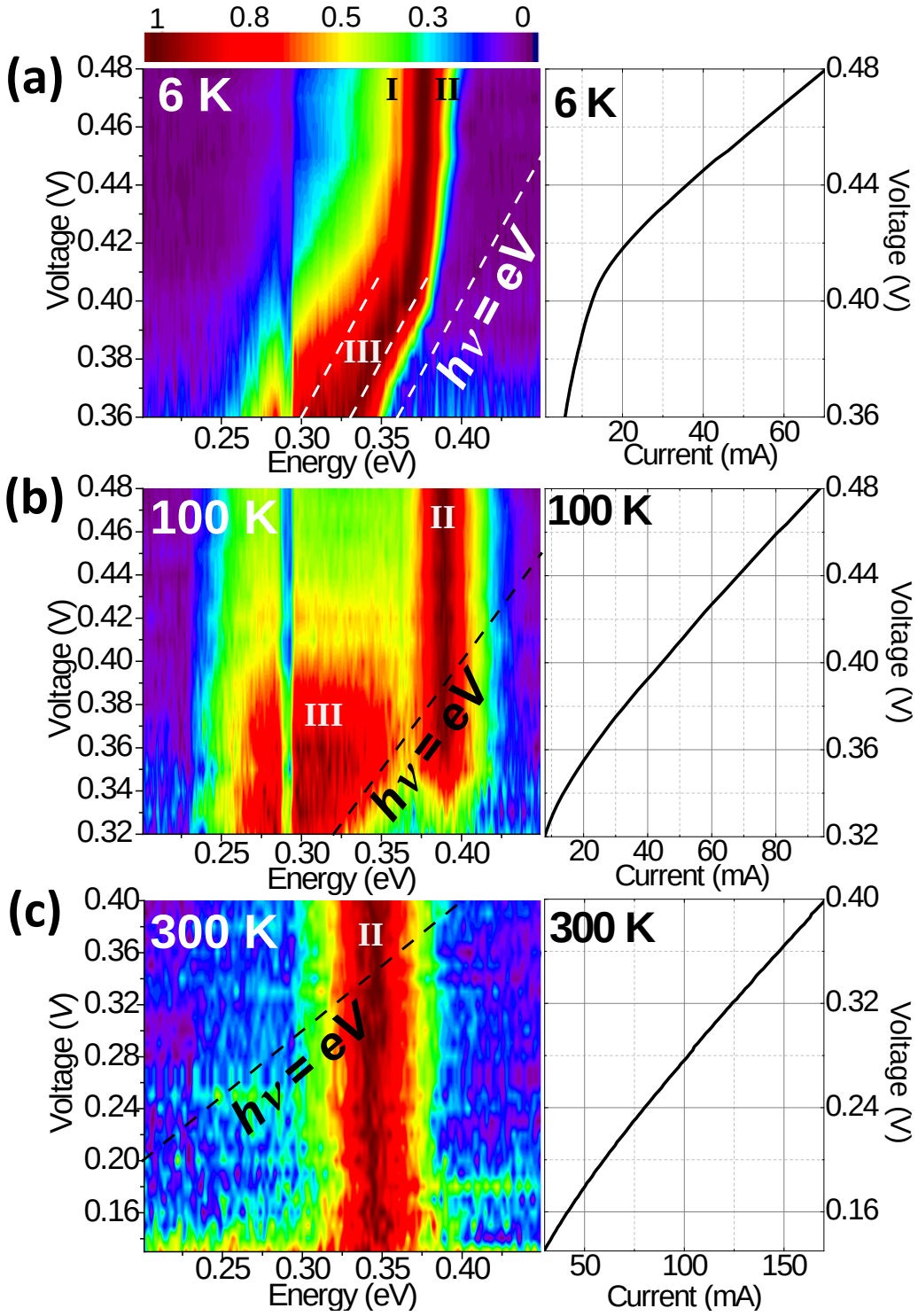


Figure 8.7: Colour maps of the normalized EL intensity at T = 6 K **(a)**, 100 K **(b)** and 300K **(c)** (left) and the corresponding I-V curves (right).

- At T = 6 K (Figure 8.8), in the bias regime around (Figure 8.8c) and above (Figure 8.8d) the flat band conditions, the Fermi level in the three dimensional (3D) electron gas of the emitter is resonant with the bound electron state (E) of the QW or shallow donor level (D) in the QW, thus enabling the resonant transmission of electrons into the QW. On the other hand, the collector state is not resonant with the ground hole state (H) of the QW; however, holes can still tunnel into deep acceptor levels (A) in the QW. Thus, at low T, the recombination of the injected carriers results in emission at energies lower than

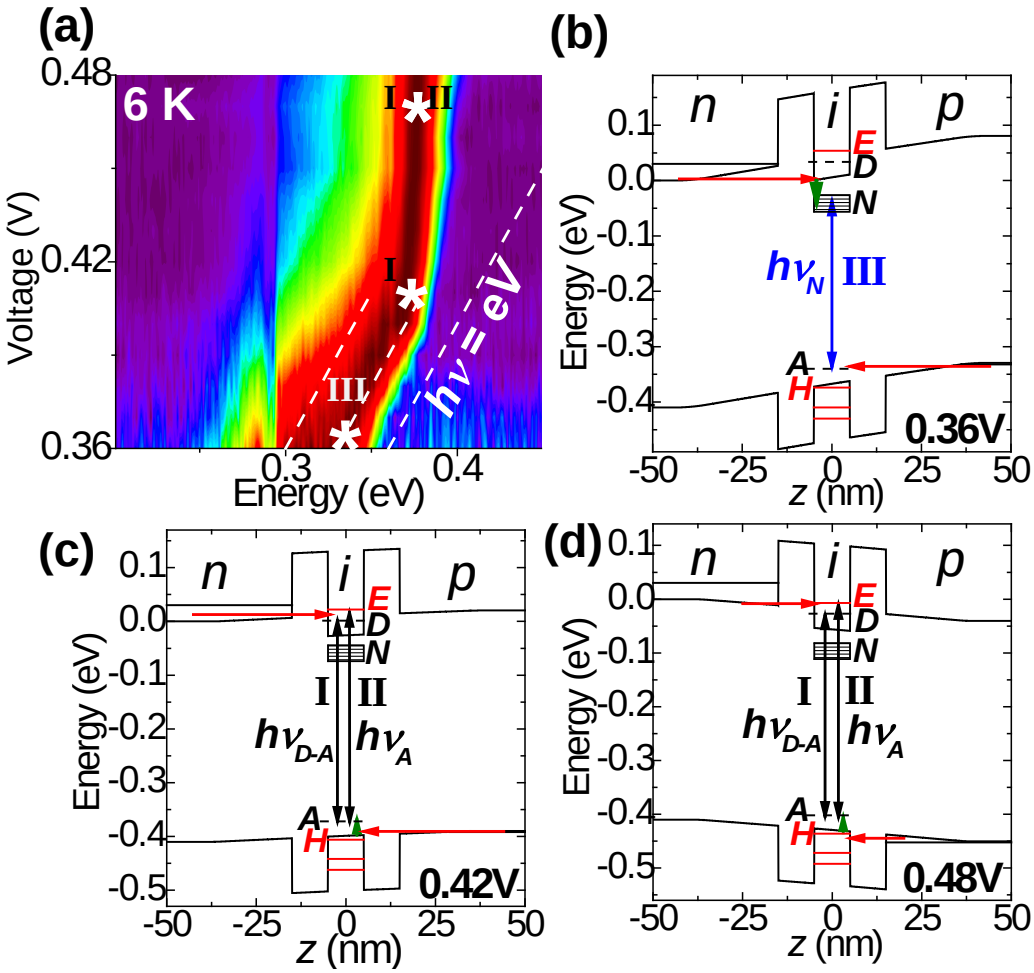


Figure 8.8: Colour map of the normalized EL intensity versus V at T = 6 K **(a)** and the modelled band diagrams at V = 0.36 V **(b)**, 0.42 V **(c)** and 0.48 V **(d)**. These bias conditions correspond to the white asterisks in the colour map.

the electron-hole recombination energy in the QW, corresponding to peaks I and II. We attribute the main peak I to a donor-acceptor recombination ($h\nu_{D-A}$) and the weaker peak II to the acceptor-free electron recombination (at $h\nu_A$). This assignment is consistent with the deviation of the *T*-dependence of peaks I and II from that of $h\nu_X$ at low *T* (Figure 8.5).

Below the flat band condition (Figure 8.8b), the emitter states are not resonant with the bound state of the QW. However, electrons can tunnel from the emitter into the N-related 0D states in the band gap (*N*) following the emission of one or two LO phonons (green arrow in Figure 8.8b) and recombine with holes in acceptor (*A*) states (peak III at $h\nu_N$). We note that the III-peak appears as the evolution of the I-peak with decreasing biases. This confirms the presence of a broad band of defect states below the CB edge of In(AsN).

- At *T* = 100 K (Figure 8.9), in the bias regime around (Figure 8.9c) and above (Figure 8.9d) the flat band conditions, the EL emission is dominated by the II-peak, whose *T*-dependence follows that expected for $h\nu_X$ for *T* > 77 K (Figure 8.5). We assign this peak to the recombination of electrons in the ground state of the QW (*E*) with holes in deep acceptor levels (*A*), similarly to what observed at the same bias conditions at *T* = 6 K. However, we observe no visible trace of the I-peak ($h\nu_{D-A}$) at this temperatures. This suggests that the shallow donor levels involved in the EL I-peak recombination are ionized for *T* > 77 K.

Below the flat band condition (Figure 8.9b), we still distinctly observe the emission from the II-peak. Note that this emission occurs at energies higher than the excitation energy (*i.e.* $h\nu > eV$). At these temperatures, electrons have enough thermal energy to occupy the QW ground state (*E*), which lies at an energy higher than the Fermi level of the emitter. The tunnelling of electrons

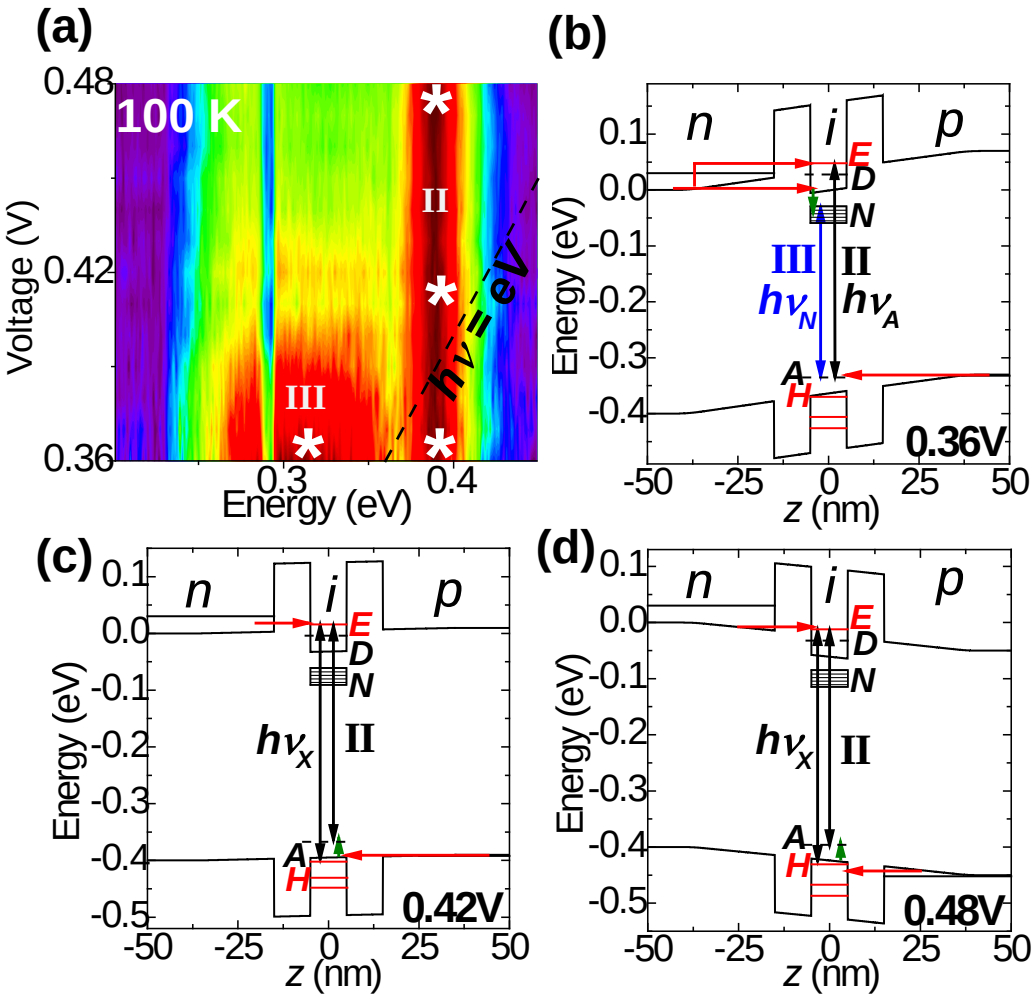


Figure 8.9: Colour map of the normalized EL intensity versus V at T = 100 K **(a)** and the modelled band diagrams at V = 0.36 V **(b)**, 0.42 V **(c)** and 0.48 V **(d)**. These bias conditions correspond to the white asterisks in the colour map.

into the QW ground state can also be assisted by the absorption of a LO phonon. This is consistent with a dominant UCL signal at high temperatures (T > 100 K). It is also worth noting that non-radiative Auger recombination can contribute to UCL, particularly if it involves injection of carriers into strongly localized states and strong Coulomb interaction between carriers[196]. We note that electrons in the emitter can also tunnel into the QW and relax into the N-related defect states (N) with emission of a LO phonon (green arrow in Figure 8.9b). The electrons then recombine with holes trapped in the deep acceptor levels (A)

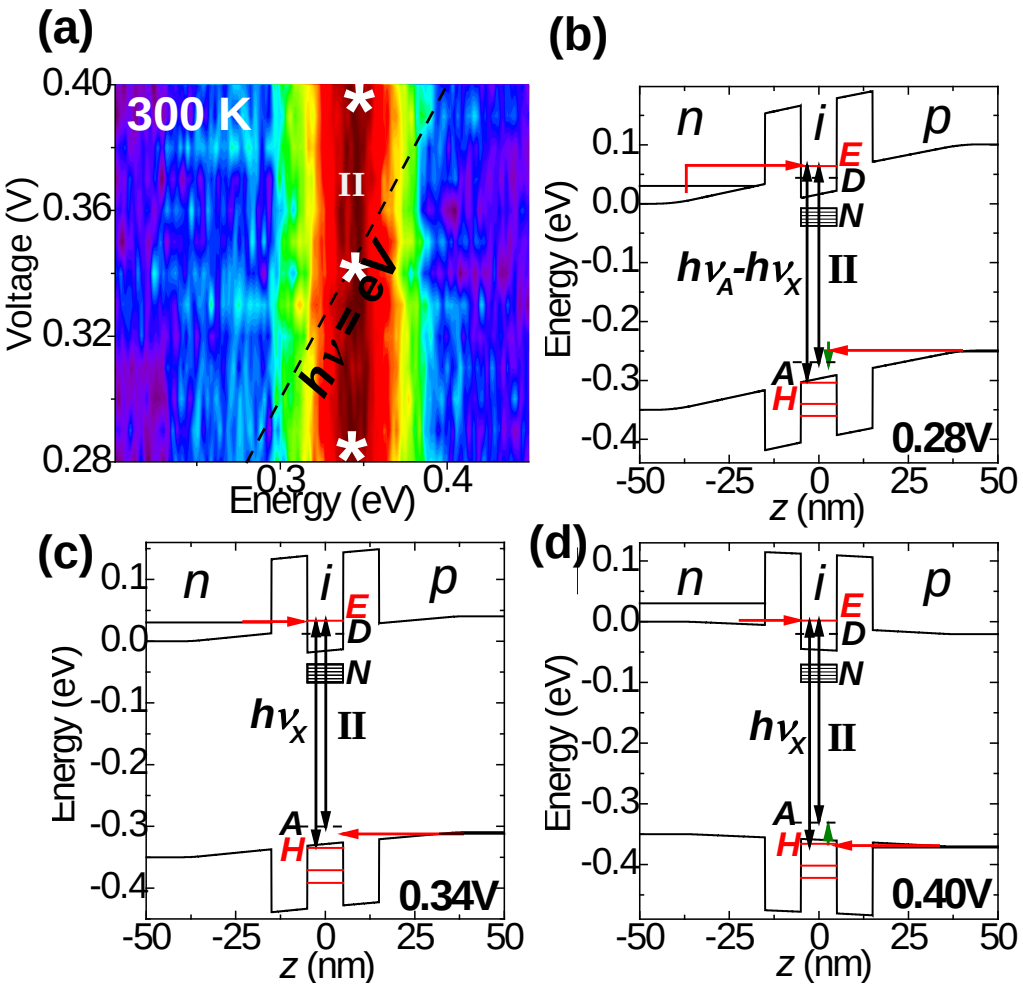


Figure 8.10: Colour map of the normalized EL intensity versus V at T = 300 K **(a)** and the modelled band diagrams at V = 0.28 V **(b)**, 0.34 V **(c)** and 0.40 V **(d)**. These bias conditions correspond to the white asterisks in the colour map.

in the band gap, resulting in the lower energy III-peak at $h\nu_N$.

- Finally, at T = 300 K (Figure 8.10), the electrons have enough thermal energy to diffuse over the QW barrier from the emitter state into the electron ground state of the QW (E) even at the lowest biases (Figure 8.10b). Close to (Figure 8.10c) or above (Figure 8.10d) the flat band condition, the 3D electron gas in the emitter is always resonant with the E-state. The holes from the collector tunnel into the hole ground state of the QW (H) or into deep acceptor states in the band gap (A), either resonantly or following the emission or

absorption of a LO phonon (indicated by a small green arrow in Figures 8.10b-d). At all the applied biases, the EL emission is dominated by the II-peak. We note that for T > 200 K the peak-II energy is broad and very close to $h\nu_X$. Thus this peak may arise either from the *E-A* recombination ($h\nu_A$) or from the *e-h* recombination from the ground states of the QW ($h\nu_X$).

8.3 Summary

In summary, we have reported EL studies of In(AsN)/(InAl)As RTDs. These structures emit in the MIR wavelength range λ = 3 - 5 μm upon electrical injection of carriers. We have reported on a bias-tuneable EL emission at energies considerably lower that the band gap energy of In(AsN) at low temperature (T < 77 K). We attribute this behaviour to the presence of the N-related defect states below the CB minimum of In(AsN). The tunnelling of electrically injected carriers into these strongly localized 0D states plays a key role in the recombination of carriers between states in the band gap, thus enabling the tuning of the EL emission towards longer wavelengths, up to λ ~ 5 μm. The MIR luminescence from the RTD structure is observed up to room temperature, notably with the occurrence of up-conversion luminescence (UCL) for T > 77 K[194, 196]. Non-radiative Auger recombination processes may contribute to the arising of output luminescence of energy $h\nu$ higher than that provided to the injected carriers by the applied voltage, V. With this regard, the presence of strongly localized N-related states in the band gap may be a significant contribution to the Auger process[195].

The observation of MIR UCL up to room temperature shows potential for applications, such as low-budget MIR LEDs. Further research paths may

include the study of the EL emission from the RTDs at different N-content and/or QW design. This could enable extending the range of the achievable wavelength of the luminescence output, as well as providing further insight into the origin, nature and configuration of the N-related 0D states in the band gap of In(AsN), whose effect on the transport and opto-electronic properties can be effectively probed by our RTD structure.

Chapter 9

Conclusions and future directions

The aim of this thesis was to investigate the effects of the incorporation of nitrogen (N) and hydrogen (H) atoms in the III-V InAs semiconductor. The findings of my research can be summarized as follows:

(i) I have shown that the increase of the electron density in the dilute nitride In(AsN) alloy upon the *post-growth* incorporation of hydrogen in the crystal induces a surface plasmon polariton (SPP) mode in the mid-infrared (MIR) spectral range.

(ii) The plasmonic behaviour of the highly doped In(AsN):H can be suppressed locally by means of laser annealing or electron beam annealing, as probed by Raman spectroscopy studies.

(iii) I have demonstrated that the incorporation of N in InAs leads to a pronounced and extended negative differential resistance (NDR) in the current-voltage (*I*-*V*) characteristic of In(AsN)/(InAl)As resonant tunnelling diodes (RTDs); this NRD is due to a novel type of resonant Zener tunnelling, assisted by N-related strongly localized zero-dimensional (0D) states in the In(AsN) band gap, whose small confinement length is probed by magneto-tunnelling experiments.

(iv) The In(AsN)/(InAl)As RTDs emit in the MIR spectral range (λ = 3-5 μm), as assessed by electroluminescence (EL) studies. A voltage-tuneable

emission was demonstrated at temperatures T < 77 K and up-conversion luminescence (UCL) was observed over a wide range of temperatures (77-300 K).

The main findings and prospects for further studies are discussed below.

9.1 MIR plasmonics with the highly doped In(AsN):H

The electron density, n_e, of the dilute nitride In(AsN) increases by two orders of magnitude, up to $n_e \sim 10^{19}$ cm^{-3}, upon the incorporation of hydrogen in the crystal[31]. This behaviour is attributed to the role of the N-atoms, which act as H-traps and lead to the formation of N-H donor complexes in a thin (0.1-1 μm) conductive layer below the surface[32]. Notably, this is not observed in N-free InAs[31] or in other dilute nitride compounds[30]. In this thesis, I have investigated the possibility to exploit the highly doped In(AsN):H semiconductor as a plasmonic material and I have proposed a novel approach to the spatial control of its plasmonic behaviour by laser annealing[166].

The high electron density achieved following the H-irradiation of In(AsN) epilayers (with N-content [N] = 1%) enables the excitation of a surface plasmon polariton (SPP) mode at frequencies ω_{spp} ~ 900-1000 cm^{-1} that is detected with reflectance spectroscopy techniques in the attenuated total reflection (ATR) configuration. These frequencies correspond to MIR wavelengths (λ ~ 10 - 11 μm). The measured values obtained by the spatial mapping of ω_{spp} across the epilayers are also consistent with simulations of the SPP dispersion in our material.

I also demonstrated that the plasmonic response of In(AsN):H can be spatially tailored and suppressed by laser-annealing, achieved by focusing a laser beam of wavelength λ = 633 nm and spot diameter d ~ 1 μm onto the

In(AsN):H surface at powers P > 10 mW and exposure times $\tau \geq 300$ s. This causes the quenching of the plasmonic L^+ Raman mode. This is attributed to the dissociation of the N-H donor complexes, thus restoring the pristine conditions of as-grown In(AsN). The spatial mapping of the L^+ Raman intensity shows a modification on the μm-scale. We estimate a temperature rise of up to ΔT = 140 K in the centre of the spot induced by the laser beam on the In(AsN):H surface. Atomic force microscopy (AFM) studies of the In(AsN) epilayers before and after hydrogenation show that no surface damage is caused by the laser annealing for the range of laser powers and exposure times used in our experiment.

In summary, our approach represents a reproducible and non-destructive means to modulate the electron density and plasmonic properties of a highly doped semiconductor by changing its chemical composition with micrometric resolution. This approach could be further developed for large-scale device fabrication with control of the plasmonic response on the μm-scale. The results of these studies were published in *Advanced Optical Materials* **6**, 1700492 (**2018**)[166].

9.2 Novel approach for H-removal with e-beam annealing

In this thesis, I have demonstrated that the dissociation of the N-H bond responsible for the increase of the electron density of In(AsN):H is successfully achieved by laser annealing. However, this approach is limited to the micron spatial resolution by the diffraction limit of the visible light. It is thus of great interest to push the limit of the modulation of electron density in a crystal down to the nanometre resolution. For example, electrons have diffraction limits down

to the nanometre scale depending on their kinetic energy. In this work, I have investigated the effect of electron beam annealing on the highly doped In(AsN):H. An electron beam (accelerating voltage V_{acc} = 20 kV, electron current I > 10 nA) of a field emission gun-scanning electron microscope (FEG-SEM) focused onto the surface of an In(AsN):H epilayer for an exposure time of τ > 5 min can induce a decrease of the electron density, as probed by Raman spectroscopy and SEM imaging. Atomic force microscopy (AFM) studies show that no topographical modification of the surface occurs upon e-beam annealing. Thus this is a reproducible and non-destructive approach to locally change the conductivity of a highly doped semiconductor, similar to laser annealing. However, contrary to what observed with laser annealing, where the diffusion of H-atoms away from the annealed spot was likely assisted also by a thermal effect, the spatial distribution of the intensity of the plasmonic Raman mode reveals that the exposure to an e-beam rather induces an accumulation of H-atoms around the annealed spot. To evaluate the effects of temperature on the dissociation of the N-H complex and/or on the H-diffusion in the lattice, the exposure to an e-beam was studied at temperatures up to T = 150 °C.

It is also worth noting that relatively high electron current values (I > 10 nA) are required to achieve visible effects for the H-removal on the surface. The focusing of a high density current electron beam thus limits the spatial resolution of the proposed writing technique. A comprehensive study of the different effects arising from laser and electron beam annealing could provide further insights into the formation and dissociation of the N-H donor complex in In(AsN):H and into the dynamics of H-diffusion in the host crystal. These results are in preparation for a journal publication.

9.3 Resonant Zener tunnelling via 0D states in In(AsN) RTDs

The incorporation of small quantities of nitrogen (N) has a profound effects on the transport and opto-electronic properties of various III-V semiconductors[7, 8, 93]; in this thesis I have focused on the narrow gap InAs compound[172]. Here, I have presented the first experimental studies of a multi-layered *p–i-n* In(AsN)/(InAl)As resonant tunnelling diode (RTD), where nitrogen ([N] = 1%) was introduced in the intrinsic (*i*) quantum well (QW) layer of the diode[143].

By acquiring the current-voltage, *I-V*, characteristics at low temperature (T = 4.2 K), we observed an ohmic behaviour for both polarities around zero bias. The current reaches a maximum at a peak at $V \sim 0.06$ V, followed by a pronounced and extended region of negative differential resistance (NDR) at biases much lower than those required to reach flat band conditions. Notably, both these features are weakly dependent on temperature and are not observed on a control sample, with no N in the QW layer.

From the *T*-dependence of the current over a wide range of T (15 - 300 K), two different competing transport phenomena can be envisaged. One is resonant Zener tunnelling of electrons through deep-energy N-related states; this process dominates at biases lower than those required to achieve flat band conditions. On the other hand, the thermal diffusion of carriers over the diode built-in potential is dominant at high applied biases and at high T.

We probed the size of the N-related states by magneto-tunnelling spectroscopy (MTS). From the magnetic field dependence of the current at the peak, we can estimate the confinement length of the N-related states, $\lambda_0 < 2$ nm, which is much smaller than those expected for a shallow donor level in InAs.

From the *I-V* curves, we estimate that the strongly localized states lie at energies > 40 meV below the conduction band (CB) minimum of the QW layer. These observations demonstrate a novel type of Zener tunnelling, assisted by 0D states arising from the incorporation of N in InAs. These levels effectively act as "stepping stones" for resonant transmission of electrons from the *n*- to the *p*-side of the diode. This also accounts for the arising of the NDR region when the *n*- and *p*- sides of the diode are off-resonance.

It is possible to have some insight into the origin of the N-related 0D states that we observe with our tunnelling experiments. Substitutional N-levels are expected to lie well-above the CB edge[99] of In(AsN) and thus cannot be responsible for the localized energy levels that we observe in the band gap. On the other hand, it is well established that non-substitutional N-related crystal defects (such as such as N–As split interstitials, N-antisites, and interstitial-N) tend to form in In(AsN)[102]. These observations open new questions of fundamental relevance on the role of nitrogen atoms in III-V crystals and require further theoretical studies and experimental validations. These results were published in *Scientific Reports* **6**, 32039 (**2016**)[143].

9.4 Electroluminescence (EL) studies of In(AsN) RTDs

It is of great interest to study the luminescence from the In(AsN)/(InAl)As RTDs resulting from the recombination of electrically injected electrons and holes. This may provide a deeper insight into the nature of the N-related defect states that we observe in the band gap of In(AsN). In this work, I have presented electroluminescence (EL) spectroscopy studies of our RTDs under different temperatures (from 6 K to 300 K). For each temperature, we modelled the

energy band diagram at different applied biases above and below the flat band conditions, to correlate the band alignment with the measured EL emissions.

At low temperatures (T = 6-50 K), the EL emission can be tuned by the applied voltage over the MIR wavelength range λ = 3-5 μm. In particular, for biases V < 0.40 V, the EL peak redshifts down to ~ 0.25 eV (λ ~ 5 μm), thus to energies significantly lower than the band gap energy of In(AsN). From the band alignment, we estimate that the recombination of electrically injected carriers is assisted by tunnelling into the strongly localized N-related defect states below the CB minimum of In(AsN). This shows that the EL emission has a strong dependence on the applied bias and it can be activated at voltages that are much smaller than the bias required to achieve flat band conditions. Notably, we observe the occurrence of up-conversion luminescence (UCL) at T > 77 K, up to room temperature. The presence of strongly localized N-related states in the band gap may be play a key role in enhancing the UCL, for example by contributing to Auger recombination processes. These results are in preparation for a journal publication.

9.5 Future directions

The results presented in this thesis show some novel effects arising from the incorporation of N- and H-atoms in the III-V InAs semiconductor. These results will stimulate further fundamental studies and open new research directions, some of which are presented in this Section.

9.5.1 Novel approach to MIR plasmonics

The proposed approach to the modulation of the electron density of a highly doped semiconductor by *post-growth* H-incorporation and H-removal by laser or electron beam annealing with microscopic precision opens a novel and interesting research path. This approach can be combined with the study of plasmonic phenomena, which rely on the enhancement of the electric field near a surface, and could be exploited for applications such as the detection of vibrational-rotational fingerprints of target trace gas species and bio-molecules in the MIR range.

The approaches presented in this thesis rely on the homogeneous hydrogenation of the epilayer surface and on the dissociation of the N-H bond by using various methods, such as laser and e-beam annealing. An alternative approach could employ the selective hydrogenation of the crystal by using surface masks to realize plasmonic structures. A common configuration consists of one-dimensional (1D) periodic arrays, which can be fabricated by large area surface patterning techniques, such as electron beam lithography (EBL), with sub-micron resolution[49, 155]. The fabrication of sub-wavelength structures enables the enhancement of the electric field intensity near the surface and the excitation of localized surface plasmon resonances (LSPRs). The proposed pattern consists of a periodic set of stripes with different period p = 2, 3 and 4 μm and width w = 250, 500, 750 and 1000 nm. These masks (shown in Figure 9.1a) were realized by EBL. The fabrication by EBL enables to achieve a high periodicity of the pattern and a sharp interface between the mask and the exposed region, as assessed by scanning electron microscopy (SEM) (Figure 9.1b). However, it is worth noting that the effective incorporation and diffusion

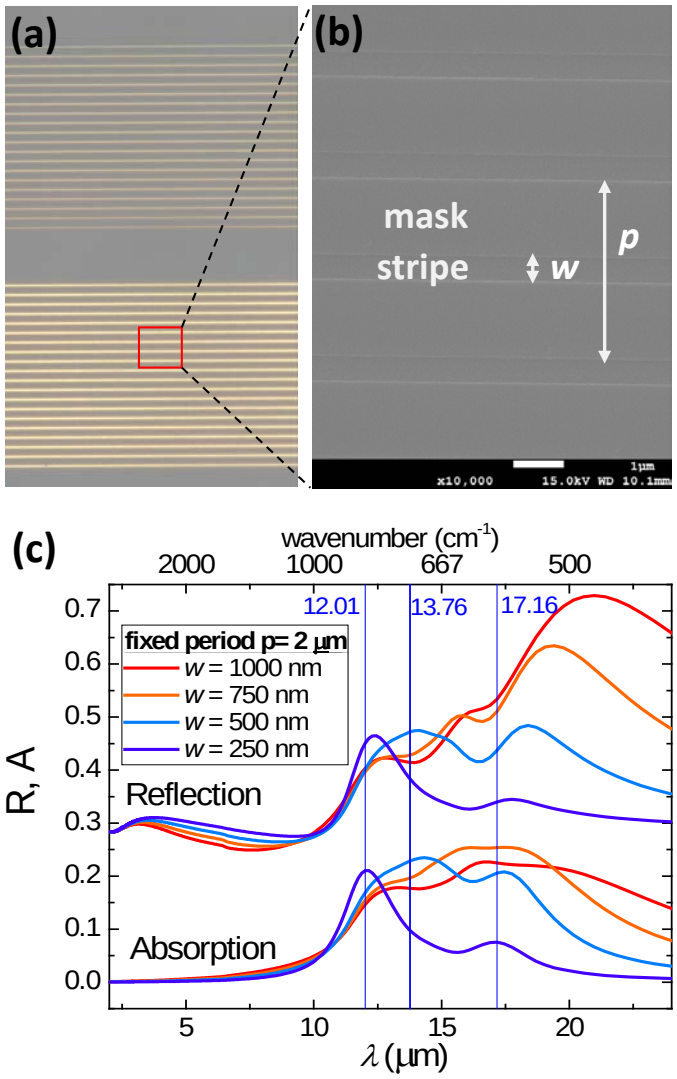


Figure 9.1: Optical **(a)** and SEM **(b)** images of the surface masks realized by EBL. **(c)** FDTD simulations of the absorption (A) and reflection (R) spectra of the proposed 1D plasmonic arrays with fixed period p = 2 µm and varying width w = 250, 500, 750 and 100 nm (courtesy of Dr M. Bomers, Université de Montpellier).

of H-atoms in III-V semiconductors usually requires temperatures T > 300 °C. This constraint requires the fabrication of surface masks with e-beam resists that are stable at these temperatures. Finite-difference time-domain (FDTD) simulations (Figure 9.1c) show that it is possible to tune these LSPRs by either

monitoring the doping of the crystal (in our case, by using different hydrogenation conditions) or by monitoring the periodicity and/or the lateral size of the patterns[49, 155]. I am planning to realize such 1D plasmonic arrays by EBL and to study the response of the plasmonic gratings obtained following the selective hydrogenation of the epilayers.

The proposed *post-growth* H-doping represents an appealing alternative to the traditional doping methods of InAs during the growth, which then require wet chemical etching techniques for the realization of plasmonic gratings.

9.5.2 Towards an understanding of N-related defects

The observation of N-related localized defect states in the band gap of In(AsN) raises new questions of fundamental relevance. Such defect states can be probed with our RTD structure and have a strong influence on the electrical and optical properties of these devices. However, the identification of the nature of these N-related defects in In(AsN) requires further studies. In particular, a comprehensive theoretical model should include complex N configurations, such as N-clusters, N–As split interstitials, N-antisites, and interstitial-N.

These studies would have not only a fundamental, but also a technological relevance. The presence of these states in the band gap may induce leakage and/or noise in devices such as MIR LEDs and photodetectors. On the other hand, these could also be exploited for exciting applications. The NDR that we observe is only weakly affected by temperature. The possibility of maintaining a pronounced and extended NDR at relatively high temperatures shows potential for non-linear components in electronics and MIR photonics applications. It would be interesting to correlate the features of the NDR with the N-content and

other growth conditions (such as growth temperature, rate and flux); these parameters could have a profound impact on the shape, range and temperature dependence of the NDR. Also, the quantum tunnelling of carriers through a defect can be employed for exciting applications such as random number generation and cryptography[182, 183].

Our In(AsN)/(InAl)As also emit luminescence in the MIR wavelength range λ = 3 - 5 μm. The defect states in the band gap seem to play a key role in the tuning of the EL emission under different applied biases at low temperature (T < 77 K). For this reason, it would also be interesting to find a correlation between the growth conditions and the EL emission in order to expand the accessible wavelength range. This could be achieved by monitoring the N-content and/or by controlling the carrier confinement, *i.e.* designing structures with different barrier or QW layer thickness. Our RTD structure also emits in the MIR range up to room temperature. The possibility to achieve up-converted MIR emission at room temperature is promising for applications in MIR photonics, such as for the design of novel and low-budget LEDs.

Appendix A

Electronic bound states in a quantum well

We consider the problem of electronic bound states in a quantum well (QW), *i.e.* a system consisting of a thin layer of material A of thickness a embedded between two layers of material B, acting as potential barriers (as depicted in Figure A.1a). The depth (V_0) of the QW is given by the discontinuity of the conduction band (CB) minima of the materials that constitute the QW layer and the barrier, *i.e.* $V_0 = E_C^B - E_C^A = \Delta E_C$. We calculate the electronic bound states in the QW by solving the time-independent Schrödinger equation in the effective-mass approximation:

$$-\frac{\hbar^2}{2m_e^*}\frac{d^2}{dz^2}\varphi(z) + V(z)\,\varphi(z) = \epsilon\,\varphi(z)\,, \qquad \text{(A.1)}$$

where m_e^* is the electron effective mass at the CB minimum of the QW, $V(z)$ is the potential profile and ϵ is the eigenvalue of the problem, providing the energy of the electron. In the following, we consider a spatial reference frame whose origin is set in the centre of the QW layer. The energy is set to zero at the CB minimum of the QW layer.

A simple solution is given by considering infinitely deep potential barriers, *i.e.* $V(z) = +\infty$ for $|z| > a/2$, and $V(z) = 0$ for$|z| < a/2$ (Figure A.1b). Since the infinite potential barrier prevents the motion of bound electrons outside the well, the wave function, $\varphi(z)$, has to vanish at the border of the QW.

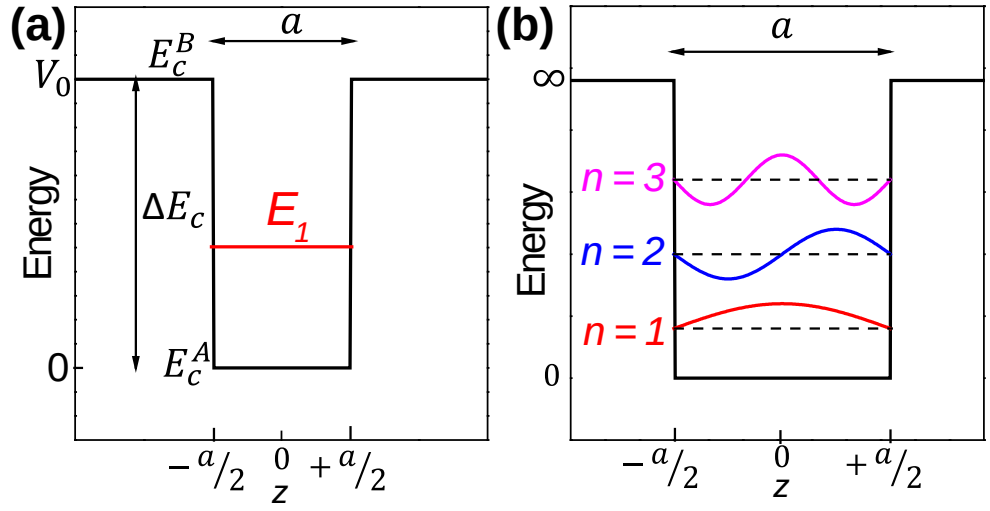


Figure A.1: **(a)** Profile of the conduction band minimum for a quantum well (QW). The red line shows the energy position of the first QW resonant state E_1. **(b)** Infinitely deep QW, showing a sketch of the first three quantized energy levels (black dashed lines) and the corresponding wave functions (coloured solid lines).

This gives the following boundary conditions: $\varphi(-a/2) = \varphi(a/2) = 0$. The solution of Schrödinger's equation in an infinitely deep QW are thus given by:

$$\phi_n(z) = \begin{cases} \sqrt{\frac{2}{a}}\cos\left(\frac{n\pi z}{a}\right) = \sqrt{\frac{2}{a}}\cos(kz), & n \text{ odd} \\ \sqrt{\frac{2}{a}}\sin\left(\frac{n\pi z}{a}\right) = \sqrt{\frac{2}{a}}\sin(kz), & n \text{ even} \end{cases} \tag{A.2}$$

with quantized energy labelled by the quantum number $n \geq 1$ (Figure A.1b):

$$\varepsilon_n = \frac{\hbar^2}{2m_e^*}\left(\frac{n\pi}{a}\right)^2. \tag{A.3}$$

Note that the solutions have even (odd) z-parity for odd (even) values of the quantum number n. Thus the electronic ground state in an infinitely deep QW has even parity. In spite of the unrealistic physical nature of the infinitely deep QW, Equations A.2 and A.3 are routinely used to solve quantum confinement problems in semiconductor heterostructures due to their simplicity.

A more realistic model considers a QW with a finite depth, V_0[77]. In this case, the electronic wave function can penetrate in the QW barriers. Thus no simple analytical solutions like those in Equation A.2 can be given for a QW with finite depth, but a numerical approach is required to calculate the eigenvalues, ϵ, of Equation A.1. Inside the well ($|z| < a/2$), $V(z) = 0$ and the eigenfunctions are similar to the infinitely deep QW case, with the same *z*-symmetry:

$$\phi_n(z) = C \begin{cases} \cos(kz) \\ \sin(kz) \end{cases}, \tag{A.4}$$

with energy $\varepsilon = \frac{\hbar^2 k^2}{2m_e^*}$. Outside the well ($|z| > a/2$), $V(z) = V_0 > \varepsilon$. The eigenfunctions are thus given by:

$$\phi_n(z) = D \exp(\pm \tilde{\kappa} z), \tag{A.5}$$

where $\frac{\hbar^2 \tilde{\kappa}^2}{2m_e^*} = V_0 - \varepsilon$ is the binding energy of the bound states, *i.e.* the energy required to enable a bound electron in the well to escape. Here C and D are normalization factors. In Equation A.5, the + sign holds for $z < 0$, while the – sign holds for $z > 0$; this is necessary for the normalization of the wave functions and thus to obtain physically meaningful solutions. In the following, we can focus only on $z > 0$, since we can calculate the wave functions for $z < 0$ from their symmetry.

We impose the continuity of the wave functions:

$$\phi\left(z = \tfrac{a}{2}\,|_-\right) = C \begin{cases} \cos(ka/2) \\ \sin(ka/2) \end{cases} = D \exp\left(-\tfrac{\tilde{\kappa} a}{2}\right) = \phi\left(z = \tfrac{a}{2}\,|_+\right), \tag{A.6}$$

and their first derivative:

$$\frac{d\phi}{dz}\left(z = \tfrac{a}{2}\,|_-\right) = Ck \begin{cases} -\sin(ka/2) \\ \cos(ka/2) \end{cases} = -D\tilde{\kappa} \exp\left(-\tfrac{\tilde{\kappa} a}{2}\right) = \frac{d\phi}{dz}\left(z = \tfrac{a}{2}\,|_+\right) \tag{A.7}$$

at $z = a/2$. By dividing (A.6) by (A.7), we eliminate the normalization factors, C and D, to obtain:

$$k\begin{cases}-\tan(ka/2)\\ \cot(ka/2)\end{cases} = -\tilde{\kappa}\,. \tag{A.8}$$

By expanding $\tilde{\kappa}$ and k as a function of V_0 and ε, Equation A.8 can be rewritten as the following transcendental equation:

$$\begin{cases}\tan(ka/2)\\ -\cot(ka/2)\end{cases} = \frac{\tilde{\kappa}}{k} = \sqrt{\frac{2m_e^* V_0}{\hbar^2 k^2} - 1}\,, \tag{A.9}$$

which needs to be solved numerically. By introducing the dimensionless variable $\theta = ka/2$, Equation A.9 can be rewritten as:

$$\begin{cases}\tan(\theta)\\ -\cot(\theta)\end{cases} = \sqrt{\left(\frac{\theta_0}{\theta}\right)^2 - 1}\,, \tag{A.10}$$

where the dimensionless parameter $\theta_0 = \sqrt{m_e^* V_0 a^2/2\hbar^2}$ incorporates all the physical input of the system, *i.e.* the electron effective mass m_e^*, and the QW depth, V_0, and width, a.

Note that the problem has to be treated in a different way if one wants to consider that the electron effective mass in the well, m_W^*, is different from the one in the barrier, m_B^*. This modifies the requirement for the continuity of the derivative of the wave function (Equation A.7) into:

$$\frac{1}{m_W^*}\frac{d\phi}{dz}\left(z = \frac{a}{2}\,|_-\right) = \frac{1}{m_B^*}\frac{d\phi}{dz}\left(z = \frac{a}{2}\,|_+\right). \tag{A.11}$$

This corresponds to:

$$\frac{Ck}{m_W^*}\begin{cases}-\sin(ka/2)\\ \cos(ka/2)\end{cases} = -\frac{D\tilde{\kappa}}{m_B^*}\exp\left(-\frac{\tilde{\kappa}a}{2}\right). \tag{A.12}$$

By dividing (A.6) by (A.12), Equation A.9 becomes:

$$\begin{cases}\tan(ka/2)\\ -\cot(ka/2)\end{cases} = \frac{m_W^*}{m_B^*}\frac{\tilde{\kappa}}{k} = \sqrt{\frac{m_W^*}{m_B^*}\left(\frac{2m_W^* V_0}{\hbar^2 k^2} - 1\right)}\,. \tag{A.13}$$

As before, $\theta = ka/2$ and $\theta_0 = \sqrt{m_W^* V_0 a^2/2\hbar^2}$, which only depends on the electron effective mass inside the well. Equation A.13 then becomes:

$$\begin{cases} \tan(\theta) \\ -\cot(\theta) \end{cases} = \sqrt{\frac{m_W^*}{m_B^*}\left(\frac{\theta_0}{\theta}\right)^2 - 1}\,. \qquad \text{(A.14)}$$

Here we solve Equation A.14 for an In(AsN) QW layer of thickness a = 10 nm embedded between two (InAl)As barriers (sketch in Figure A.2a). Equation A.14 can be solved graphically, as showed in Figure A.2b. The solutions are given by those values of θ for which the square root on the right side of Equation A.14 is equal to the tangent or the cotangent function; these points are indicated with the blue dots in FigureA.2b. Being the square root positive, only one solution between the tangent-like or the cotangent-like is allowed at a given θ. Also, no solution is allowed for $\theta > \theta_0$. Since the square root function intersects the θ-axis at $\theta = \theta_0$, while the tangent/cotangent functions intersect the θ-axis at $\theta = n\pi/2$ ($n \geq 0$), the number of the solutions (*i.e.* the number of the possible confined bound states in the QW) is given by $n^* = 2\theta_0/\pi$, rounded up to the next integer. This means that a square QW has always at least one bound state. In our case, we calculate two electronic bound states; however, as shown in Figure A.2a-b, the excited state has energy, E_2, very close to the QW barrier height, thus it is very easily excited out of the QW.

The same treatment can be applied to the holes confined in a QW in the valence band (VB). In this case, we use the heavy hole effective mass, m_{hh}^*, while the depth of the well is given by the discontinuity of the VB maxima in the two materials that constitute the semiconductor heterostructure, *i.e.* $V_0 = \Delta E_V$. For the CB and VB edge offsets, we use the same value as in reference [198]. The graphical solutions for the bound hole states in our In(AsN)/(InAl)As QW are reported in Figure A.2c.

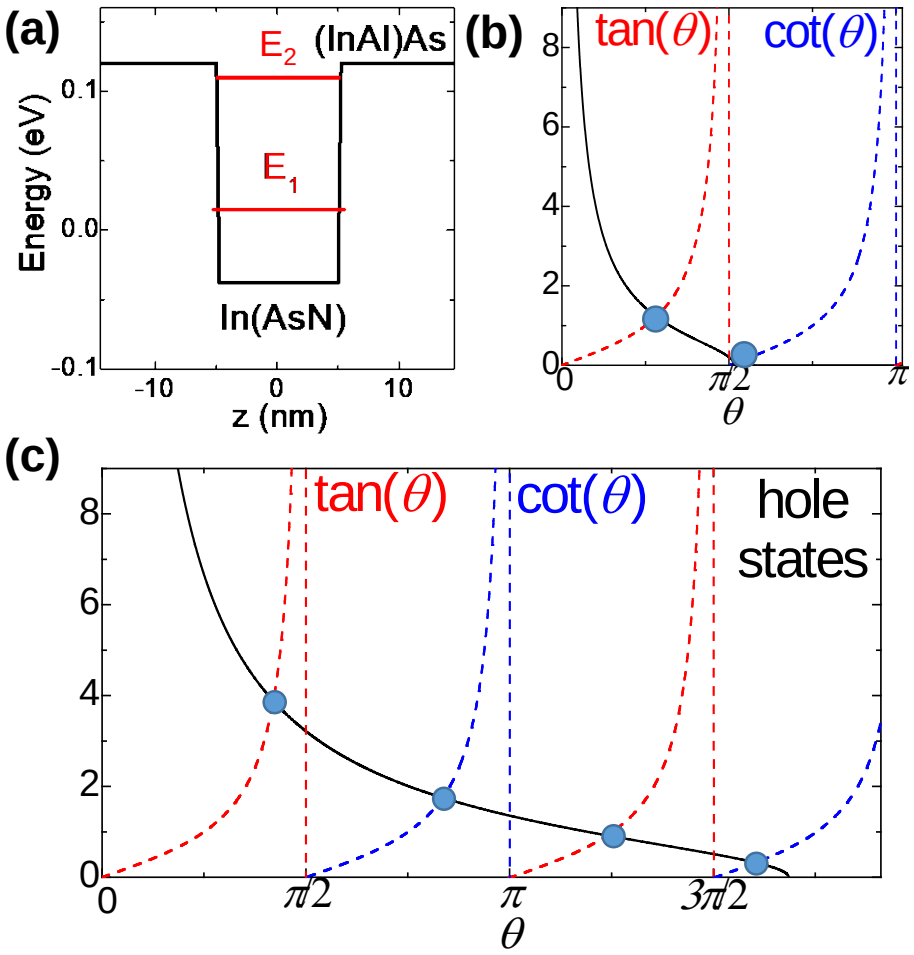


Figure A.2: (a) Profile of the conduction band minimum for an In(AsN)/(InAl)As QW. The red lines shows the energy position of the QW bound states. **(b)** Graphical solution for the electronic bound states in the CB; the blue dots represent the solution to the problem. **(c)** Graphical solution for the hole bound states in the VB; the blue dots represent the solution to the problem.

Appendix B

Laser induced lattice heating

Here we describe the temperature rise in an In(AsN):H lattice induced by a focused laser beam. Let us assume that the laser beam has a Gaussian intensity distribution (Figure B.1a):

$$I = I_0 \exp\left(-\frac{r^2}{w^2}\right) = I_0 \exp(-R^2)\,, \tag{B.1}$$

where r is the in-plane radial distance from the spot centre and w is the beam waist. In the following, z indicates the depth below the surface (Figure B.1b). Here, $R = r/w$ and $Z = z/w$ indicate the spatial coordinates in units of the beam waist.

The laser induced temperature rise can be written as[178]:

$$T(R, Z, W) = T_{max}\, N(R, Z, W) \tag{B.2}$$

where $T_{max} = T(0, 0, \infty)$ is the maximum temperature rise, $W = \alpha(\lambda)\, w$, $\alpha(\lambda)$ is the wavelength-dependent absorption coefficient, and $N(R, Z, W)$ is a normalization factor. T_{max} depends on the laser beam power, P, and waist, w, as well as on the temperature-dependent thermal conductivity, $K(T)$:

$$T_{max} = \frac{P}{2\sqrt{\pi}\, wK(T)}\,. \tag{B.3}$$

The maximum temperature rise is reached in the limit of large light absorption ($W = \infty$) on the surface ($Z = 0$) at the centre of the beam ($R = 0$), *i.e.* $N(0, 0, \infty) = 1$.

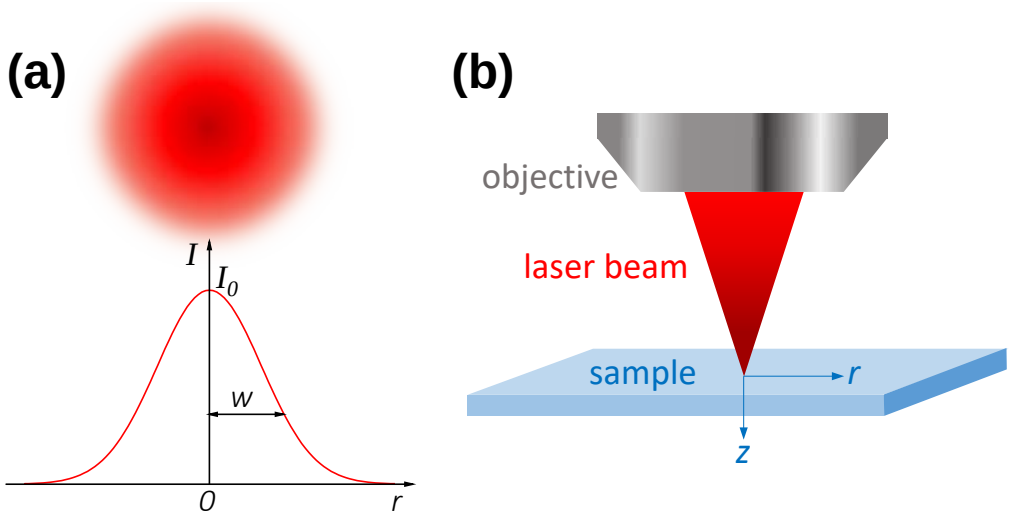


Figure B.1: a) Schematic of a laser spot and its intensity distribution along *r*. Here *w* is the beam waist. **b)** Sketch of the laser beam focused onto the sample.

For excitations over a finite depth, the temperature rise is less than unity:

$$N(0,0,W) = \left(\int_0^\infty I(\lambda)\frac{W}{W+\lambda}d\lambda\right)\left[\int_0^\infty I(\lambda)\,d\lambda\right]^{-1}. \qquad \text{(B.4)}$$

Here $I(\lambda)$ is the Bessel transform of $I(R)$:

$$I(\lambda) = \int_0^\infty I(R)\; J_0(\lambda R)\; R\; d\lambda\,, \qquad \text{(B.5)}$$

where $J_0(\lambda R)$ is the zeroth-order Bessel function of the first kind. For a Gaussian intensity distribution profile, $I(\lambda) = {}^1/_2\, exp\left(-{}^{\lambda^2}/_4\right)$ and $\int_0^\infty I(\lambda)\,d\lambda = {}^{\sqrt{\pi}}/_2$. The solution of Equation B.4 is given by:

$$N(0,0,W) = W\; D\left(\frac{W^2}{4}\right) - \frac{W^2}{2\pi^2}\exp\left(-\frac{W^2}{4}\right)\; Ei\left(\frac{W^2}{4}\right), \qquad \text{(B.6)}$$

where $D(x) = \exp(-x^2)\int_0^x exp(t^2)\,dt$ is the Dawson integral, $Ei(x) = P\int_{-\infty}^{x}\frac{exp(t)}{t}dt$ is the exponential integral, and *t* is the exposure time.

More generally, Equation B.7 gives the spatial distribution of the temperature rise considering the finite penetration (*i.e.* finite $W = \alpha w$) and the in-plane and depth deviations (*R* and *Z*) from the beam centre at the surface:

$$N(R,Z,W) = \frac{W}{\int_0^\infty I(\lambda)d\lambda} \times \int_0^\infty J_0(\lambda R)\, I(\lambda) \frac{W\, exp(-\lambda Z) - \lambda \exp(WZ)}{W^2+\lambda^2} d\lambda \ . \quad \text{(B.7)}$$

For $R, Z >> W^{-1}$ (*i.e.* for $r, z >> \alpha^{-1}$, the penetration depth of the impinging laser radiation), Equation B.7 gives:

$$\lim_{R,Z\to\infty} N(R,Z,W) = \frac{I(0)}{\int_0^\infty I(\lambda)d\lambda} \frac{1}{(R^2+Z^2)^{1/2}} = \frac{1}{\pi^{1/2}} \frac{1}{(R^2+Z^2)^{1/2}}, \quad \text{(B.8)}$$

where the last result yields for a Gaussian intensity distribution profile. Therefore, from Equations B.2 and B.8, the temperature rise can be expressed as:

$$T(R,Z,W) = \frac{P}{2\pi w K(T)} \frac{1}{(R^2+Z^2)^{1/2}}. \quad \text{(B.9)}$$

The parameters for In(AsN) used in our simulations are summarized in Table B.1.

Table B.1. Parameters used for our simulation of the temperature rise: the light absorption coefficient, α, at the wavelengths λ; the thermal conductivity, K, at T = 300 K; the beam waist, w, and the corresponding dimensionless parameter, $W = \alpha w$. The beam waist is estimated as $w = 1.22\ \lambda$ / NA, where NA (= 0.8) is the numerical aperture of our 100× objective.

λ [nm]	α [m^{-1}] [199]	K [W m^{-1} K^{-1}] [200]	w [μm]	$W = \alpha w$
532	2.3×10^7	27	0.8	18
633	1.2×10^7		1	12

Bibliography

1. Capasso, F., *Band-Gap Engineering: From Physics and Materials to New Semiconductor Devices.* Science, 1987. **235**(4785): p. 172.
2. Jaros, M., *Concepts and Applications of Band Structure Engineering in Optoelectronics*. Low-Dimensional Structures in Semiconductors: From Basic Physics to Applications, ed. A.R. Peaker and H.G. Grimmeiss. 1991, Boston, MA: Springer US. 147-163.
3. Capasso, F. and A.Y. Cho, *Bandgap engineering of semiconductor heterostructures by molecular beam epitaxy: physics and applications.* Surface Science, 1994. **299-300**: p. 878-891.
4. Ning, C.-Z., L. Dou, and P. Yang, *Bandgap engineering in semiconductor alloy nanomaterials with widely tunable compositions.* Nature Reviews Materials, 2017. **2**: p. 17070.
5. Koenraad, P.M. and M.E. Flatté, *Single dopants in semiconductors.* Nature Materials, 2011. **10**: p. 91.
6. Schubert, E.F., *Doping in III-V Semiconductors*, ed. C.U. Press. 1993, Cambridge, UK.
7. Buyanova, I.A. and W.M. Chen, *Physics and applications of dilute nitrides*. 2004, New York Taylor & Francis.
8. Henini, M., *Dilute Nitride Semiconductors*. 2005: Elsevier Science.
9. Shih, D.-K., et al., *Band Gap Reduction in InAsN Alloys.* Jpn. J. Appl. Phys. Vol., 2003. **42**: p. 375-383.
10. Veal, T.D., et al., *Photoluminescence spectroscopy of bandgap reduction in dilute InNAs alloys.* Appl. Phys. Lett., 2005. **87**: p. 182114.
11. Zhuang, Q., A. Godenir, and A. Krier, *Photoluminescence in InAsN epilayers grown by molecular beam epitaxy.* J. Phys. D: Appl. Phys., 2008. **41**: p. 132002.
12. Kudrawiec, R., et al., *Photoreflectance study of the energy gap and spin-orbit splitting in InNAs alloys.* Appl. Phys. Lett., 2009. **94**: p. 151902.
13. Shan, W., et al., *Band Anticrossing in GaInNAs Alloys.* Phys. Rev. Lett., 1999. **82**: p. 1221-1224.

14. Wu, J., W. Shan, and W. Walukiewicz, *Band anticrossing in highly mismatched III–V semiconductor alloys.* Semicond. Sci. Technol. , 2002. **17** p. 860-869.
15. Shan, W., et al., *Band anticrossing in dilute nitrides.* J. Phys.: Condens. Matter, 2004. **16**: p. 3355-3372.
16. Lindsay, A. and E.P. O'Reilly, *Unification of the Band Anticrossing and Cluster-State Modelsof Dilute Nitride Semiconductor Alloys.* Phys. Rev. Lett., 2004. **93**: p. 196402.
17. López, N., et al., *Engineering the Electronic Band Structure for Multiband Solar Cells.* Physical Review Letters, 2011. **106**(2): p. 028701.
18. Krier, A., et al., *InAs-based dilute nitride materials and devices for the mid-infrared spectral range.* SPIE Proceedings, 2013. **8631**: p. 86311Q-1.
19. Janotti, A., et al., *Effects of Hydrogen on the Electronic Properties of Dilute GaAsN Alloys.* Phys. Rev. Lett., 2002. **89**(8): p. 086403.
20. Fowler, W.B., et al., *Structure and vibrational properties of N-H_2 complexes in GaAs:N.* Physical Review B, 2005. **72**(3): p. 035208.
21. Du, M.-H., S. Limpijumnong, and S.B. Zhang, *Hydrogen pairs and local vibrational frequencies in H-irradiated $GaAs_{1-y}N_y$.* Physical Review B, 2005. **72**(7): p. 073202.
22. Wen, L., et al., *Detailed structure of the H-N-H center in $GaAs_yN_{1-y}$ revealed by vibrational spectroscopy under uniaxial stress.* Physical Review B, 2010. **81**(23): p. 233201.
23. Bissiri, M., et al., *Role of N clusters in $In_xGa_{1-x}As_{1-y}N_y$ band-gap reduction.* Physical Review B, 2002. **66**(3): p. 033311.
24. Berti, M., et al., *Formation and dissolution of D-N complexes in dilute nitrides.* Physical Review B, 2007. **76**(20): p. 205323.
25. Bisognin, G., et al., *High-resolution X-ray diffraction in situ study of very small complexes: The case of hydrogenated dilute nitrides*. Vol. 41. 2008. 366-372.
26. Balakrishnan, N., et al., *Laser writing of the electronic activity of N- and H-atoms in GaAs.* Applied Physics Letters, 2011. **99**(2): p. 021105.

27. Balakrishnan, N., et al., *Band-gap profiling by laser writing of hydrogen-containing III-N-Vs.* Physical Review B, 2012. **86**(15): p. 155307.
28. Trotta, R., A. Polimeni, and M. Capizzi, *Hydrogen Incorporation in III-N-V Semiconductors: From Macroscopic to Nanometer Control of the Materials' Physical Properties.* Advanced Functional Materials, 2012. **22**(9): p. 1782-1801.
29. Ciatto, G., *Hydrogenated Dilute Nitride Semiconductors - Theory, properties and Applications*. 2015, Singapore: Pan Stanford Publishing.
30. Birindelli, S., et al., *Peculiarities of the hydrogenated In(AsN) alloy.* Semicond. Sci. Technol., 2015. **30**(10): p. 105030.
31. Kozlova, N.V., et al., *Nonresonant hydrogen dopants in In(AsN): A route to high electron concentrations and mobilities.* Phys. Rev. B, 2013. **87**: p. 165207.
32. Velichko, A.V., et al., *H-tailored surface conductivity in narrow band gap In(AsN).* Appl. Phys. Lett., 2015. **106**: p. 022111.
33. *http://ec.europa.eu/growth/industry/policy/key-enabling-technologies_en*.
34. *Postgraduate Research on Dilute Metamorphic Nanostructures and Metamaterials in Semiconductor Photonics (PROMIS) - Marie Skłodowska-Curie Innovative Training Network (ITN) Agreement (**2015**)*. 2015.
35. Kleine-Ostmann, T. and T. Nagatsuma, *A Review on Terahertz Communications Research.* Journal of Infrared, Millimeter, and Terahertz Waves, 2011. **32**(2): p. 143-171.
36. John, F.F., et al., *THz imaging and sensing for security applications—explosives, weapons and drugs.* Semiconductor Science and Technology, 2005. **20**(7): p. S266.
37. Liu, H., et al., *Terahertz Spectroscopy and Imaging for Defense and Security Applications.* Proceedings of the IEEE, 2007. **95**(8): p. 1514-1527.
38. Tanabe, K., *A Review of Ultrahigh Efficiency III-V Semiconductor Compound Solar Cells: Multijunction Tandem, Lower Dimensional,*

Photonic Up/Down Conversion and Plasmonic Nanometallic Structures. Energies, 2009. **2**(3).

39. Nozik, A.J., et al., *Semiconductor Quantum Dots and Quantum Dot Arrays and Applications of Multiple Exciton Generation to Third-Generation Photovoltaic Solar Cells.* Chemical Reviews, 2010. **110**(11): p. 6873-6890.
40. Obama, B., *The irreversible momentum of clean energy.* Science, 2017.
41. Yamazoe, N. and N. Miura, *Environmental gas sensing.* Sensors and Actuators B: Chemical, 1994. **20**(2): p. 95-102.
42. Duk-Dong, L. and L. Dae-Sik, *Environmental gas sensors.* IEEE Sensors Journal, 2001. **1**(3): p. 214-224.
43. Lewicki, R., et al., *Current Status of Mid-infrared Semiconductor-Laser-based Sensor Technologies for Trace-Gas Sensing Applications*. 2013: SPIE Press Book.
44. Yin, Z. and X. Tang, *A review of energy bandgap engineering in III–V semiconductor alloys for mid-infrared laser applications.* Solid-State Electronics, 2007. **51**: p. 6-15.
45. Pereira, M.F., *TERA-MIR radiation: materials, generation, detection and applications.* Optical and Quantum Electronics, 2014. **46**(4): p. 491-493.
46. Töpfer, T., et al., *Room-temperature mid-infrared laser sensor for trace gas detection.* Applied Optics, 1997. **36**(30): p. 8042-8049.
47. Kosterev, A., et al., *Application of quantum cascade lasers to trace gas analysis.* Applied Physics B, 2008. **90**(2): p. 165-176.
48. Tittel, F.K., et al., *Emerging Infrared Laser Absorption Spectroscopic Techniques for Gas Analysis*. Trace Analysis of Specialty and Electronic Gases. 2013: Wiley Online Library.
49. Barho, F.B., et al., *All-semiconductor plasmonic gratings for biosensing applications in the mid-infrared spectral range.* Optics Express, 2016. **24**(14): p. 16175-16190.
50. Barho, F.B., et al., *Highly doped semiconductor plasmonic nanoantenna arrays for polarization selective broadband surface-enhanced infrared absorption spectroscopy of vanillin.* Journal of Nanophotonics, 2018. **7**(2): p. 507-516.

51. Capasso, F., *High-performance midinfrared quantum cascade lasers.* Optical Engineering, 2010. **49**: p. 111102.
52. Faist, J., et al., *Quantum Cascade Laser*. Vol. 264. 1994. 553-556.
53. Faist, J., *Quantum Cascade Lasers*. 2013: Oxford University Press.
54. Tredicucci, A., et al., *Terahertz quantum cascade lasers—first demonstration and novel concepts.* Semiconductor Science and Technology, 2005. **20**(7): p. S222.
55. Yang, R.Q., *Infrared laser based on intersubband transitions in quantum wells.* Superlattices and Microstructures, 1995. **17**(1): p. 77-83.
56. Meyer, R., et al., *Type-II and type-I interband cascade lasers*. Vol. 32. 1996. 45-46.
57. Li, L., et al., *Low-threshold InAs-based interband cascade lasers operating at high temperatures.* Applied Physics Letters, 2015. **106**(25): p. 251102.
58. Rui, Q.Y., *InAs-based quantum cascade lasers with enhanced confinement.* Semiconductor Science and Technology, 2015. **30**(10): p. 105023.
59. Wysocki, G., et al., *Widely tunable mode-hop free external cavity quantum cascade laser for high resolution spectroscopic applications.* Applied Physics B, 2005. **81**(6): p. 769-777.
60. Wysocki, G., et al., *Widely tunable mode-hop free external cavity quantum cascade lasers for high resolution spectroscopy and chemical sensing.* Applied Physics B, 2008. **92**(3): p. 305-311.
61. Höfling, S., et al. *Interband cascade lasers for the mid-infrared spectral region*. in *SPIE OPTO*. 2014. SPIE.
62. Matveev, B.A., et al., *Mid-infrared (3-5 μm) LEDs as sources for gas and liquid sensors.* Sensors and Actuators B: Chemical, 1997. **39**(1): p. 339-343.
63. Krier, A., et al., *The development of room temperature LEDs and lasers for the mid-infrared spectral range.* physica status solidi (a), 2008. **205**(1): p. 129-143.
64. O'Brien, K., et al., *Carrier recombination mechanisms in mid-infrared GaInAsSb quantum well lasers.* physica status solidi (b), 2007. **244**(1): p. 203-207.

65. Krier, A., et al., *Development of dilute nitride materials for mid-infrared diode lasers.* Semicond. Sci. Technol., 2012. **27**: p. 094009.
66. Underwood, K.J., et al. *Auger Recombination in Mid-Infrared Active Regions*. in *Conference on Lasers and Electro-Optics*. 2018. San Jose, California: Optical Society of America.
67. Krishna, S. *Antimonide Based Photonic Infrared Detectors*. in *Photonics on the Lake* 2018. Windermere (UK).
68. Zhang, S.B., *The microscopic origin of the doping limits in semiconductors and wide-gap materials and recent developments in overcoming these limits: a review*. Journal of Physics: Condensed Matter, 2002. **14**(34): p. R881.
69. Wolfe, C.M. and G.E. Stillman, *Self-compensation of donors in high-purity GaAs.* Appl. Phys. Lett., 1975. **27**(10): p. 564-567.
70. Luz, D.M., S.S. Makler, and E.V. Anda, *The compensation effect in the impurity band of doped semiconductors.* J. Phys. C: Solid State Phys., 1988. **21**: p. 5149-5162.
71. Sealy, B.J., *Review of III-V semiconductor materials and devices.* Journal of the Institution of Electronic and Radio Engineers, 1987. **57**(1): p. S2.
72. Grosso, G. and G. Parravicini, *Solid State Physics*. 2000: Academic Press.
73. Blakemore, J.S., *Semiconducting and other major properties of gallium arsenide.* Journal of Applied Physics, 1982. **53**(10): p. R123-R181.
74. Goldammer, K.J., et al., *High-mobility electron systems in remotely-doped InSb quantum wells.* Journal of Crystal Growth, 1999. **201-202**: p. 753-756.
75. Rodilla, H., et al., *High-mobility heterostructures based on InAs and InSb: A Monte Carlo study.* Journal of Applied Physics, 2009. **105**(11): p. 113705.
76. Frensley, W.R. and N.G. Einspruch, *Heterostructures and Quantum Devices*. 1994, San Diego: Academic Press.
77. Davies, J.H., *The Physics of Low-dimensional semiconductors - An Introduction*. 1998, New York, NY, USA: Cambridge University Press.

78. Brunner, K., et al., *Sharp-Line Photoluminescence and Two-Photon Absorption of Zero-Dimensional Biexcitons in a GaAs/AlGaAs Structure.* Physical Review Letters, 1994. **73**(8): p. 1138-1141.
79. Černe, J., et al., *Terahertz Dynamics of Excitons in GaAs/AlGaAs Quantum Wells.* Physical Review Letters, 1996. **77**(6): p. 1131-1134.
80. Toshiaki, F., L.I.K. Keisuke, and N. Hisao, *Photoluminescence from AlGaAs-GaAs Single Quentum Wells with Growth Interrupted Heterointerfaces Grown by Molecular Beam Epitaxy.* Japanese Journal of Applied Physics, 1985. **24**(7A): p. L510.
81. Satoshi, H., et al., *Room-Temperature Mobility of Two-Dimensional Electron Gas in Selectively Doped GaAs/ N -AlGaAs Heterojunction Structures.* Japanese Journal of Applied Physics, 1981. **20**(5): p. L378.
82. Gonzalez, E.M., Y. Lin, and E.E. Mendez, *Magnetotunneling in a two-dimensional electron-hole system near equilibrium.* Phys. Rev. B, 2000. **63** p. 033308.
83. Fu, Y., T.H. Wang, and M. Willander, *Designing two-dimensional electron gases in GaAs/InGaAs/AlGaAs, δ-doped AlGaAs/GaAs, and AlGaAs/InGaAs/GaAs heterostructures for single electron transistor application.* Journal of Applied Physics, 2001. **89**(3): p. 1759-1763.
84. Solomon, P.M. and H. Morkoc, *Modulation-doped GaAs/AlGaAs heterojunction field-effect transistors (MODFET's), ultrahigh-speed device for supercomputers.* IEEE Transactions on Electron Devices, 1984. **31**(8): p. 1015-1027.
85. Hatami, F., et al., *Carrier dynamics in type-II GaSb/GaAs quantum dots.* Physical Review B, 1998. **57**(8): p. 4635-4641.
86. Laghumavarapu, R.B., et al., *GaSb/GaAs type II quantum dot solar cells for enhanced infrared spectral response.* Applied Physics Letters, 2007. **90**(17): p. 173125.
87. Hatami, F., et al., *Radiative recombination in type-II GaSb/GaAs quantum dots.* Applied Physics Letters, 1995. **67**(5): p. 656-658.
88. Singh, J., *Electronic and Optoelectronic Properties of Semiconductor Structures*. 2003: Cambridge University Press.
89. Muralidharan, P., et al. *Modeling of InAs/GaSb tunnel junction*. in *2012 38th IEEE Photovoltaic Specialists Conference*. 2012.

90. Knoch, J. and J. Appenzeller, *Modeling of High-Performance p-Type III–V Heterojunction Tunnel FETs.* IEEE Electron Device Letters, 2010. **31**(4): p. 305-307.
91. Zhou, G., et al. *Novel gate-recessed vertical InAs/GaSb TFETs with record high ION of 180 μA/μm at VDS = 0.5 V*. in *2012 International Electron Devices Meeting*. 2012.
92. Kuech, T.F., *III-V compound semiconductors: Growth and structures.* Progress in Crystal Growth and Characterization of Materials, 2016. **62**(2): p. 352-370.
93. Erol, A., *Dilute III-V Nitride Semiconductors and Material Systems: Physics and Technology*. 2008: Springer.
94. Weyers, M., M. Sato, and H. Ando, *Red Shift of Photoluminescence and Absorption in Dilute GaAsN Alloy Layers.* Japanese Journal of Applied Physics, 1992. **31**(7A): p. L853.
95. Fang, Z.M., et al., *Photoluminescence of InSb, InAs, and InAsSb grown by organometallic vapor phase epitaxy*. Journal of Applied Physics, 1990. **67**(11): p. 7034-7039.
96. Madelung, O., *Semiconductors: Data Handbook*. 2004: Springer.
97. Drachenko, O., et al., *Cyclotron resonance mass and Fermi energy pinning in the In(AsN) alloy.* Appl. Phys. Lett., 2011. **98**: p. 162109.
98. Bi, W.G. and C.W. Tu, *Bowing parameter of the band-gap energy of GaNxAs1−x.* Applied Physics Letters, 1997. **70**(12): p. 1608-1610.
99. O'Reilly, E.P., et al., *Trends in the electronic structure of dilute nitride alloys.* Semicond. Sci. Technol., 2009. **24**: p. 033001.
100. Talwar, D.N., *Novel Dilute III–V-Ns : From Physics to Applications.* International Conference on Emerging Trends in Electronic and Photonic Devices & Systems, 2009.
101. Vurgaftman, I. and J.R. Meyer, *Band parameters for nitrogen-containing semiconductors.* J. Appl. Phys., 2003. **94**: p. 3675-3696.
102. J. Ibáñez, et al., *Structural and optical properties of dilute InAsN grown by molecular beam epitaxy.* J. Appl. Phys., 2010. **108**: p. 103504.
103. Lindsay, A. and E.P. O'Reilly, *Theory of enhanced bandgap non-parabolicity in GaN_xAs_{1-x} and related alloys.* Solid State Communications, 1999. **112**: p. 443-447.

104. Wu, J., W. Walukiewicz, and E.E. Haller, *Band structure of highly mismatched semiconductor alloys: Coherent potential approximation.* Physical Review B, 2002. **65**(23): p. 233210.

105. Van de Walle, C.G. and J. Neugebauer, *Universal alignment of hydrogen levels in semiconductors, insulators and solutions.* Nature, 2003. **423**: p. 626.

106. Clerjaud, B., *Unintentional hydrogen incorporation in crystals.* Physica B: Condensed Matter, 1991. **170**(1): p. 383-391.

107. Ren, F., *Sources of Hydrogen in III-V Device Processing.* Materials Science Forum, 1994. **148-149**: p. 141-158.

108. Pankove, J.I. and N.M. Johnson, *Hydrogen in Semiconductors (Semiconductors and Semimetals)*. Vol. 34. 1991: Boston: Academic.

109. J.Pearton, S., J.W. Corbett, and M. Stavola, *Hydrogen in Crystalline Semiconductors*. 1992: Springer Series in Materials Science.

110. Nickel, N.H., *Hydrogen in Semiconductors II (Semiconductors and Semimetals)*. Vol. 61. 1999: Boston: Academic.

111. Nielsen, K.B., et al., *Bond-centered hydrogen in silicon studied by in situ deep-level transient spectroscopy.* Physical Review B, 1999. **60**(3): p. 1716-1728.

112. Nielsen, K.B., et al., *Acceptor state of monoatomic hydrogen in silicon and the role of oxygen.* Physical Review B, 2002. **65**(7): p. 075205.

113. Elias, D.C., et al., *Control of Graphene's Properties by Reversible Hydrogenation: Evidence for Graphane.* Science, 2009. **323**(5914): p. 610-613.

114. Teukam, Z., et al., *Shallow donors with high n-type electrical conductivity in homoepitaxial deuterated boron-doped diamond layers.* Nature Materials, 2003. **2**: p. 482.

115. Limpijumnong, S. and C.G. Van de Walle, *Passivation and Doping due to Hydrogen in III-Nitrides.* physica status solidi (b), 2001. **228**(1): p. 303-307.

116. Pettinari, G., et al., *Experimental evidence of different hydrogen donors in n-type InN.* Physical Review B, 2008. **77**(12): p. 125207.

117. Myers, S.M., et al., *Diffusion, release, and uptake of hydrogen in magnesium-doped gallium nitride: Theory and experiment.* Journal of Applied Physics, 2001. **89**(6): p. 3195-3202.

118. De Luca, M., et al., *Identification of four-hydrogen complexes in In-rich $In_xGa_{1-x}N$ alloys using photoluminescence, x-ray absorption, and density functional theory.* Physical Review B, 2012. **86**(20): p. 201202.

119. Breuer, S.J., et al., *Interstitial hydrogen and enhanced dissociation of C-H complexes in GaAs.* Physical Review B, 1996. **53**(24): p. 16289-16296.

120. Amore Bonapasta, A., M. Capizzi, and P. Giannozzi, *Structure, kinetics, and passivation of hydrogen-acceptor complexes in gallium arsenide: A theoretical study.* Physical Review B, 1998. **57**(20): p. 12923-12931.

121. Ashwin, M.J., et al., *Carbon acceptors passivated with hydrogen and the search for carbon donors in highly doped GaAs:C.* Semiconductor Science and Technology, 1993. **8**(5): p. 625.

122. Kozuch, D.M., et al., *Hydrogen in carbon-doped GaAs grown by metalorganic molecular beam epitaxy.* Applied Physics Letters, 1990. **57**(24): p. 2561-2563.

123. Ashwin, M.J., et al., *The bonding of CAs acceptors in $In_xGa_{1-x}As$ grown by chemical beam epitaxy using carbon tetrabromide as the source of carbon.* Journal of Applied Physics, 1996. **80**(12): p. 6754-6760.

124. Capizzi, M., et al., *Hydrogen activated radiative states in GaAs/GaAlAs heterostructures and InGaAs/GaAs multiquantum wells.* Journal of Applied Physics, 1992. **72**(4): p. 1454-1459.

125. Amore Bonapasta, A., M. Capizzi, and P. Giannozzi, *Near-Edge States Induced by Hydrogen Inclusion in Gallium Arsenide.* physica status solidi (b), 1998. **210**(2): p. 277-282.

126. Capizzi, M., et al., *Hydrogen-donor-induced free-exciton splitting in GaAs.* Physical Review B, 1993. **47**(19): p. 12563-12567.

127. Pettinari, G., et al., *Hydrogen effects in dilute III-N-V alloys: From defect engineering to nanostructuring.* Journal of Applied Physics, 2014. **115**(1): p. 012011.

128. Felici, M., et al., *In-Plane Bandgap Engineering by Modulated Hydrogenation of Dilute Nitride Semiconductors.* Advanced Materials, 2006. **18**(15): p. 1993-1997.
129. Birindelli, S., et al., *Single Photons on Demand from Novel Site-Controlled GaAsN/GaAsN:H Quantum Dots.* Nano Letters, 2014. **14**(3): p. 1275-1280.
130. Balakrishnan, N., et al., *Tunable spectral response by hydrogen irradiation of Ga(AsN) superlattice diodes.* Appl. Phys. Lett., 2014. **104**(24): p. 242110.
131. Ciatto, G., et al., *Nitrogen-hydrogen complex in $GaAs_xN_{1-x}$ revealed by x-ray absorption spectroscopy.* Physical Review B, 2005. **71**(20): p. 201301.
132. Sze, S.M., *Physics of Semiconductor Devices*, ed. Wiley. 1981, New York.
133. King, P.D.C., et al., *Surface Band-Gap Narrowing in Quantized Electron Accumulation Layers.* Phys. Rev. Lett., 2010. **104**(25): p. 256803.
134. Li, D. and C.Z. Ning, *All-semiconductor active plasmonic system in mid-infrared wavelengths.* Optics Express, 2011. **19**(15): p. 14594-14603.
135. Zener, C., *A Theory of the Electrical Breakdown of Solid Dielectrics.* Proc. R. Soc. London, 1934. **145**: p. 523-529.
136. Esaki, L., *New Phenomenon in Narrow Germanium p-n Junctions.* Phys. Rev., 1958. **109**: p. 603-604.
137. Horowitz, P. and W. Hill, *The Art of Electronics - 2nd Edition*, ed. C.U. Press. 1989: Cambridge University Press.
138. Kane, E.O., *Zener tunneling in semiconductors.* Journal of Physics and Chemistry of Solids, 1960. **12**(2): p. 181-188.
139. Fredkin, D.R. and G.H. Wannier, *Theory of Electron Tunneling in Semiconductor Junctions.* Physical Review, 1962. **128**(5): p. 2054-2061.
140. Tiemann, J.J. and H. Fritzsche, *Theory of Indirect Interband Tunneling in Semiconductors.* Physical Review, 1965. **137**(6A): p. A1910-A1913.
141. Vandenberghe, W., et al., *Zener tunneling in semiconductors under nonuniform electric fields.* Journal of Applied Physics, 2010. **107**(5): p. 054520.

142. Kane, E.O., *Theory of Tunneling.* Journal of Applied Physics, 1961. **32**(1): p. 83-91.
143. Di Paola, D.M., et al., *Resonant Zener tunnelling via zero-dimensional states in a narrow gap diode.* Sci. Rep., 2016. **6**: p. 32039.
144. Zheng, J.F., et al., *Scanning Tunneling Microscopy Studies of Si Donors (Si_{Ga}) in GaAs.* Phys. Rev. Lett. , 1994. **72**: p. 1490-1493.
145. Sakai, J.W., et al., *Probing the wave function of quantum confined states by resonant magnetotunneling.* Physical Review B, 1993. **48**(8): p. 5664-5667.
146. Narihiro, M., et al., *Resonant tunneling of electrons via 20 nm scale InAs quantum dot and magnetotunneling spectroscopy of its electronic states.* Appl. Phys. Lett. , 1997. **70**: p. 105.
147. Vdovin, E.E., et al., *Imaging the Electron Wave Function in Self-Assembled Quantum Dots.* Science 2000. **290** p. 122-124
148. Patanè, A., et al., *Probing the quantum states of self-assembled InAs dots by magnetotunneling spectroscopy.* Phys. Rev. B, 2002. **65**: p. 165308.
149. Maier, S.A., *Plasmonics: Fundamentals and Applications*. 2007, New York, NY, USA: Springer.
150. Naik, G.V., V.M. Shalaev, and A. Boltasseva, *Alternative Plasmonic Materials: Beyond Gold and Silver*. Advanced Materials, 2013. **25**(24): p. 3264-3294.
151. West, P.R., et al., *Searching for better plasmonic materials.* Laser Photonics Rev. , 2010. **4**(6): p. 795-808.
152. Scotognella, F., et al., *Plasmonics in heavily-doped semiconductor nanocrystals.* The European Physical Journal B, 2013. **86**(4): p. 154.
153. Henini, M. and M. Razeghi, *Handbook of infrared detection technologies*, ed. Elsevier. 2002, Oxford (UK): Elsevier.
154. Han, Z., et al., *On-chip mid-infrared gas detection using chalcogenide glass waveguide.* Appl. Phys. Lett., 2016. **108**(14): p. 141106.
155. Milla, M.J., et al., *Localized surface plasmon resonance frequency tuning in highly doped InAsSb/GaSb one-dimensional nanostructures.* Nanotechnology, 2016 **27**: p. 425201.
156. Boltasseva, A. and H.A. Atwater, *Low-Loss Plasmonic Metamaterials.* Science, 2011. **331**: p. 290-291.

157. Naik, G.V. and A. Boltasseva, *Semiconductors for plasmonics and metamaterials.* physica status solidi (RRL) – Rapid Research Letters, 2010. **4**(10): p. 295-297.
158. Naik, G.V. and A. Boltasseva, *A comparative study of semiconductor-based plasmonic metamaterials.* Metamaterials, 2011. **5**(1): p. 1-7.
159. Sachet, E., et al., *Dysprosium-doped cadmium oxide as a gateway material for mid-infrared plasmonics.* Nat Mater, 2015. **14**(4): p. 414-420.
160. Schuller, J.A., et al., *Dielectric Metamaterials Based on Electric and Magnetic Resonances of Silicon Carbide Particles.* Phys. Rev. Lett., 2007. **99**(10): p. 107401.
161. Hoffman, A.J., et al., *Negative refraction in semiconductor metamaterials.* Nat. Mater., 2007. **6**(12): p. 946-950.
162. Taliercio, T., et al., *Brewster "mode" in highly doped semiconductor layers: an all-optical technique to monitor doping concentration.* Opt. Express, 2014. **22**: p. 24294-24303.
163. Zhong, Y., et al., *Review of mid-infrared plasmonic materials.* Journal of Nanophotonics, 2015. **9**(1): p. 093791-093791.
164. Tokumitsu, E., *Correlation between Fermi Level Stabilization Positions and Maximum Free Carrier Concentrations in III–V Compound Semiconductors.* Japanese Journal of Applied Physics, 1990. **29**(5A): p. L698.
165. Law, S., et al., *Mid-infrared designer metals.* Optics Express, 2012. **20**(11): p. 12155-12165.
166. Di Paola, D.M., et al., *Optical Detection and Spatial Modulation of Mid-Infrared Surface Plasmon Polaritons in a Highly Doped Semiconductor.* Advanced Optical Materials, 2018. **6**(3): p. 1700492.
167. Houzay, F., et al., *First stages of the MBE growth of InAs on (001)GaAs.* Journal of Crystal Growth, 1987. **81**(1): p. 67-72.
168. *HR800 User Manual, Horiba Jobin Yvon.*
169. *JEOL JSM-7100F FEGSEM, User Manual.*
170. *Murano 525 Gathan heating stage, User Manual.*
171. Hamaguchi, C., *Basic Semiconductor Physics*, ed. Springer-Verlag. 2006, London: Springer-Verlag.

172. Patanè, A., et al., *Effect of Low Nitrogen Concentrations on the Electronic Properties of $InAs_{1-x}N_x$.* Phys. Rev. B, 2009. **80**: p. 115207.
173. Buchner, S. and E. Burstein, *Raman Scattering by Wave-Vector-Dependent LO-Phonon-Plasmon Modes in n-InAs.* Phys. Rev. Lett., 1974. **33**(15): p. 908-911.
174. Li, Y.B., et al., *Raman scattering by plasmon-phonon modes in highly doped n-InAs grown by molecular beam epitaxy.* Semicond. Sci. Technol., 1992. **7**(9): p. 1149.
175. Palik, E.D. and J.K. Furdyna, *Infrared and microwave magnetoplasma effects in semiconductors.* Rep. Prog. Phys., 1970. **33**(13): p. 1193.
176. Mead, C.A. and W.Q. Spitzer, *Fermi level position at semiconductor surfaces.* Phys. Rev. Lett., 1963. **10**: p. 471.
177. Cowley, R.A. and G. Dolling, *Conduction Electrons and Optic Modes of Ionic Crystals.* Phys. Rev. Lett., 1965. **14**(14): p. 549-551.
178. Lax, M., *Temperature rise induced by a laser beam.* Journal of Applied Physics, 1977. **48**(9): p. 3919-3924.
179. Okhotin, A.S., A.S. Pushkarskii, and V.V. Gorbachev, *Thermophysteal Properties of Semiconductors*, ed. A.P. House. 1972, Moscow.
180. Katsnelson, M.I., K.S. Novoselov, and A.K. Geim, *Chiral tunneling and the Klein paradox in graphene.* Nature Phys. 2, 2006: p. 620-625.
181. Klein, O., *Die Reflexion von Elektronen an einem Potentialsprung nach der relativistischen Dynamik von Dirac.* Z. Phys., 1929. **53**: p. 157-165.
182. Gavito, R.B., et al. *N-state random switching based on quantum tunnelling*. in *SPIE Nanoscience + Engineering*. 2017. SPIE.
183. Bernardo-Gavito, R., et al., *Extracting random numbers from quantum tunnelling through a single diode.* Sci. Rep., 2017. **7**(1): p. 17879.
184. Esaki, L., et al., *Esaki diodes live and learn.* Proc. Jpn. Acad., Ser. B, 2010. **86**: p. 451-453.
185. Kuan, C.H., et al., *Analysis of the dark current in the bulk of InAs diode detectors.* J. Appl. Phys., 1996. **80**: p. 5454-5458.
186. Morifuji, M., et al., *Resonant effect of Zener tunneling current.* Phys. Rev. B, 2002. **65**: p. 233308.

187. Kyriakou, I., J.H. Jefferson, and C.J. Lambert, *Suppression of thermal broadening via Zener tunneling in narrow-gap semiconductor double-quantum-wire structures.* Applied Physics Letters, 2010. **96**: p. 232104

188. Veiler, M.H., W. Zawadzki, and B. Lax, *Theory of Tunneling, Including Photon-Assisted Tunneling, in Semiconductors in Crossed and Parallel Electric and Magnetic Fields.* Phys. Rev., 1967. **163**: p. 733-742.

189. Patanè, A., et al., *Manipulating and Imaging the Shape of an Electronic Wave Function by Magnetotunneling Spectroscopy.* Phys. Rev. Lett., 2010. **105**: p. 236804.

190. Makarovsky, O., et al., *Using randomly distributed charges to create quantum dots.* Phys. Rev. B, 2010. **81**: p. 035323

191. Chen, W.M., et al., *Point defects in dilute nitride III-N—As and III-N—P*. Physica B, 2006. **376-377**: p. 545-551.

192. Buyanova, I.A., W.M. Chen, and C.W. Tu, *Defects in dilute nitrides.* J. Phys.: Condens. Matter, 2004. **16**: p. 3027-3035.

193. Fan, W.J., et al., *Comparison of nitrogen compositions in the as-grown GaNxAs1−xGaNxAs1−x on GaAs measured by high-resolution x-ray diffraction and secondary-ion mass spectroscopy*. Appl. Phys. Lett., 2002. **80**: p. 4136.

194. Kammerer, C., et al., *Photoluminescence Up-Conversion in Single Self-Assembled InAs/GaAs Quantum Dots.* Physical Review Letters, 2001. **87**(20): p. 207401.

195. Turyanska, L., et al., *Sharp-line electroluminescence from individual quantum dots by resonant tunneling injection of carriers*. Vol. 89. 2006. 092106-092106.

196. Baumgartner, A., et al., *Upconversion electroluminescence in InAs quantum dot light-emitting diodes.* Applied Physics Letters, 2008. **92**(9): p. 091121.

197. Allaberenov, O.A., et al., *Photoluminescence of n-type InAs.* Soviet Physics - Semiconductors, 1973. **4**(10): p. 1662.

198. Lin, H.-K., et al., *Design and characteristics of strained InAs/InAlAs composite-channel heterostructure field-effect transistors.* J. Appl. Phys., 2005. **97**: p. 024505

199. Aspnes, D.E. and A.A. Studna, *Dielectric functions and optical parameters of Si, Ge, GaP, GaAs, GaSb, InP, InAs, and InSb from 1.5 to 6.0 eV.* Physical Review B, 1983. **27**(2): p. 985-1009.

200. Maycock, P.D., *Thermal conductivity of silicon, germanium, III–V compounds and III–V alloys.* Solid-State Electronics, 1967. **10**(3): p. 161-168.